Analysis of complex faulting: Wavelet transform, Multiple datasets and Realistic fault geometry

Thesis by

Chen Ji

In Partial Fulfillment of the Requirements
for the Degree of
Doctor of Philosophy

Caltech
Pasadena, California

2002
(Submitted March 26, 2002)

Acknowledgements

I would like to first thank my thesis advisor, Don Helmberger, for his support, patience and encouragement. He taught me how to read the beautiful wiggles of seismograms and spent a notable amount of time to improve my manuscripts. At same time, he gave me remarkable amount of freedom to do what I interest. I am grateful to David Wald, who has been involved in most of my research projects and is very supportive in every way possible.

Other faculties have offered various help in my education and research. Mark Simons is fun to talk with and is always ready to criticize my theories or answer my questions. Don Anderson and Rob Clayton, as my academic advisors, have provided all the needed assistance. Discussing with Hiroo Kanamori, Tom Heaton and Don Anderson during coffee break is the best way to learn the physics of earthquakes. I also want to thank Seismo lab staff, particularly Evelina Cui and Viola Carter.

My research has benefited from discussions with many graduate students and post-docs. Among them are Lupei Zhu, Jishu Deng, Luc Lavier, Stone Ni, Jeroen Ritsema, Jascha Polet, Brian Savage, Leo Eisner, Cangli Liu, and Matthew Pritchard. Specific thanks to Lianxing Wen, Alex Song, Kuo-Fong Ma and my officemates. Lianxing and his wife, Meilan, encouraged me to apply the Seismo Lab and welcomed me by providing countless delicious foods. Alex and Prof. Ma gave me lots of information related to the Chi-Chi earthquake and Taiwan tectonics. My officemates, Anupama Venkataraman, Jeanne Hardebeck, Emily Brodsky, Patricia Persaud, Debbie Smith, Ying Tan, Ali Ozgun Konca and Min Chen gave me various assistance to make my life at Caltech easy.

Most chapters of this thesis are based on papers published or submitted. Many people helped me by reviewing the manuscripts, including Hiroo Kanamori, Mark Simons, Jason Saleeby, Steve Hartzell, Greg Beroza, V. Langenheim and several anonymous reviewers. I thank D. Agnew, S.-B. Yu and K.F. Ma for providing the GPS data of the 1999 Hector Mine and Chi-Chi earthquakes. This Ph.D. research work was supported by SCEC contract No. NSF EAR-8920136, NSF EAR-0106701 and by the U.S. Geological Survey under Contract No. 1HQGR0098.

In the end, I want to thank many teachers and friends at Institute of Geophysics, Chinese Academy of Science, particularly Prof. Zhenxing Yao, supervisor of my Master degree. They had offered important help during the beginning phase of my academic life. Finally, I want to thank my parents and lovely wife for their long time support and encouragement. I devote this thesis to them.

Abstract

This thesis presents the studies of two recent large and well-recorded earthquakes, the 1999 Hector Mine and Chi-Chi earthquakes. A new procedure for the determination of rupture complexity from a joint inversion of static and seismic data was first developed. This procedure applies a wavelet transform to separate seismic information related to the spatial and temporal slip history, then uses a simulated annealing algorithm to determine the finite-fault model that minimizes the objective function described in terms of wavelet coefficients. This method is then applied to simultaneously invert the slip amplitude, slip direction, rise time and rupture velocity distributions of the Hector Mine and Chi-Chi earthquakes with both seismic and geodetic data. Two slip models are later verified with independent datasets.

Results indicate that the seismic moment of the Hector Mine earthquake is 6.28×10^{19} Nm, which is distributed along a "Y" shape fault geometry with three segments. The average slip is 1.5 m with peak amplitudes as high as 7 m. The fault rupture has an average slip duration of 3.5 sec and a slow average rupture velocity of 1.9 km/sec, resulting in a 14 sec rupture propagation history. The rise time appears to be roughly proportional to slip, and the two branches of "Y" shape fault rupture together. The Chi-Chi earthquake is the best-recorded large earthquake so far. Its seismic moment of 2.7×10^{20} Nm is concentrated on the surface of a "wedge shaped" block. The rupture front propagates with a slow rupture velocity of about 2.0 km/sec. The average slip duration is 7.2 sec. Four interesting results are obtained: (1) The sinuous fault plane strongly affects both spatial and temporal variation in slip history; (2) Long-period peak slip velocity increases as the rupture propagates; (3) The peak slip velocity near the surface is in general higher than on the deeper portion of the fault plane as predicted by dynamic modeling [e.g., *Oglesby et al.*, 1998]; and (4) the complex fault geometry and slip distribution are related to the two transfer zones obliquely across Taiwan, which separate Taiwan into three regions with different tectonic activity. The transfer zone in the north can be explained by the slab breakoff mechanism proposed by *Teng et al.* [2000] recently.

Contents

List of Figures

List of Tables

Chapter 1 Introduction

Understanding the behavior of earthquakes is one of the reasons to have a discipline called seismology. Traditionally, there are two branches of seismology that address the earthquake physics. One attempts to estimate earthquake rupture histories based on observations on the surface (geodetic data and seismograms); the other attempts to simulate a complex earthquake with a fault model built with the simple constitutive laws inferred from the fracture mechanics and rock mechanics. These two approaches are named separately as the kinematics and dynamics of an earthquake, respectively [*Aki and Richards*, 1980], and are complementary. For instance, the kinematic study generates insights to modify the constitutive laws used in the dynamic simulation (e.g., *Heaton*, 1990). In this thesis, after some efforts in improving tools, I present kinematic models of two best-recorded large earthquakes ($M_w > 7$), the 1999 Hector Mine and Chi-Chi earthquakes. Finally, I will discuss their impacts in understanding earthquake faulting and local tectonics.

The finite fault approach I used in this study was developed after the 1979 Imperial Valley, California, earthquake (e.g., *Olson and Apsel*, 1982; *Hartzell and Heaton*, 1983), and has been greatly improved in recent years. This kind method constrains the rupture history of an earthquake by minimizing the difference between observed seismic data and synthetics. However, conventional finite-fault inverse procedures work exclusively in either the time domain or the frequency domain, the spatial distribution and character of slip heterogeneity on the fault plane influences not only the frequency content of the outgoing seismic wave, but also when such effects appear on seismograms. In order to extract more information about slip heterogeneity, it is best to simultaneously consider both the time and frequency characteristics of the waveforms. To this end, we introduce a wavelet transform approach for studying the spatial and temporal slip history of earthquakes in Chapter 2. Our limited knowledge of the earth structure and over-simplified fault plane geometry are also important causes of the uncertainty embedded in any inverted slip history. Then using a more realistic fault geometry and performing a seismic and geodetic combined inversion [*Wald and Graves*, 2001] are fundamental attempts for a reliable kinematic model, which are integrated into our inverse procedure too.

In Chapter 3, the new inverse procedure was applied to study the 1999 Hector Mine earthquake. Four datasets, including waveforms of 10 strong motion stations and 23 teleseismic stations, geodetic displacements of 36 GPS monuments, and geological surface offsets, are used to construct the slip history. The slip amplitude, rake angle, rupture initiation time and rise time function of each subfault are inverted simultaneously. The result indicates that the Hector Mine earthquake has a different rupture scenario comparing to the 1992 Landers earthquake, even though they are within the same tectonic province and separated by only 20 km. I will show how a close *TriNet* station can help us to constrain a "Y" shape fault geometry, whose two branches ruptured simultaneously.

The next three chapters focus on the 1999 Chi-Chi earthquake, which has the best strong motion and GPS coverage for a magnitude over 7 earthquake to date. In Chapter 4, the well-distributed geodetic data not only constrain a complex fault geometry, but allow retrieval of a physical plausible slip distribution as well. As a continuation, in Chapter 5, the 3-component velocity waveforms at 36 strong motion stations are added into the inversion to understand how fast the over 10 meter slip occurred. To verify inverted slip history constructed by only local measurements, the teleseismic P and SH ground velocities have been first forward predicted with a satisfying result. Among the many interesting observations from this study, the most exciting result is the strong correlation between the slip history and complex fault geometry. It addresses a long-standing argument that the fault topography first order controls the dynamic rupture of earthquakes (e.g., *Scholz*, 1990).

It is well established that the large slip related to the big earthquakes is accumulated by local tectonic motions. Then the information of earthquakes becomes important constraints to the tectonic study. In fact, focal mechanisms and cumulative displacement of earthquakes have become general information in inferring the current direction and rate of relative plate motions. However, a big earthquake usually involves a large fault dimension, and contains more useful information than what we can obtain from a point-source focal mechanism. For instance, the Chi-Chi earthquake is a thrust event in a point-source representation (e.g., Harvard CMT), but the inverted slip distribution exhibits important strike slip components, consistent with geological observations. An unusual slip pattern that both left-lateral and right-lateral motions appear in single earthquake, indicates the rapid spatial variation of the local stress field, and is used as an unique observation to investigate the mechanism of a narrow transfer zone across Central Taiwan in Chapter 6. Hence, the slip histories of large earthquakes would be very helpful to the study of local tectonics.

Chapter 2 Wavelet domain inversion theory and resolution analysis

2.1 Abstract

We present a new procedure for the determination of rupture complexity from a joint inversion of static and seismic data. Our fault parameterization involves multiple fault segments, variable local slip, rake angle, rise time and rupture velocity. To separate the spatial and temporal slip history, we introduce a wavelet transform that proves effective at studying the time and frequency characteristics of the seismic waveforms. Both data and synthetic seismograms are transformed into wavelets that are then separated into several groups based on their frequency content. For each group, we use error functions to compare the wavelet amplitude variation with time between data and synthetic seismograms. The function can be an L1+L2 norm or a correlative function based on the amplitude and scale of wavelet functions. The objective function is defined as the weighted sum of these functions. Subsequently, we developed a finite-fault inversion routine in the wavelet domain. A simulated annealing algorithm is used to determine the finite-fault model that minimizes the objective function described in terms of wavelet coefficients. With this approach, we can simultaneously invert for the slip amplitude, slip direction, rise time and rupture velocity efficiently. Extensive experiments conducted on synthetic data are used to assess the ability to recover rupture slip details. We also explore slip-model stability for different choices of layered earth models assuming the geometry encountered in the 1999 Hector Mine, California, earthquake.

2.2 Introduction

Detailed mapping of spatial and temporal slip distributions of large earthquakes is one of the principal goals of seismology. After the 1979 Imperial Valley, California, earthquake, an approach, which was called finite fault inversion method, was developed to study the complexities of larger earthquakes (e.g.,*Olson and Apsel*, 1982; *Hartzell and Heaton*, 1983). During the past two decades, the methodology has been greatly improved. In the early work of *Hartzell and Heaton* [1983], the slip velocity was fixed or allowed to vary only slightly during the inversion. Attempts have been made to invert for both slip amplitude and rupture time (e.g., *Beroza and Spudich*, 1988) and, more recently, global inversion methods were introduced, where slip amplitude, rupture time, and rise time were determined simultaneously (e.g., *Hartzell et al.*, 1996). These studies are time domain inversions, i.e., the fault model is determined by fitting the seismic waveform data. In addition, *Olson and Anderson* [1988] investigated the use of a linear frequency domain inversion, which also allowed for the simultaneous solution of both slip amplitude and rupture time. Several larger earthquakes have been analyzed using a variety of the above methods (e.g., *Wald et al.*, 1991, 1994, 1996; *Beroza*, 1988, 1991; *Hartzell*, 1991, 1994, 1996), and the complexity and general characteristics of these earthquakes have been used in scores of seismological studies and even to invoke a new theory of earthquake mechanics (e.g., *Heaton*, 1990).

Although conventional finite-fault inverse procedures work exclusively in either the time domain or the frequency domain, the spatial distribution and character of slip heterogeneity on the fault plane influences not only the frequency content of the outgoing seismic wave, but also when such effects appear on seismograms. In order to extract more information about slip heterogeneity, it is best to simultaneously consider both the time and frequency characteristics of the waveforms. To this end, we introduce a wavelet transform approach for studying the spatial and temporal slip history of significant earthquakes.

Recently, *Graves and Wald* [2001] and *Wald and Graves* [2001] discussed the effects of velocity structure on source resolution. They found that by using seismic waveform data only, an inaccurate velocity structure could strongly bias the inversion results. Fortunately, they also found that the static displacements have different sensitivity to velocity structure, and adding geodetic data to inversion enhances the robustness of the inversion. However, the wavelet transform approach that we will introduce can not be applied to the static information, so we include it into our inversion method separately.

In the present paper, we first give a brief review of finite fault representation theory suggested by *Hartzell et al.* [1996], then use it to introduce the wavelet transforms and to construct a useful objective function and perform slip history inversions. Finally, we use the data distributions encountered in the 1994 Northridge, and the 1999 Hector Mine, California, earthquakes to test the resolution. In the rest of the chapters, the method developed here was used to study slip history of the Hector Mine earthquake (Chapter 3) and Chi-Chi earthquake (Chapter 4, 5) in detail.

2.3 Finite fault approach

The response of a finite fault at a station can be approached by summing the contributions of a regular grid-work of subfaults (e.g., *Hartzell and Heaton*, 1983):

$$\begin{aligned} u(t) = \sum_{j=1}^{n}\sum_{k=1}^{m} D_{jk}[cos(\lambda_{jk})Y_{jk}^{1}(V_{jk},t) \\ + sin(\lambda_{jk})Y_{jk}^{2}(V_{jk},t)] * \dot{S}_{jk}(t) \end{aligned} \tag{2.1}$$

Here, $u(t)$ is the displacement at an arbitrary station, j is the $j-th$ subfault along-strike, and k is the k-th subfault down-dip. D_{jk}, λ_{jk} and $S_{jk}(t)$ are the average dislocation amplitude, rake angle and rise time function, respectively. V_{jk} is the average rupture velocity between the hypocenter and subfault jk. The terms $Y_{jk}^{1}(V_{jk},t)$ and $Y_{jk}^{2}(V_{jk},t)$ are the subfault Green' functions for the unit slip in the strike direction and down dip direction, respectively. Each such function is obtained by summing the responses of point sources uniformly distributed over it. Every point source is delayed appropriately by the time that is equal to the shortest on-fault distance from the hypocenter divided by the average rupture velocity. Thus, all subfault Green's functions separately include the correct effects of the directivity. The number of point sources used depends on the size of subfaults and highest frequency studied.

Following the work of *Cotton and Campillo* [1995] and *Hartzell et al.* [1996], we use a modified cosine function to represent rise time function, S(t) (Fig. 2.1a),

$$\frac{d\,S(t)}{dt} = \frac{1 - cos(2\pi t/r)}{r}, 0 < t < r \tag{2.2}$$

Here, r is width of rise time function. The advantage of this approach is that we need only one parameter to represent the rise time function. This makes the inversion more stable. We use this approach in studying 1999 Hector Mine earthquake. When we have a better strong motion coverage such as the situation of the 1999 Chi-Chi earthquake, we attempt to use a more complex form [*Zeng and Chen*, 2001] (Fig. 2.1b).

$$\frac{d\,S(t)}{dt} = \begin{cases} \frac{1}{t_s+t_e}(1 - cos(\frac{\pi t}{t_s})) & 0 < t < t_s, \\ \frac{1}{t_s+t_e}(1 - sin(\frac{\pi t}{t_s})) & t_s < t < t_s + t_e, \\ 0 & t > t_s + t_e \end{cases} \tag{2.3}$$

In this approach, the derivative rise function is determined by just two parameters. The first one, called the starting-phase time (t_s), is used to measure the duration from the rupture initiation to the time with maximum slip velocity; the second one, called the end-phase time (t_e), is used to measure duration to accomplish the rest of slip. This approach permitted us to model the asymmetric "pulse" like ground velocity that are clearly observed by strong motion stations near the surface break of the 1999 Chi-Chi earthquake.

Apparently, such approaches limit the complexity of the time history of individual subfaults in comparison to the multiple time window approach (e.g., *Wald and Heaton*, 1994). However, *Guatteri and Spudich* [2000] have demonstrated that such complexity may be hard to constrain with only low frequency strong motion data.

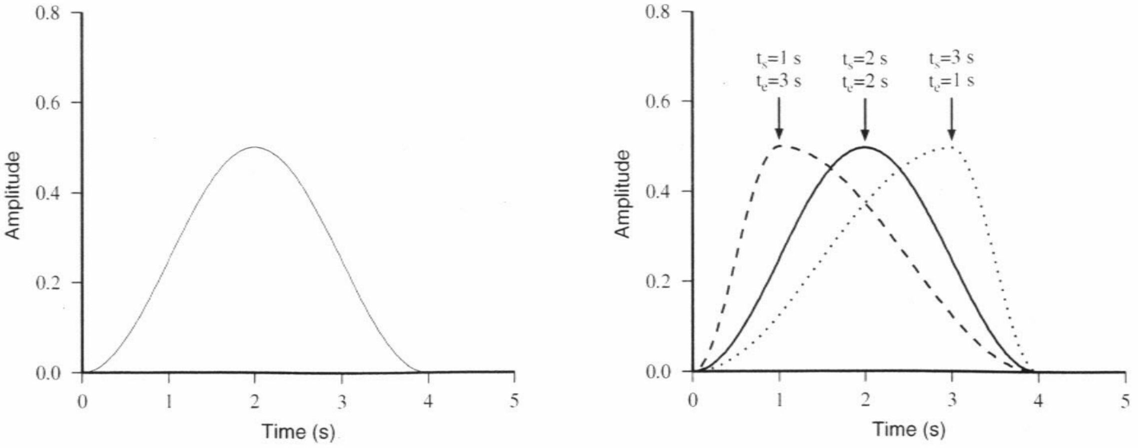

(a)

(b)

Figure 2.1: Derivative rise time function. (a) Symmetric derivative rise time function with a rise time $r=$ 4 sec. It is defined by formula (2.2). (b) Three possible derivative rise time functions with same rise time of 4 sec. There are defined by formula (2.3).

Equation (2.1) can also be used for the static response of a finite fault by replacing $Y^i_{jk}(V_{jk}, t)$ with its static Green's function Y^i_{jk}. With this approach, a full representation of the fault response relies on four parameters, i.e., dislocation amplitudes, rake angles, average rupture velocities and rise time widths. Thus, we can invert the parameters by matching the synthetic seismograms and static displacements to the observations.

2.4 Objective function and inversion method

Finite fault inversion involves finding the values of fault parameters that can minimize a misfit or objective function. This function characterizes the differences between observed and synthetic data calculated by using a fault model and the propagation effects produced by an assumed earth model. Hence, two questions must be answered: what is the definition of the misfit function and how do we find the minimum? We will address these issues in this section.

For significant earthquakes, the relative low frequency signals (frequency $f < 0.2$ Hz) usually dominate displacement records. Thus, such information is essential to constrain the general picture of a seismic source, but it is not as sensitive to the detailed characteristics, such as variations of rise time, rupture velocity. On the other hand, a sudden change in slip amplitude or rupture velocity radiates strong high frequency seismic signals (effects similar to a stopping phase, *Aki and Richards*, 1980). Hence, studying higher frequency signals will increase the spatial and temporal resolution.

However, because of the large difference in amplitudes, it is difficult to simultaneously capture lower and high frequency information with time domain waveform inversions, which emphasize the longer period and larger amplitude signals. While the fit to lower frequency and higher frequency signals are independent in frequency domain inversions, because Fourier transform decomposes seismograms into sine or cosine functions, it is easy to lose other important information about when such signals arrive.

In order to handle this problem, we could separate a seismogram into many traces containing different frequencies and invert them separately. This was attempted by *Mendoza and Hartzell* [1988], who used long period, short period and intermediate period teleseismic P waves to constrain the slip distribution for the 1986 Palm Springs earthquake. Similarly, *Wald et al.* [1996] used both displacement and velocity records for the slip history of the 1994 Northridge, California, earthquake. Here, we introduce a new data processing technique, the wavelet transform, which appears to be ideal for handling the above time-frequency problems, and is also ideal for inversion application.

2.4.1 Wavelet transform

The wavelet transform has been developed over the last two decades [*Mallat*, 1998]. In contrast to the Fourier transform, it decomposes a time series into a sum of wavelets, which are functions satisfying the rule:

$$\int_{-\infty}^{+\infty} \psi(t)dt = 0 \tag{2.4}$$

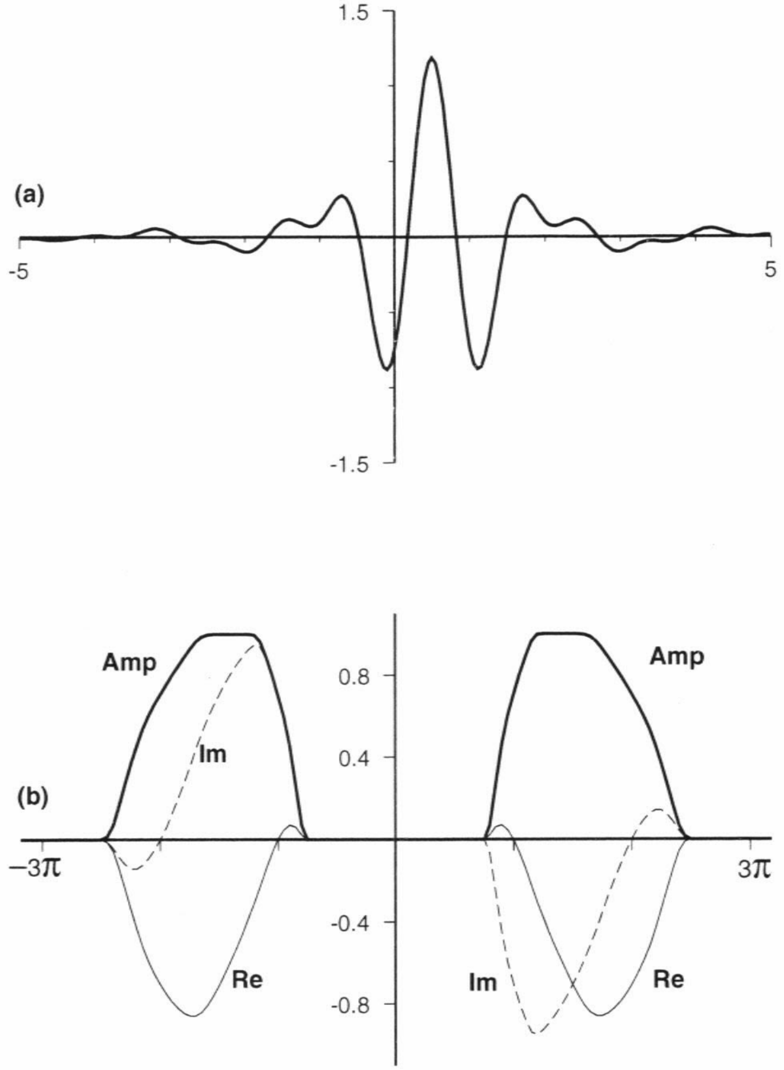

Figure 2.2: Analyzing wavelet of Meyer-Yamada: (a) Waveform in the time domain. (b) Amplitude (thick line), real (thin line) and imaginary (dashed line) parts in the frequency domain (modified from *Yomogida*, 1994).

The wavelet function dilated with a scale parameter s and translated by u is referred as a wavelet atom:

$$\psi_{s,u} = \frac{1}{\sqrt{s}}\psi(\frac{t-u}{s}) \tag{2.5}$$

A wavelet transform coefficient of seismogram $f(t)$ at the wavelet scale s and position u is defined by

$$\alpha_{s,u} = \int_{-\infty}^{+\infty} f(t)\psi_{s,u}(t)dt \tag{2.6}$$

With such continuous wavelet transforms, we can detect signal variations in 2D time-frequency space. However, it is not suitable for an inversion procedure because s and u are continuous, and do not form an orthonormal base by uniform sampling [*Mallat*, 1998]. Hence, we will either miss some useful information, or get abundant linearly dependent constraints. This problem can be solved by using an orthonormal discrete wavelet transform (ODWT). In fact, one ODWT, called the Meyer-Yamada wavelet (MYW), has been introduced to process seismic data by *Yomogida* [1994]. The analytic representation of the MYW is complex. Here, we plot its shapes in the time and frequency domains in Figure 2.2 to illustrate its basic characteristics. Note that in the frequency domain, the real parts of the ψ are symmetric and the imaginary parts are anti-symmetric, thus ψ is a pure real function in the time domain, which is a particularly useful property in handling time series.

For a discrete time series y_i ($i = 0, 1, 2, ..., N-1$, and $N = 2^n, n$ is integer) with the length T $= N\Delta t$ (Δt is the sample interval), the discrete MYW atoms can be represented as

$$\begin{gathered}\psi_{j,k}(i) = \sqrt{\frac{1}{2^{n-j}\Delta t}}\psi(\frac{i}{2^{n-j}\Delta t} - k), \\ j = 0, 1, \cdots, n-1 \text{ and } k = 0, 1, \cdots 2^j - 1\end{gathered} \tag{2.7}$$

Here j is the discrete form of s, and k is the discrete form of u . The discrete wavelet transform is expressed by

$$y_i = \sum_{j=0}^{n-1} \sum_{k=0}^{2^j-1} \alpha_{j,k} \psi_{j,k}(i) \tag{2.8}$$

where the coefficients are calculated with the fast algorithm suggested by *Yamada and Ohkitani* [1991].

Since the wavelet function $\psi(\omega)$ will be non-zero only within $[2\pi/3, 8\pi/3]$ (Fig. 2.2), the wavelet atom is band-limited in range $[2^j/3T, 2^{j+2}/3T]$ for each j; Furthermore, in contrast with the sine and cosine harmonic functions, which have the same amplitudes universally, the wavelet function is spatially compact. The amplitude decay in Figure 2.2a shows a factor of 10 reduction over a small window $-1 < s < 2$. Hence, a coefficient $\alpha_{j,k}$ measures the variation of s_i in the neighborhood of $i = k \times 2^{n-j}$ whose size is proportional to s. However, because of the condition shown in equation (2.4), this wavelet transform can not resolve the static component of the signal. This is consistent with the fact that the total number of coefficients is $N-1$, even though the number of original data is N [*Yomogida*, 1994].

The MYM is an orthonormal base [*Yomogida*, 1994], i.e., suppose we have another time series u_i, $(i = 0, 1, ..., N-1)$ with corresponding coefficients $\beta_{j,k}$. Then u_i is a good match to y_i if and only if $\alpha_{j,k} = \beta_{j,k}$, for $j = 0, 1, \cdots, n-1$; $k = 0, 1, \cdots, 2^j - 1$. With this characteristic, we can construct an objective function in MYM domain as we did in the time and frequency domain.

2.4.2 Test example

We use a simple test to show the advantage of our time-frequency analysis. A fault model which is simplified from the finite fault inversion modeling of the 1994 Northridge earthquake (Fig. 2.3; *Wald et al.*, 1996) is used to generate the synthetic data. Note that we assign slip to occur only on two rectangle asperities, **A** and **B**. Asperity **A** is deep and has a uniform rise time 0.5 sec and slip 1 m. Asperity **B** is shallower and has 2.5 sec rise time and slip 2 m.

We generate the synthetic P waves of an arbitrary teleseismic station, whose distance and azimuth are 70°, 236° respectively. We choose a layered velocity model suggested by *Wald et al.* [1996]. The responses to asperity **A**, **B** and the whole fault (**A+B**) are shown in (Fig. 2.3b).

Due to the differences in propagation and rise time, the waveforms generated from the two patches are quite different. The response generated from subevent **A** has more high frequency energy and arrives earlier; that from the subevent B has more lower frequency signal and arrives later. For the purpose of inversion, we attempt to find the crucial information from **A+B** which can separate the effects of the two asperities. Note that it is the high-frequency information that highlights the differences in rise time, and it is the time information that can localize the position of source.

In Figure 2.3c and Figure 2.3d, we use the MYW transform to convert the data **A** and **B** into traces with same scales and compare them with corresponding transform results of data **A+B**. Note that it becomes easier to separate the effects in time-frequency domain (Fig. 2.3c and 2.3d) than in time domain only (Fig. 2.3b). First, the energy from the short rise-time subevent dominates the higher frequency channels and that from the long rise-time subevent are larger in the lower frequency channels. Second, the wavelet transform can provide relatively accurate localization of seismic energy in the high frequency channels, e.g., in the last three channels ($j = 6, 7, 8$), the signals have died out before the end of signal generated by block B. This appears to be the key information needed to constrain rise time variations.

However, the wavelet transform can not change the frequency content of a seismic signal. The amplitude difference between high frequency and lower frequency signal still exists. Hence, if we just use the $L2$ norm as criteria to measure the difference between wavelet atom coefficients, we would get the same results as we do in the time domain. As a test, we assume the synthetic seismogram of **A+B** is $o_i, i = 0, 1, ..., 511$. The sample interval is 0.1 sec and the $o_{j,k}$ are wavelet coefficients. We define another series s_i^m which satisfy

$$s_i^m = \begin{cases} 0 & \text{if } m = 0; \\ \sum_{j=0}^{m-1} \sum_{k=0}^{2^j-1} o_{j,k} * \psi_{j,k}(i) & \text{if } 0 < m < 9; \end{cases} \tag{2.9}$$

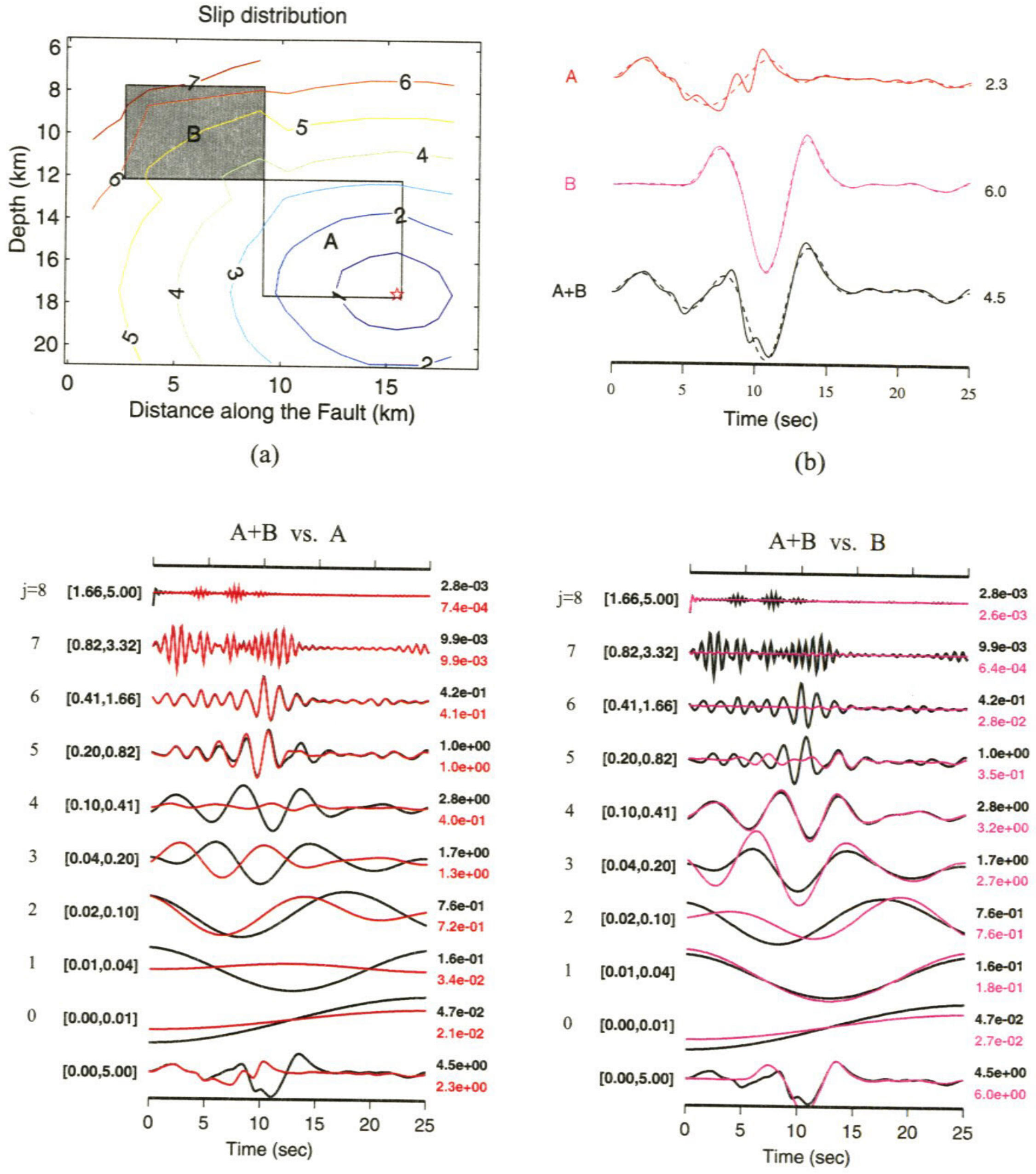

(a) (b) (c) (d)

Figure 2.3: The advantage of wavelet transform. (a) The dip, strike and rake angles of the test fault plane are 40°, 121° and 112°, respectively. The slip distribution has been discussed in text. Contours in a 1.0 sec interval indicate the rupture initiation time. (b) Synthetic vertical velocity records of teleseismic P wave are generated by the block **A**, block **B** and whole fault (**A+B**) as labeled in the left, respectively. The dashed lines show the contributions in the first 5 wavelet scales ($j = 0, 1, 2, 3, 4$). The peak amplitudes in milli-meter per second are indicated in the right. (c) Comparison between data **A** and data **A+B** in different wavelet channels. The frequency content of each wavelet channel is shown in the left (low, high frequency bands given), and the peak amplitudes are indicated in the right with the same color as data. (d) Similar comparison between data **B** and data (**A+B**).

We can measure the least-square error in both time domain and wavelet domain by formula,

$$e_m^t = \frac{\sum_{k=0}^{N-1}(o_i - s_i^m)^2}{\sum_{k=0}^{N-1}(o_i)^2} \tag{2.10}$$

$$e_m^w = 1 - \frac{\sum_{j=m}^{n-1}\sum_{k=0}^{2^j-1} o_{j,k}^2}{\sum_{j=0}^{n-1}\sum_{k=0}^{2^j-1}(o_i)^2} \tag{2.11}$$

where e_m^t and e_m^w are the normalized L2 errors in the time domain and the wavelet domain, respectively. The crosses and circles in Figure 2.4 show the variation of two error functions with m, which essentially overlay. This test, in fact, is a demonstration of the orthonormal characteristic of the MYW. This example also indicates that time domain inversion emphasizes longer period and larger-amplitude signals. Note, that after summing the first five channels ($j > 5$), the error function is reduced to less than 5 percent. It is noteworthy that we only need 31 wavelet coefficients to uniquely determine the waveforms of first 5 channels ($j = 0, 1, 2, 3, 4$), which is only about 6 percent of total number of coefficients (511). Then, if we can not use information of smaller scale signals, the constraint of the source is strongly limited. Furthermore, the key information that can separate differences in rise time is contained in the small scale traces. Fortunately, in the wavelet domain, we can separate the coefficients by scales, then the contribution of the smaller scale coefficients can be enhanced easily.

Finally, it is noteworthy that using the wavelet transform to divide the time series into traces with the same scale is similar in effect to the multiple bandpass filter. Hence, the method proposed here is close to the approach used by *Mendoza and Hartzell* [1988]. However, constructing the error function in the wavelet domain is more efficient than in the time domain due to the multiple traces with different frequency contents, i.e., suppose we have a seismogram with N samples; if we separate it into M frequency bands, then we need to match NM time samples compared with N coefficients for the wavelet transform approach.

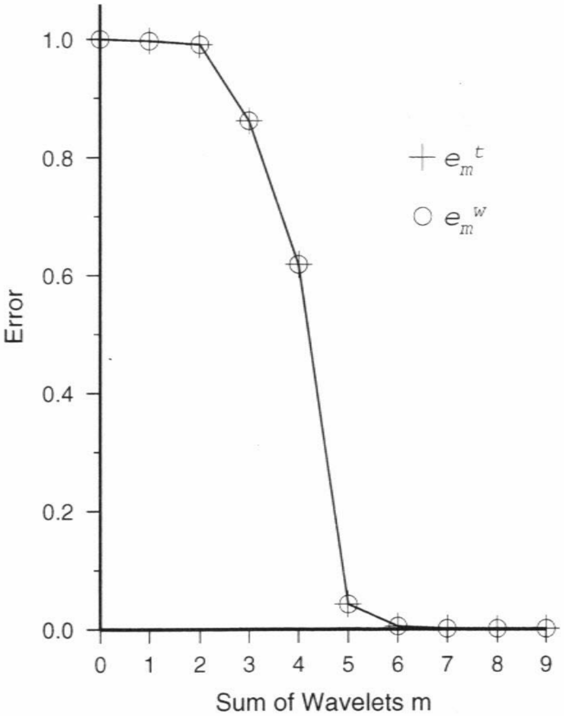

Figure 2.4: L2 norm variations versus summations of wavelet channels. The crosses show the behavior in the time domain, and circles show the behavior in the wavelet domain.

2.4.3 Objective function for waveform: Multiple criteria

Suppose series o_i and y_i are the observed and synthetic seismograms, respectively, and $o_{j,k}$ and $y_{j,k}$ are the corresponded wavelet coefficients. As discussed above, the large amplitude difference between the lower and higher frequency signals still exists; thus, we need to give more weight to the coefficients of small scale (high-frequency) wavelet atoms. For this purpose, we separate the wavelet coefficients into two groups by their scales and use different criteria to measure them.

The L1 or L2 norm is good at comparing absolute amplitudes, and their combination takes advantage of both L1 and L2 as suggested by many authors (e.g., *Zhao and Helmberger*, 1994). We use it to measure the differences in lower frequency (large scale), but larger amplitude coefficients.

$$e_l = \sum_{j_{min}}^{j_c} W_j \left(\frac{1}{k_j} \sum_{k_j} |o_{j,k} - y_{jk}| + \sqrt{\frac{1}{k_j} \sum^{k_j} (o_{j,k} - y_{j,k})^2} \right) \tag{2.12}$$

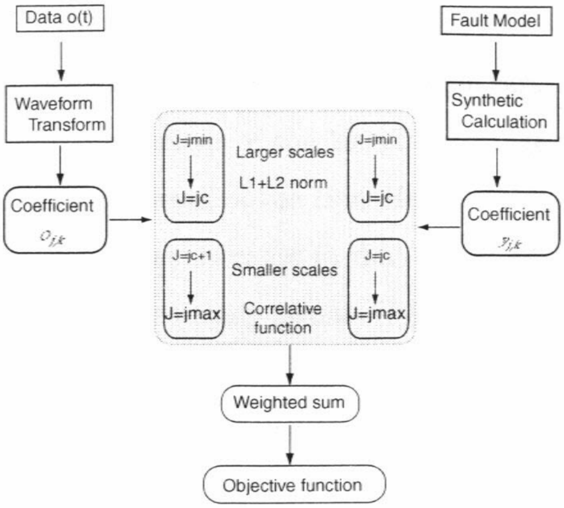

Figure 2.5: The flow chart of the objective function. Note that the synthetic calculation includes two steps. First, we generate synthetic seismograms in time domain and then we do a wavelet transform to convert them into the wavelet domain.

Note that the largest wavelet scale s_{max} used in an inversion is equal to $s_{max} = T/2^{2^{j_{min}}}$; and the critical scale s_c can be represented as $s_c = T/2^{j_c}$, T is the signal duration. Thus j_{min} and j_c correspond to the largest and smallest scale wavelets measured by this criteria, respectively.

The correlative function suggested by *Sen and Stoffa* [1991] focuses on signal shape, and is relatively less sensitive to the signal amplitudes, so it is good at handling the high frequency and small amplitude information. Thus, we define

$$e_h = \sum_{j_{c+1}}^{j_{max}} W_j(1.0 - \frac{2 \times \sum^{k_j} o_{j,k} y_{j,k}}{\sum^{k_j} o_{j,k}^2 + \sum^{k_j} y_{j,k}^2}) \tag{2.13}$$

Here, j_{max} corresponds to the smallest scale wavelets, $s_{min} = T/2^{j_{max}}$.

As we pointed out earlier, the effect of the wavelet transform is similar to multiple bandpass filters. Then by defining the bandpass width of a wavelet function as the frequency region with spectrum amplitudes larger than $1/\sqrt{2}$, we can derive the simple relation between the bandpass width and scale of a wavelet atom, i.e., $1/2s < f < 1/s$, where f is the frequency. Hence the choices of s_{max} and s_{min} should depend on the frequency contents of the seismic signals, and our knowledge of the earth structure. In our study, s_{max} is roughly equal to the reliable signal duration, and s_{min} is close to the shortest seismic period that we can model.

The critical scale s_c is chosen based on the amplitude variation with wavelet scales. For example, in the later simulations of the 1994 Northridge, California, earthquake, we use s_c as 1.6 sec. But in the work of the 1999 Hector Mine, California, earthquake, we use a longer scale, $s_c = 3.2$ sec, because in that event, most strong motion records were dominated by the lower frequency signals (Figure 3.7 in Chapter 3).

Figure 2.5 shows the flow chart of the objective function. This function is the sum of measurements of the higher frequency channels and lower frequency channels.

$$err_{wf} = e_l + e_h \tag{2.14}$$

Note that the data only need to be transformed once. However, for each new fault model, the synthetic wavelet coefficients must be recomputed. In our approach, both teleseismic and strong motion synthetic seismograms are generated in the frequency domain, thus we can apply the efficient algorithm suggested by *Yamada and Ohkitani* [1991] to calculate the wavelet coefficients.

2.4.4 Objective function for GPS measurement

Near-field GPS measurements are very helpful in constraining the slip distribution of earthquakes, and thus increase the robustness of inversion [*Wald and Graves*, 2001]. But as mentioned above, static displacement data can not be included into above wavelet transform approach. Thus, we need to treat the static displacement separately.

Sum-squared residuals χ^2 have been used as the criteria to measure the difference between synthetic and observed static displacements (e.g., *Hudnut et al.*, 1996). This can be represented as

$$err_{st} = \sum_{i}^{N} (\frac{S_o^i - S_s^i}{\sigma^i})^2 \tag{2.15}$$

where S_o^i and S_s^i are the $i-th$ observed and synthetic static displacements, respectively. σ is the observed standard error. However, this criterion has two weaknesses. First, since the static displacements decay rapidly with the distance from fault trace, the formula can not fairly treat every measurement. For instance, in our study of the 1999 Hector Mine earthquake (Chapter 3), the largest GPS record is 85 cm, and the smallest is only 3 cm. Suppose σ is the same for all data and that the criteria χ^2 indicates that there is a 1.5 cm misfit in some measurements. Then, if such misfit is related to the largest observation, the model can explain over 98 percent of the amplitude. Thus, further improvement is better but may be not necessary. However, if the same amount of misfit is relative to the 3.0 cm observation, the model should be further improved. Second, equation (2.15) only considers the observed error, but our numerical example discussed later demonstrates that two possible layered velocity structures can easily produce 5 percent amplitude differences.

Due to the uncertainty in earth structure, a perfect fit to the largest amplitude records may not be a physical or desirable solution. But a model is probably acceptable if it can explain over 95 percent of the amplitude of every GPS observation. Hence we modified equation (2.15) by introducing a threshold. If the relative difference between the synthetic static displacement and the data is less than 5 percent, we let the difference be zero. Then, the new criteria is

$$S_o - S_i = \begin{cases} 0 & \text{if } |S_o - S_i| < 0.05 * S_o, \\ S_o - S_i & \text{otherwise} \end{cases} \tag{2.16}$$

With this precondition expression (2.16), the result will have an error even when it is zero. However, it is very small, and we can prove that the errors satisfy,

$$\frac{\Delta S}{S_o} \leq 0.05; \tag{2.17}$$

$$\Delta\theta < 3^o \tag{2.18}$$

ΔS and $\Delta\theta$ are the probable misfits in amplitude and direction when the $\chi^2 = 0$.

2.4.5 Inversion method

When we try to simultaneously invert seismic and GPS observations, the criteria can be represented as

$$err_{wf} + W_{st} \times err_{st} + W_c \times (constraints) = \text{minimum} \tag{2.19}$$

Two types of constraints are chosen: one that minimizes the difference between the slip on adjacent subfaults, and the second one that minimizes the total moment [*Hartzell et al.*, 1996]. Using additional constraints increases the stability of inversion but the resolution is reduced. Two weights W_{st} and W_c are used to adjust the trade-off between fitting the two different data sets and satisfying the constraints. Their values are obtained on a trial-and-error basis to insure that the fits to two data sets are not strongly degraded. In our procedure, all inversions start with random initial fault models with total slips equal to the result of the point source inversions (e.g., CMT solution). The inversions with individual datasets and no constraints are first performed to determine the possible maximum improvements, which is then used to normalize the err_{wf} and err_{st} in the future combined inversion. The smoothing constraints are also normalized with the value of the initial models. After this process, the weights W_{st} and W_c become dimensionless.

We choose a particular kind of the simulated annealing inverse method (SA), called the heat-bath algorithm [*Rothman*, 1986], to search for the best finite-fault model in the whole model space. Compared to other simulated annealing algorithms, it has two advantages. First, it acts by perturbing the objective parameters one by one. When we perturb the parameters of one subfault, the response of the rest of the fault can be saved, so we can speed the calculation of the objective function by nearly 100 times. Second, as *Sen and Stoffa* [1995] pointed out, it is good for problems with a large numbers of free parameters. This method permits us to simultaneously invert for the slip amplitude, slip direction, rise-time, and rupture velocity, efficiently.

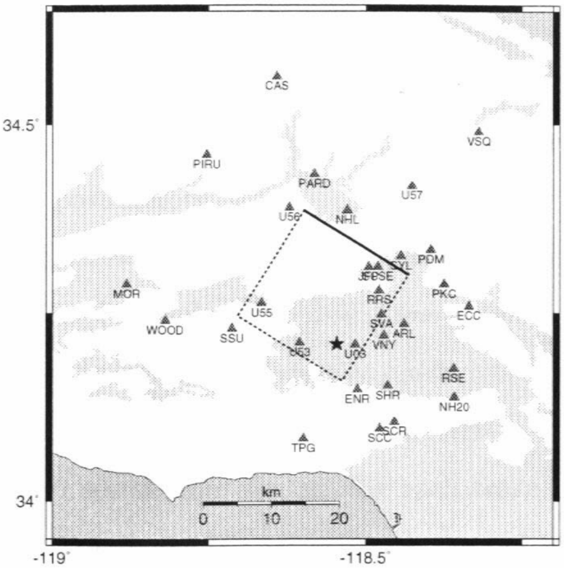

Figure 2.6: The projection of the 1994 Northridge earthquake fault plane and strong motion stations (triangles). The star shows the location of the epicenter.

2.5 Resolution analysis

In this section we check the resolution and robustness of our new procedure by inverting synthetic data sets for two different source geometries. In the first test, we stress the reliability of the inversion method by returning to the fault geometry of Northridge earthquake discussed earlier. In the second test, we emphasize the effect of uncertainty caused by choice of local velocity structure on synthetic waveform and GPS measurement assuming the geometry appropriate for the 1999 Hector Mine earthquake dataset.

2.5.1 Strong motion inversion: 1994 Northridge earthquake

We use the station distribution and fault geometry of the Northridge earthquake (Fig. 2.6). In this event, 30 strong motion stations were within 40 km from the hypocenter, forming a good near source station coverage. It should be pointed out that a good distribution of station is always one of the fundamental conditions for a detailed analysis. The test rupture model is modified from finite fault inversion analysis of the Northridge earthquake by *Wald and Heaton* [1994] (Fig. 2.7). The fault plane is 18 km along-strike and 24 km down-dip and the dip and strike of it are 40° and 122°, respectively. We divide it into 196 subfaults with dimensions 1.29 km by 1.71 km, and each of them is represented by four parameters mentioned above. In total, there are 784 free parameters.

We use the hard-rock velocity model [*Wald et al.*, 1996] to generate the synthetic seismograms applying the FK code [*Zhu and Rivera*, 2000] with a 0.1 sec sample interval. In the inversion, we match the wavelet coefficients for the scale region from 0.8 sec to 12.8 sec or in the period region from 0.04 Hz to 1.2 Hz. Because we only try to fit 12.8 sec to 25.6 sec seismic signals, for each trace, we need fit to 31 to 63 wavelet coefficients. The total number of data points used in the inversion is about 4200.

During the test, bounds of 0 to 3 meters are allowed for the slip amplitudes; the rise-times vary from 0.5 to 3.5 sec at a 0.5 sec interval; the rake angle is given the range of 70° to 140°; the rupture time of each subfault is bounded by the time for a rupture to reach the subfault from the hypocenter traveling for 2.4 km/sec to 3.6 km/sec. The inversion begins with a random model in the above domains. We let the inversion stop if the improvement is less than 0.05 percent in 20 iterations. During the inversions, we let the W_c be zero, so no smoothing or minimum moment constraints are used.

We show the inversion results of noise-free strong motion data in Figure 2.7c and 2.7d. It recovers nearly all details and validates the algorithm and approach we used. In the next inversion, when we add 5 percent Gaussian noise (the peak amplitude of noise is 5 percent of peak amplitude of synthetic data in time domain), the results are smeared (Fig. 2.7e and 2.7f). However, we found that the four parameters are affected differently. Rise time and rupture time, characteristics of fault that are related to frequency variation in seismograms, are relatively stable for noise. i.e., the rupture time contours are nearly wholly recovered and the variation within rise time is in one sample interval 0.5 sec. But absolute slip amplitudes and rake directions are affected.

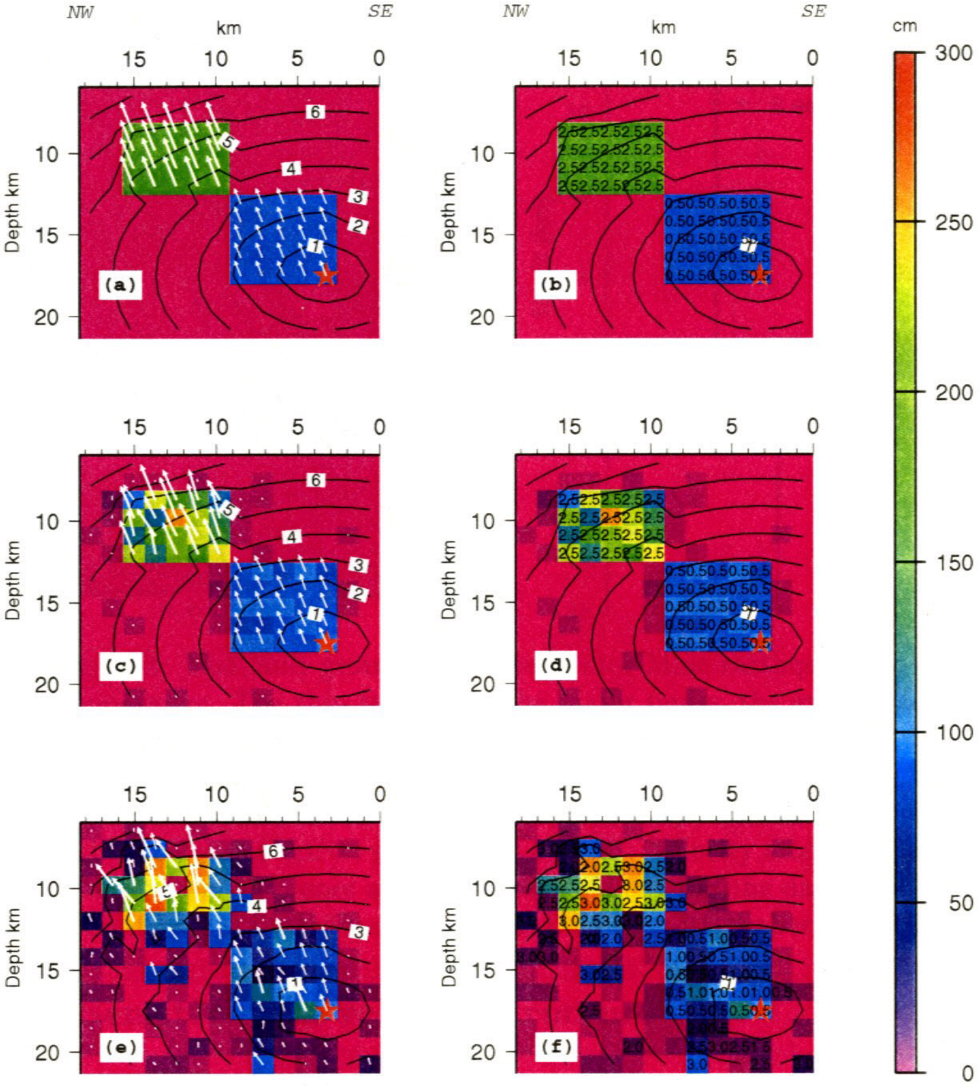

Figure 2.7: Comparison of finite fault inversions. (a) slip distribution and (b) rise time distribution of test model. (c) and (d) are results of noise free inversion; (e) and (f) are result of data contaminated with 5 percent Gaussian noise. The contours indicate the rupture initiations. The color shows the slip amplitude; arrows indicate the slip directions. In order to highlight the major features, we add a 0.4 m threshold before the plot, i.e., only when subfault with over 0.4 m slip, its rise time is plotted. Furthermore, the average rupture velocities of subfaults with less than 0.4 m slip is set to 2.6 km/sec since it is poorly constrained when slips are small.

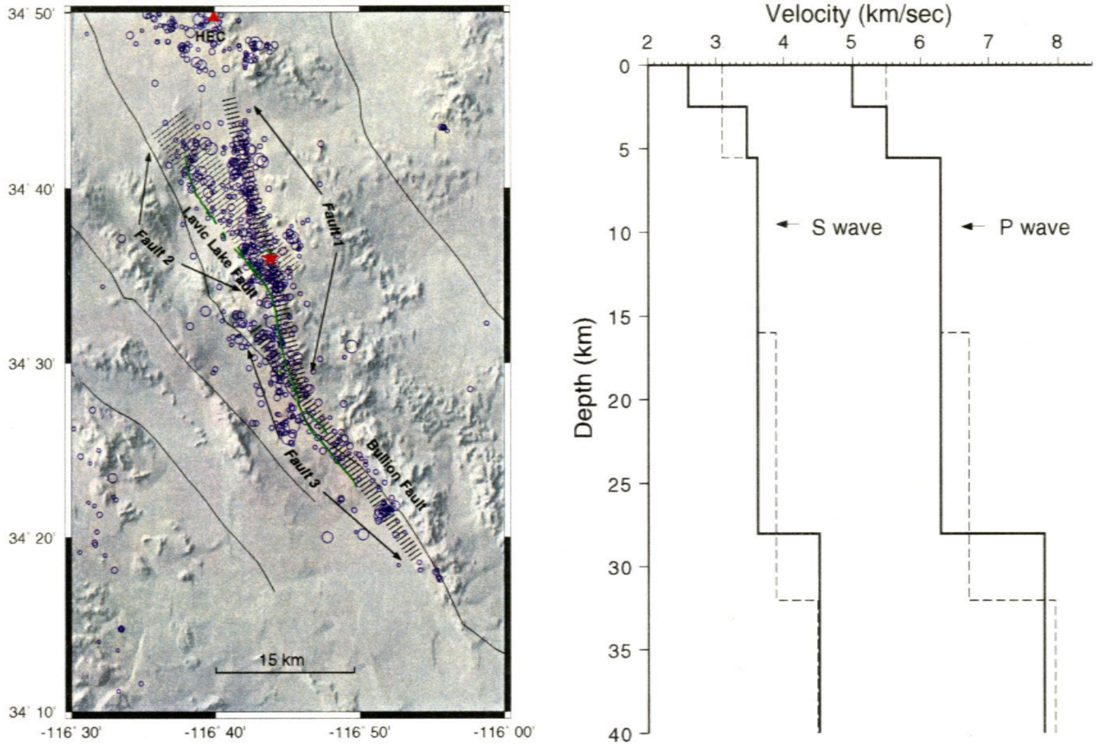

Figure 2.8: Left: Test fault geometry for the Hector Mine earthquake on a base-map of local topography. The thin lines show the major faults, the green trace indicates the mapped surface break, and a star is used to display the epicenter. The surface projections of the fault plane are presented with hatchured lines. The blues circles show the aftershock ($M_L > 2$, *Hauksson et al.*, 2002). The triangle in the north indicates the location of TriNet station HEC. Right: Velocity models. The solid lines show the Mojave model (Jones and Helmberger, 1998) and the dashed lines show the Southern California standard model (SoCal, Dreger and Helmberger, 1993).

2.5.2 Sensitivity to velocity structure

In recent work, *Wald and Graves* [2001] and *Graves and Wald* [2001] studied the importance of accurate Green's functions for finite fault source inversions. They found that inaccurate 3D Green's functions allow only partial recovery of the slip distribution even when the rupture velocity, rise time and rake angle are fixed. However a joint geodetic and seismic inversion allows for reasonable recovery of slip distribution. This analysis prompts us to discuss the effect of Green's function before performing a combined inversion of 1999 Hector Mine earthquake in Chapter 3.

It was pointed out that the velocity structure around the Hector Mine earthquake

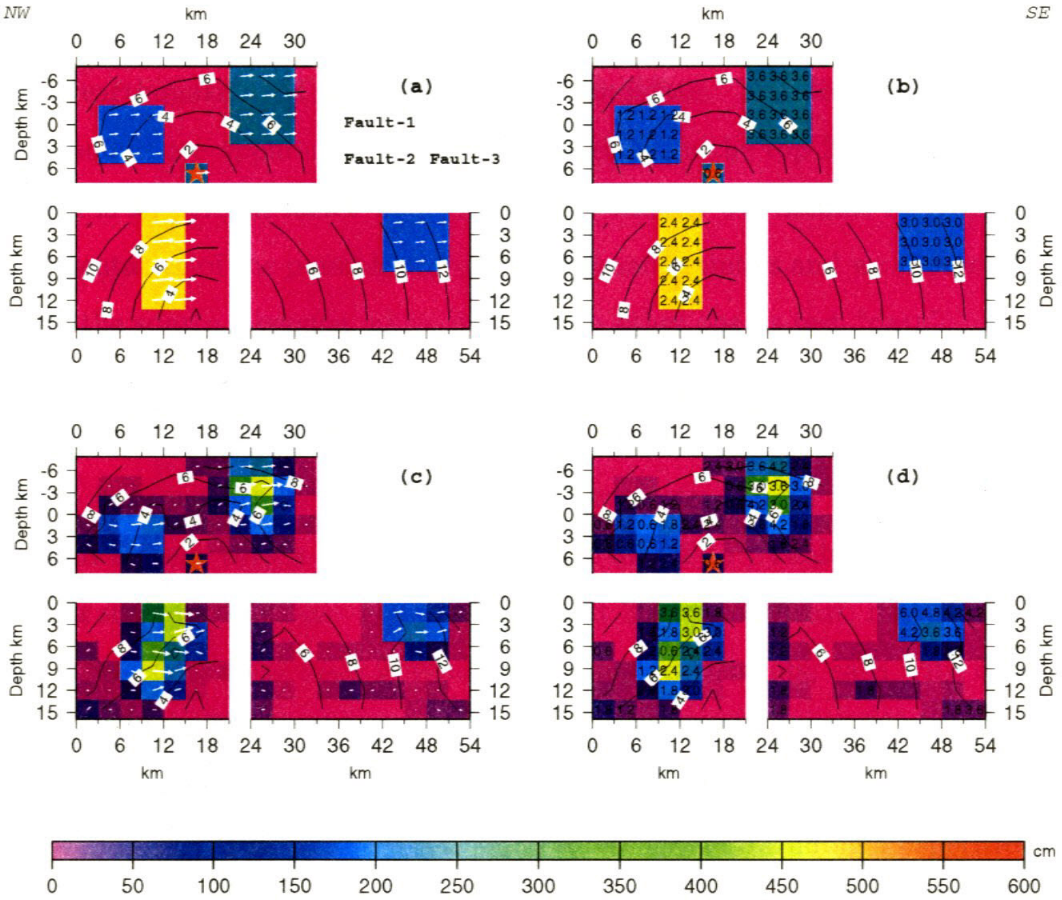

Figure 2.9: Cross section of the slip distribution of test models (top, a and b) and inverted models (bottom, c and d). The contours indicate the rupture time at a 2.0 s interval. The slip amplitudes are displayed with color. At the left (a and c), the arrows are used to show the rake angles; and in the right (b and d), the average rise time of each subfault is indicated. A 0.5 m threshold is used before the plot, i.e., if a subfault with less than 0.5 m slip, its rise time is not plotted and the average rupture velocity of the fault segment is used to calculate the initiation time.

is relatively simple [*Hauksson*, 2000]. The simple layered models can model the wavefield reasonably well. The southern California standard model (SoCal, *Dreger and Helmberger*, 1993), which is used in the automated source inversion for events in this region [*Zhu and Helmberger*, 1996], seems to be a good choice; while the Mojave model [*Jones and Helmberger*, 1998] was shown to work well in explaining the waveforms from the Landers aftershock sequence, with similar paths for the Hector Mine earthquake, and could be another candidate. The differences between these two models are apparent (Fig. 2.8), particularly in the top 2.5 km, where the Socal Model is 30 percent faster than the Mojave Model. We assume such differences are representative of the possible velocity model uncertainties and we choose one of them to do the source inversion while treating the other one as test "data".

We use the same data distribution and similar fault geometry as those used in the detailed analysis of the 1999 Hector Mine earthquake (Chapter 3). The fault geometry shown in Figure 2.8 consists of three fault segments: Fault 1 is in the central portion of fault system with a strike of 346° and a dip of 85°; Fault 2 is in the northwest, with a strike of 322° and a dip of 75°; Fault 3 is in southeast, its strike is 325° and dip is 85°. The total fault is subdivided into 168 elements, each with dimensions 3 km by 2.7 km. We use four parameters to determine the response of each subfault as mentioned above, so the total number of free parameters is 672.

Within this fault geometry, we build a test model including 4 asperities, and the slip on the rest of fault is set to zero. We fix the rake angles of all asperities to 175°, but each asperity has an individual rise time and slip amplitude. Moreover, the rupture velocities are also varied asperity to asperity. For instance, rupture front speed is only 1.8 km/sec for the asperity on fault 2. Finally, the total moment is 3.33×10^{19} Nm with the rigidity of the Socal Model, about one-half of that of the Hector Mine earthquake (Fig. 2.9a and 2.9b).

Records of 10 strong motion and 38 GPS stations (Fig. 2.10) are used. The azimuth coverage of strong motion stations is quite good, but we have only one station HEC whose epicentral distance is less than 30 km. In addition, 15 teleseismic P waves and 11 teleseismic SH waves are also used (Fig. 2.11).

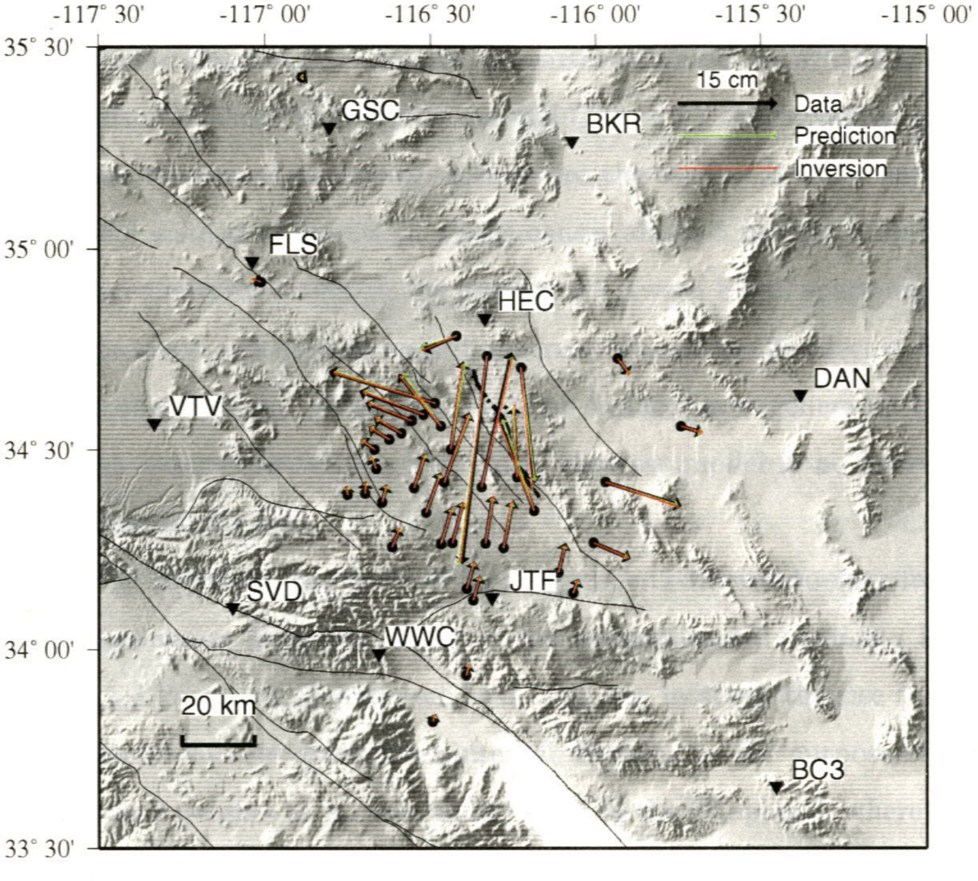

Figure 2.10: Distribution of strong motion (triangles) and GPS stations (circles). The major faults in this regions are plotted by thin lines, and the surface break during Hector mine earthquake is indicated by thick line. For each station, black arrow shows synthetic displacement generated form the test model and SoCal velocity model, blue one shows that from the test model and the Mojave model, and red one shows that from the inverted model and Mojave model. See text for details.

We use the SoCal model to build the test data of the aforementioned fault model. The strong-motion, teleseismic P or SH body-wave and the static displacements (Fig. 2.10, 2.11 and 2.12) of this layered model are generated with the synthetic methods developed by *Zhu and Rivera* [2000], *Yao and Ji* [1998], and *Xie and Yao* [1989]. Then, the Mojave model is used to make the Green's functions for the later inversions as we do in Chapter 3.

Before performing the inversion, we forward calculated the synthetic seismograms and static displacements with the test model (Fig. 2.9). As expected, the variations in teleseismic waveforms are small, and so are the static displacements. Using the Mojave model instead of the SoCal model causes about 5 percent amplitude error in static displacements even though the difference between a half space and the Mojave model can produce a 15 percent amplitude error. However, the effect is significant for the local strong motions, where the soft near-surface layer generated larger surface waves. With inaccurate velocity structure, the test model is no longer the model which can best fit the data.

During the inversion, the dislocation amplitude is allowed to vary from 0 to 8 m; the rake angle varies from 140° to 210°; the average rupture velocity is selected to range from 1.6 km/sec to 3.0 km/sec at 0.1 km/sec interval; the rise time is allowed to range from 0.6 to 6 sec at a 0.6 sec interval. Finally, for the purpose of comparison, we use the same weights as we used in the work in the Chapter 3, where $W_{st} = 1$ and $W_c = 0.1$.

The wavelet coefficients in a scale range 1.6 to 25.6 sec for teleseismic P waves and strong motion data, and 3.2 to 25.6 sec for teleseismic SH waves are used to constrain the slip model. For the closest station HEC, the coefficients of the wavelets with a scale of 0.8 sec are also used. The L1+L2 combined criteria is used to constrain the wavelet coefficients with scales over 3.2 sec, and the correlation function is used to constrain the fit to coefficients with scales of 0.8 and 1.6 sec. Finally, the GPS measurements offer 114 additional constraints to the slip distribution.

Three inversions with different initiation models are performed, and all inverted models have smaller objective function values than that of the test model. One typical result is given in Figure 2.9. The synthetics generated from this model are displayed in Figure 10 by red arrows, Figure 2.11 by red lines and Figure 2.12 by thin lines. Note that the inverted model matches the strong motion data much better than the test model (Fig. 2.11), but becomes worse at fitting the teleseismic data (Fig. 2.12). Finally, two models explain the GPS data equally well (Fig. 2.10).

Comparison between the test model and inverted model (Fig. 2.9) emphasizes the importance of a suitable velocity structure for source inversion studies. In a relative sense, the inversion for the slip distribution is more robust, the slip pattern is similar to the test model but is smeared. However, the recovery of the rise time and rupture velocity distributions are strongly affected by the inaccurate velocity structure. Fortunately, the influence can be reduced if we have near fault observations. For instance, in the four asperities, only that in the northern portion of Fault-1, which is near the closest strong motion station HEC, has a reasonable recovery of both rise time and rupture initiation contours. The resolution of the two asperities on fault 1 and 2 is also fairly good, but significant variations are also observed. For a more quantitative evaluation, we calculate five basic parameters: seismic moment, average slip, average rake angle, rupture velocity and rise time (Table 2.1). Because only the subfaults with larger dislocation amplitudes are well determined, the latter three parameters have been weighted with slip amplitudes.

$$V_m = \frac{\sum^j \sum^k D_{jk} * V_{jk}}{\sum^j \sum^k D_{jk}} \tag{2.20}$$

$$r_m = \frac{\sum^j \sum^k D_{jk} * r_{jk}}{\sum^j \sum^k D_{jk}} \tag{2.21}$$

$$R_m = \frac{\sum^j \sum^k D_{jk} * R_{jk}}{\sum^j \sum^k D_{jk}} \tag{2.22}$$

Here D_{jk}, V_{jk}, r_{jk} and R_{jk} dislocation amplitude, rupture velocity, rise time and rake angle of subfault jk, respectively.

The average retrieved values for the entire fault are well determined. About 10

Table 2.1: Sensitivity of finite source parameters to variation in velocity structure

Parameter	Fault 1	Fault 2	Fault 3	Whole Fault
Mo(10^{19} Nm)	1.47(1.56)	1.19 (1.32)	0.42 (0.45)	3.08 (3.33)
Slip Amplitude (m)	0.86 (0.87)	1.19 (1.20)	0.41 (0.31)	0.78 (0.75)
Rake angle (^{o})	174 (175)	179 (175)	172 (175)	176 (175)
Rupture speed (km/s)	2.3 (2.3)	2.0 (1.8)	2.7 (2.8)	2.23 (2.17)
Rise time (sec)	2.3 (2.7)	2.5 (2.4)	2.9 (3.0)	2.50 (2.60)

The numbers in brackets are the corresponding input values of the test model. The moments are calculated based on velocity models that generate the synthetic seismograms and static displacements. The subfault dislocation amplitudes are used as weights to calculate the weighted average rake angle, rupture velocity and rise time of whole fault and the three fault segments.

percent difference in entire seismic moment release is caused by the different shear moduli of the models because the average slip of inverted model is slightly larger than that of test model.

The effects of the inaccurate velocity model are apparent but still reasonably small when we consider the value of individual fault segments. The variations in rupture velocity are about 0.2 km/sec (fault 2) and the changes in rise time are less than about 0.4 sec (fault 1). The differences in the average slip and rake angle are negligible of faults 1 and 2, but become larger of fault 3, which is probably due to the fact that there is no strong motion station near fault 3.

With a large variation in velocity structure and few near-source strong motion stations, the uncertainty of individual subfaults becomes quite large. Outside of the region of the rupture initiation, it is difficult to have confidence in the characteristics of an individual subfault. However, if a group of subfaults have a similar characteristic, it is probably more reliable. In addition, given an approximate velocity structure, we can recover the overall pattern fairly well.

In summary, from our resolution test, we can make several observations. First, the recovery of the overall slip distribution is relatively robust. Second, rupture time and rise time distributions are perturbed by the inaccurate velocity structure. Third, while individual subfault parameters may vary from the true model, overall features

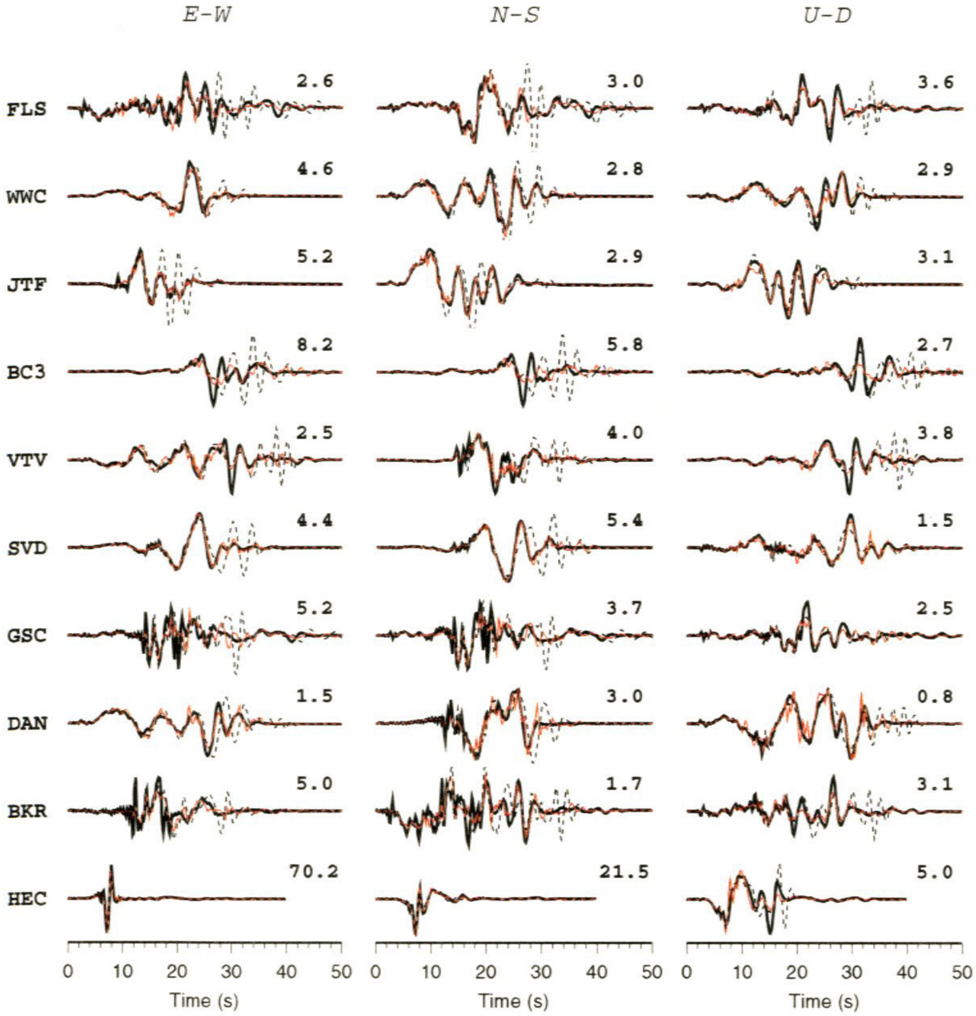

Figure 2.11: Strong motion velocity data (thick lines, generated by the test model and SoCal Model), forward prediction (dashed lines, generated by test model and Mojave model), and synthetics (red lines, generated by the inverted model and Mojave Model). The station names are indicated at the right of traces. The peak amplitudes of test data in cm/sec are indicated above the end of traces.

are still well resolved. Finally, in this particular test, the variation of the average rupture velocity of one fault segment is less than 0.2 km/sec, and the variation in rise time is about 0.4 sec.

2.6 Discussions

Inverting for source excitation with a limited knowledge of the earth structure certainly proves challenging. While the primary faulting parameters are easily described, the details of the rupture process remain elusive. Incremental improvements in resolving for source complexity will be possible in the near future with the extensive deployments of modern geodetic and seismic networks combined with space-based observations, but additional advances in the inversion process will also be beneficial. Here, we have added to the source inversion tool chest by examining the variation of frequency content with time. In particular, the simultaneous inversion using the geodetic data to determine the slip distribution, and the wavelet transform of the seismic data to address the temporal rupture properties, proves beneficial. In Chapter 3, we apply this method to study the complex slip history of 1999 Hector Mine earthquake in detail.

It is noteworthy that the approach suggested in this work only begins to take advantage of the wavelet transform. Wavelet transform theory suggest that signals should be seen in a 2D time-frequency plane, instead of a 1D time or frequency axis. The criteria that measure the difference between observed and synthetic signals could reflect this concept. Compared with the approach used in this work, which only weighted signals by the signal scales, it could be done with both the scales and positions. For instance, the L2 norm in the wavelet domain could be

$$e = \sum_j \sum_k W_{j,k}(o_{j,k} - s_{j,k})^2 \tag{2.23}$$

Where $W_{j,k}$ is the weight related to scale parameter j and position parameter k. With this approach, the prior knowledge of noise can be impacted in a fashion to "zoom in" on reliable signals and "zoom out" the large noisy contaminated signals by adjusting the weights. This approach will decrease the sensitivity to the velocity in some extent. Note that it is nearly impossible to accomplish this in the time or frequency domain alone.

Furthermore, since wavelet transform is a linear transform, it should be straightforward to apply this approach in other linear waveform inversion algorithms. Finally, the theory of wavelet transforms is still developing, and more wavelet atoms are being introduced. Since different wavelet atoms will focus on different qualities of seismic signals, such as time, frequency, phase, etc., introducing them into seismological studies will be helpful to better understand the earthquake rupture process.

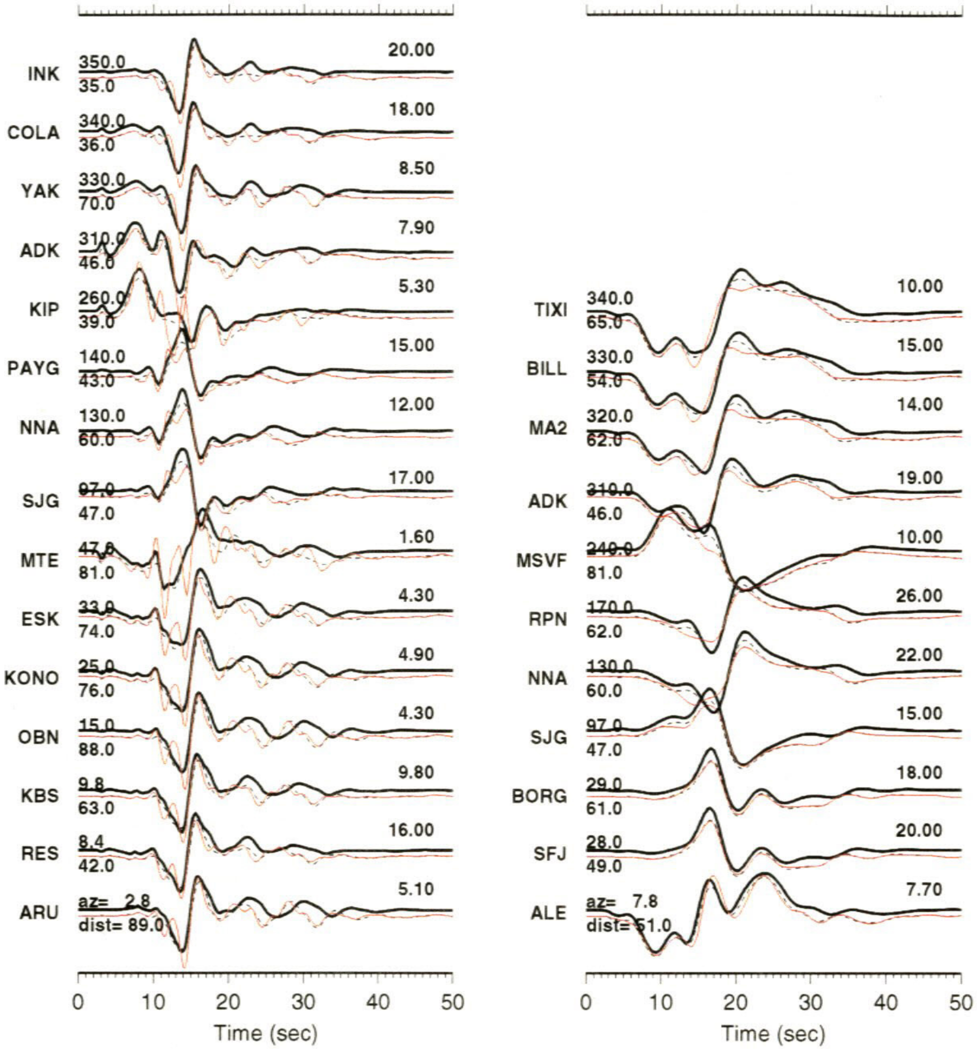

Figure 2.12: Teleseismic P and SH velocity data (thick lines, generated by the test model and SoCal Model), forward prediction (dashed lines, generated by test model and Mojave model), and synthetics (red lines, generated by the inverted model and Mojave Model). The station abbreviations are indicated at the right of each trace. The peak amplitudes of test data in millimeter/sec are indicated above the end of traces. The synthetic seismograms are slightly shifted in vertical for a better comparison. Comparison of P waves in the left column, and comparison of SH waves in the right.

Chapter 3 Source description of the 1999 Hector Mine, California, earthquake

3.1 Abstract

We present a rupture model of the Hector Mine earthquake (M_w 7.1), determined from the joint inversion of strong motion records, P and SH teleseismic body waves, Global Positioning System (GPS) displacement vectors, and measured surface offset. We solve for variable local slip, rake angle, rise time and rupture velocity of a finite fault model involving multiple segments. The inversion methodology developed in Chapter 2 combines a wavelet transform approach with a nonlinear (simulated annealing) algorithm. The final model is checked by forward simulating the Interferometric Satellite Aperture Radar (InSar) data. Our estimation to the seismic moment is 6.28×10^{19} Nm, which is distributed along three segments from north to the south, releasing 37, 41, and 22 percent of the total moment, respectively. The average slip is 1.5 m with peak amplitudes as high as 7 m. The fault rupture has an average rise time of 3.5 sec and a relatively slow average rupture velocity (1.9 km/sec) resulting in a 14 sec rupture propagation history. Our approach permits large variation in rupture velocity and rise time and indicates that rise time appears to be roughly proportional to slip and shorter rise times are associated with the initiation of asperity rupture. We also find evidence for nearly simultaneous rupture of the two northern branches.

3.2 Introduction

The 1999 Hector Mine, California, earthquake occurred in a remote, sparsely-populated part of the Mojave desert, only about 20 km east of the 1992 Mw 7.3 Landers earthquake. Both occurred within the eastern California shear zonne (ECSZ). Because most of faults in the ECSZ have low slip rates and major earthquakes repeat times are on the order of several thousands to tens of thousands of years [*Sieh et al.*, 1993], the occurrence of two magnitude 7 earthquakes within 7 years illustrates the complexity of the faulting interaction.

The Hector Mine earthquake occurred when major upgrades to the regional seismic network (*TriNet*) were underway [*Mori et al.*, 1999]. With the convenient real-time TriNet data set, the basic source information of this earthquake was obtained soon after it occurred. For instance, the focal mechanism was determined within a minute (Zhu and Helmberger, 1996). After a few hours, even a preliminary single-plane finite-fault model was determined using waveform data from the *TriNet* array [*Dreger and Kaverina*, 2000].

However, as the accumulation of information continued, discrepancies became apparent. One discrepancy is the difference between the surface rupture (Fig. 3.1) and the preliminary finite-fault model. Most of the surface break (more than 5 meters at some sites) was centered around the hypocenter, but is nearly zero in the preliminary finite fault model (Dreger and Kaverina, 2000). In contrast, in the 1992 Landers earthquake, the initial models constrained by the seismic data were consistent with the geological observations (e.g., *Kanamori et al.*, 1992; *Dreger*, 1994).

Dreger and Kaverina [2000] approximated the complex fault geometry of the Hector Mine earthquake by a single plane, because the goal was to obtain a finite fault model in near real time. Here, we want to show that the discrepancies can be explained by considering the fault geometry and rupture initiation. The surface break data and aftershock pattern are, in fact, used to determine the complexity of the fault plane geometry. The local strong motion data, teleseismic body waves, and GPS data are combined to constrain the slip history of the Hector Mine earthquake.

One of the unique advantages of the strong motion records of this event is the timing. Traditionally, strong motion instruments were designed for engineering purposes and thus they did not record continuously. They were triggered when the ground accelerations were larger than a particular threshold, and the absolute trigger time was often not preserved. Usually, it is assumed that the instruments are triggered by the

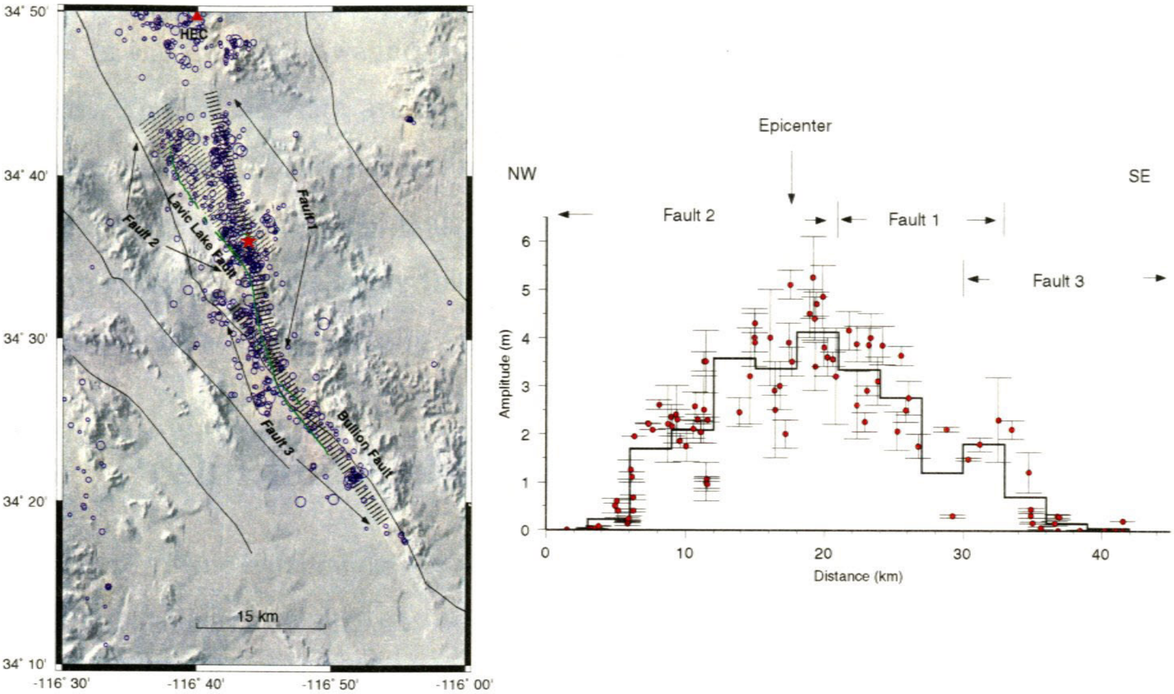

Figure 3.1: (a) Fault geometry for the 1999 Hector Mine earthquake with a base map of local topography. The thin lines show major faults. The green traces indicate the mapped surface ruptures, the southern portion is associated with the Bullion fault, and the northern portion is the Lavic Lake fault. The star indicates the epicenter. Aftershocks ($M_L > 2$, *Hauksson et al.*, 2002) are plotted as blue circles. The grid of black dots is the surface projection of the point sources used to generate the fault response. The red triangle in the north is the location of *TriNet* station HEC. (b) Horizontal component of the slip on the surface rupture of the Hector Mine event. The red dots with error bars are surface measurements (Scientists, 2000). The heavy line segments indicate the amount of the slip as averaged along 3 km intervals.

direct P waves (e.g., *Hartzell and Heaton*, 1983). This assumption may not be valid because most large earthquakes start with a foreshock or nucleation phase [*Ellsworth and Beroza*, 1995]. However, most of the strong motions of the Hector Mine earthquake were recorded continuously at the broadband *TriNet* stations. Careful analysis of the beginning portions of the broadband records in absolute time was essential for determining the nucleation and evolution of this earthquake.

While the constraint to the slip distribution can be improved by additional geodetic data (*Graves and Wald*, 2001; *Wald and Graves*, 2001), the resolution of rupture evolution is still dependent on the wavelength of radiated seismic waves. Generally, the shorter the wavelength is, the higher the potential resolution is [*Aki and Richards*, 1980]. In the Chapter 2 we incorporated the wavelet transform into a finite fault inversion. The seismic data are further separated into multiple wavelet channels with different frequency bands. The lower frequency channels are used to constrain the larger scale characteristics of fault, and high-frequency channel help to constrain the pattern recognition. We apply this approach here in order to recover simultaneously the spatial variations of the slip amplitude, rake angle, rise time and rupture time.

3.3 Preliminary observations and fault Geometry

The Hector Mine earthquake ruptured two fault zones, the Bullion fault and Lavic Lake fault. The latter one was mapped only after this earthquake (Fig. 3.1). The overall length of surface faulting is approximately 41 km, but most of the surface slip is along the central part of Lavic Lake fault, where the surface rupture changes direction. The strike changes from 322° in the north segment to 346° in the south. The maximum amplitude of surface slip (5.2 m) was measured near the intersection of the two surface breaks [*Scientists from the U.S. Geological Survey et al.*, 2000]. Surface slip along the Bullion fault (southern branch) is complex and smaller than along the Lavic Lake fault.

It is noteworthy that the surface slip in the northern portion shows two branches. In addition to the aforementioned larger surface break in the west, there is a small patch of surface rupture positioned directly above the hypocenter and along the northward extension of the middle portion (Fig. 3.1a). This implies that the Lavic Lake fault separates into two faults. This observation is supported by the aftershock pattern, which shows two planes in the northern part of the Lavic Lake fault [*Hauksson et al*, 2002]. One plane has an azimuth of 322° trace and a dip angle of 75°. The other plane strikes 346° and is slightly steeper (85° to the east). While the former plane corresponds to the larger surface break, the hypocenter that determined by local short period data is on the latter fault plane. The two-fault system can also explain the large variations in point source solutions obtained by several groups (Ta-

Table 3.1: Focal mechanisms of the 1999 Hector Mine earthquake

Groups	$\theta(^o)$	$\delta(^o)$	$\lambda(^o)$	$M_o \times 10^{19}$ Nm
Harvard	336	80	174	5.98
NEIC	329	83	171	5.4
TriNet	331	77	179	3.4
USB	343	70	175	4.01

θ, δ and λ are the strike, dip and rake of the double couple fault plane which is close to the strike of the fault surface break, respectively.

ble 3.1). Even though all of the solutions indicated that the Hector Mine event is a nearly pure strike-slip earthquake, the strike directions vary between 329° to 343°, roughly in the middle of two fault planes determined by the aftershock pattern. We show later that the 20° difference in fault direction strongly affects the waveforms at the closest station, HEC.

3.4 Fault parameterization

Based on the information mentioned above, we separate the rupture into three segments (Fig. 3.1). Fault 1 is the central part of fault system with a strike of 346° and a dip of 85°. Fault 2 is the northwestern segment, with a strike of 322° and a dip of 75°. Fault 3 is the southeastern segment with a strike of 322° and a dip of 75°. We let fault 1 extend north of its junction with fault 2, and fault 3 also extends north of its junction with fault 1 to guarantee the full coverage of the possible slip regions.

Here, the maximum depth of fault planes is fixed to be 16 km because preliminary inversions with the bottom at 25 km did not show important deeper slip (> 1 m). We use the epicenter from *TriNet* (34.597°N, -116.27°E) and let the main rupture nucleate in fault 1. The three fault segments are further divided into 168 subfaults with dimensions of 3 km by 2.7 km. And four parameters, dislocation amplitude, rake angle, rise time, and rupture velocity are used to control the response of each subfault (Chapter 2). Thus we have 704 variables needed to solve in the inversions.

The Mojave velocity model (Fig. 3.2, *Jones and Helmberger*, 1998) is in very

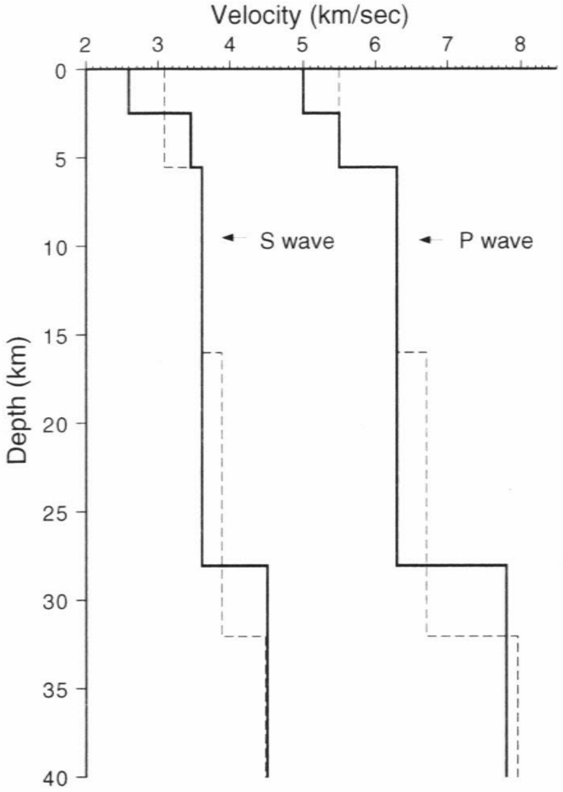

Figure 3.2: Layered velocity models. The solid lines show the Mojave model [*Jones and Helmberger*, 1998] and the dashed lines show the Southern California standard model (SoCal, Dreger and Helmberger, 1993).

good agreement with the average East Mojave model in the recently developed 3D tomography model of *Hauksson* [2000]. It was also found to work well in explaining the waveforms for Landers aftershock sequence [*Jones and Helmberger*, 1998]. Due to the similar station event paths for the Landers aftershocks and the Hector Mine earthquake, we choose this model to calculate the subfault Green's functions (Chapter 2).

The simulated annealing method [*Sen and Stoffa*, 1991] is applied to find a global minimum of the error function represented as

$$err_{wf} + W_{st} \times err_{st} + W_c(constraints) = \text{minimum} \tag{3.1}$$

Here, err_{wf} and err_{st} are objective functions of the seismic waveforms and static displacements, respectively. Two types of constraints are chosen: one that minimizes the difference in slip on adjacent subfaults, and a second that minimizes the total moment [*Hartzell et al.*, 1996]. The W_{st} and W_c are weights to the static criteria and constraints. Note that the objective functions and constraints have been normalized for the convenience of discussion (Chapter 2).

After performing the test runs with larger ranges but rough intervals, the inversions presented here are constrained in the following ranges: the dislocation amplitude of each subfault is allowed to vary from 0 to 800 cm, and the rake angle can vary from 140° to 210°. The average rupture velocity is selected to range from 1.6 km/sec to 3.0 km/sec at 0.1 km/sec intervals. Finally, the rise time is allowed to change from 0.6 to 6 sec at 0.6 sec intervals.

3.5 Data sets

In this study, both seismic waveform data and geodetic data are used to constrain the fault model. The combination can offer a more uniform near-source coverage of the faults and a more broadband frequency range of information (D.C to 0.8 Hz) than the individual data sets.

Table 3.2: Strong motion data

Sta	Lat (^{o})	Lon (^{o})	Dist (km)	Az (^{o})	Affi	W(UD)	W(NS)	W(EW)
HEC	34.829	-116.335	26.24	345.92	TriNet	1.5	4.0	4.0
BKR	35.269	-116.070	76.45	13.38	TriNet	1.0	1.5	1.5
DAN	34.637	-115.381	80.96	86.84	TriNet	0.5	1.0	1.0
GSC	35.302	-116.805	92.23	327.92	TriNet	0.5	1.0	1.0
SVD	34.104	-117.097	94.17	234.40	TriNet	1.0	1.5	1.5
VTV	34.567	-117.333	97.79	268.15	TriNet	1.0	1.5	1.5
BC3	33.655	-115.453	128.89	144.35	TriNet	0.5	1.0	1.0
JTF	34.130	-116.314	52.43	184.93	CDMG	1.0	1.5	1.5
WWC	33.990	-116.657	76.76	208.07	USGS	0.5	1.0	1.0
FLS	34.970	-117.039	81.75	300.42	USGS	0.5	1.0	1.0

3.5.1 Waveform data

We use strong motion data from 10 *TriNet* stations (Table 3.2 and Fig. 3.3). These observations provide good azimuthal coverage, but only one station is less than 30 km from the epicenter of the mainshock, and most epicentral distances are between 75 km to 100 km. The lack of near source stations limits the inverse resolution and robustness to the accuracy of the velocity structures used.

Most of the data were recorded on the broadband acceleration channels of *TriNet* stations. We de-convolve the instrument responses to obtain the ground velocities. However, the E-W component of record at station HEC was contaminated by the possible station tilt and by an aftershock that occurred about 60 sec after the mainshock. These data were corrected by removing a linear trend. The data of stations WWC, JTF and FLS were high-pass filtered at 0.02 Hz to remove the uncertainty at the lower frequency, then integrated to velocities. All data are filtered by a 4-th order, two-pass Buttonworth filter to less than 1 Hz, then resampled to a sample interval of 0.2 sec.

All strong motion data are aligned by the first arrivals of P wave. For continuous recording instruments, including all *TriNet* broadband stations, it was easy to identity the first arrivals. For the records in the triggered strong motion stations WWC and

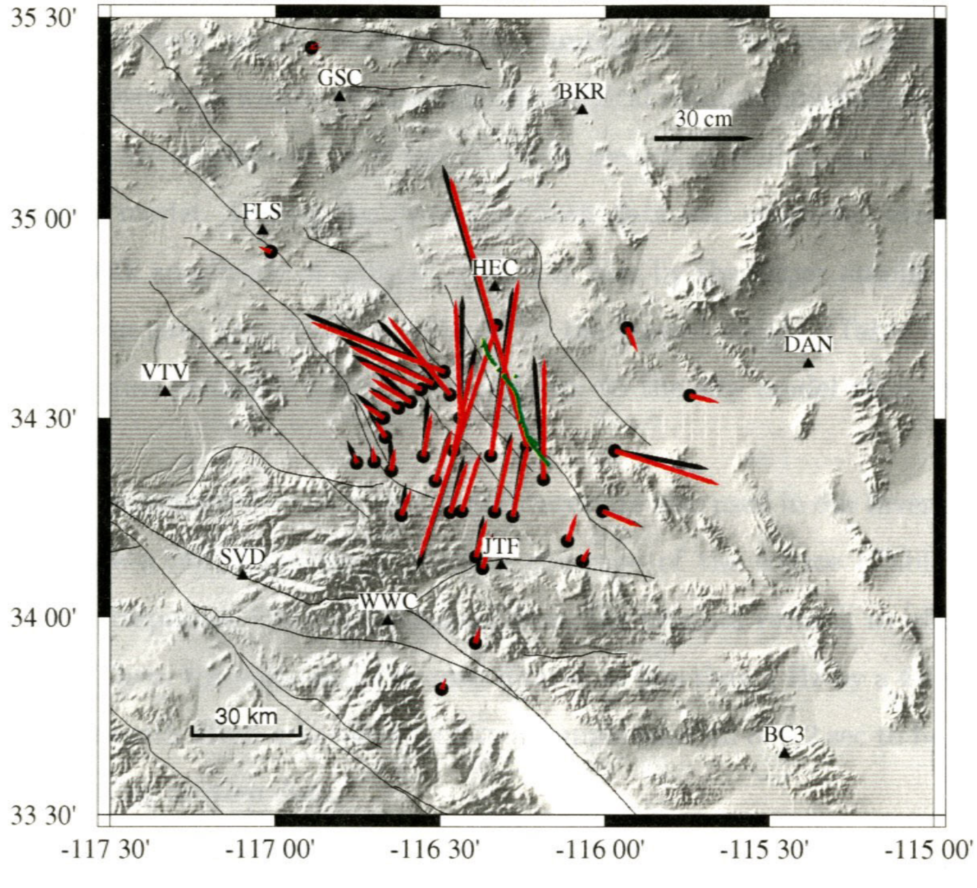

Figure 3.3: Distribution of strong motion (triangles) and GPS stations (circles). Thick lines show the surface rupture of the Hector Mine earthquake. Comparison of the horizontal GPS data (black arrows) and synthetic static displacements (red arrows) generated by the preferred model is also presented.

JTF, the exact first arrival times are not available so we use the Mojave velocity model to estimate them. Such values are adjusted by performing a preliminary inversion based on weighting only the other stations and then comparing the synthetic and observed waveforms at triggered stations. The times are not changed during the subsequent inversions.

Note that we did not rotate the records to fault normal and parallel because the extended fault length makes rotation ambiguous. The horizontal components were given twice the weight of those for the vertical components because the vertical components are dominated by P waves, which are not as well modeled by our simple 1D velocity model. During the inversion, both data and synthetic were normalized with the peak amplitude of data to avoid any bias by the larger amplitude stations. Moreover, we gave the closest station HEC the largest weight (Table 3.2), because such close-fault records have larger sensitivity to the slip model than more distant data.

Fifteen teleseismic P-waves and 11 SH-waves are also used in our inversions. These data provide a well distributed azimuth coverage of the source (Table 3.3). The instrument responses were de-convolved from the original records to obtain ground velocities. Then, the data were low-pass filtered to less than 1 Hz by a 4-th order two-pass Butterworth filter, and resampled to a sample interval of 0.2 sec to be compatible with the strong motion data.

Because of the existence of a small foreshock (Appendix A), the teleseismic arrival times are very difficult to pick. We use the Iasp91 travel-time table [*Kennett and Engdahl*, 1991] to make first order estimations. However, these estimations alone are not sufficient to be used directly in a waveform inversion. For instance, in the study of the 1992 Landers earthquake, *Wald and Heaton* [1994] found that the uncertainty in P wave arrival time could be over 2.0 sec. Considering the small spatial separation between two earthquakes, we believe that there is about the same amount of uncertainty in the current dataset. Because of the small take-off angles of the teleseismic phases, such uncertainty in the arrival time estimations can cause important errors in inverted models, e.g., a 1.0 sec error in teleseismic P arrival time implies a

Table 3.3: Teleseismic Data

Stations	Lat (^{o})	Lon (^{o})	Dist (^{o})	Az (^{o})	P-delay(s)	S-delay(s)
ARU	56.43	58.56	89.18	2.84	0.6	-
ALE	82.50	-62.35	51.32	7.81	-	-3.2
RES	74.69	-94.90	41.55	8.40	0.6	-
KBS	78.93	11.94	62.89	9.81	0.4	-
OBN	55.11	36.57	87.63	15.19	0.0	-
KONO	59.65	9.60	76.03	25.06	0.0	-
SFJ	67.00	-50.62	49.16	28.23	-	0.0
BORG	64.75	-21.33	61.24	29.15	-	2.8
ESK	55.32	-3.21	73.82	33.18	0.4	-
MTE	40.40	-7.54	80.67	47.11	-0.2	-
SJG	18.11	-66.15	47.38	96.89	-0.6	0.2
NNA	-11.99	-76.84	59.55	133.79	-0.8	1.2
PAYG	-0.67	-90.29	42.68	139.64	0.0	-
RPN	-27.13	-109.33	61.78	172.98	-	3.4
MSVF	-17.73	178.05	81.28	241.50	-	5.4
KIP	21.42	-158.01	38.81	261.53	-1.8	-
ADK	51.88	-176.68	45.90	311.42	-2.2	-3.2
MA2	59.58	150.77	62.24	324.97	-	1.8
YAK	62.03	129.68	70.11	332.76	-2.8	-
COLA	64.87	-147.85	35.83	337.60	0.8	-
BILL	68.06	166.45	53.64	332.95	-	1.2
TIXI	71.65	128.87	64.69	341.48	-	-2.4
INK	68.31	-133.52	35.21	349.01	0.6	-

over 10 km horizontal mislocation of the corresponding seismic radiation source. For this reason, we first use the strong motion data to obtain a preliminary fault model, then apply the model to predict the teleseismic synthetic seismograms. Improved best alignments are estimated by comparing the synthetic and observed waveforms. Unfortunately, this procedure reduces the independence of teleseismic data to some extent.

During the inversions, the number of wavelet coefficients used depends on the quality of the Green's functions (Chapter 2). We use the wavelet coefficients with scales not smaller than 1.6 sec for most of strong motion and teleseismic P data, which is similar to a low-pass filter with a corner frequency at 0.6 Hz (Chapter 2). For the records of the closest station HEC, we put the coefficients with a scale of 0.8 sec into inversions. In contrast, for the teleseismic SH-wave data, the high frequency cut-off is only 0.3 Hz (the scale $s \leq 3.2$ sec) because the 4.0 sec attenuation factor removes most higher frequency energy.

3.5.2 Geological and geodetic data

The field observations of the Hector Mine earthquake were made during the week following the mainshock [*Scientists from the U.S. Geological Survey et al.*, 2000]. Since there is no evidence of large afterslip, it is a good data set to help constrain the fault model. The slip measurements along the surface rupture were made at evenly distributed points along the fault. For our finite fault model, we average the detailed measured slip on 3 km by 2.7 km subfaults because the distant and lower-pass filtered seismic data do not have enough resolution to distinguish smaller spatial heterogeneities. Following work of *Wald and Heaton* [1994], we average the measured surface slip within the 3-km intervals along surface subfaults (Fig. 3.1b). This averaging reduced the peak amplitude from 5.2 m to 4.1 m.

GPS data is another important dataset for our study. We use the horizontal and vertical displacements at 36 monuments of the Southern California Integrated GPS Network (SCIGN) and the U.S. Geological Survey (USGS). Only stations with more

Table 3.4: Comparison of observed and synthetic GPS displacements

Site	Position(^{o})		U-D (cm)		N-S (cm)		E-W (cm)	
site	Lon.	Lat.	Obs.	Syn.	Obs.	Syn.	Obs.	Syn.
LAE1	-116.557	34.574	-7.10	-2.17	10.40	8.38	-20.80	-18.85
LAE2	-116.522	34.589	-1.30	-2.43	13.90	11.30	-28.00	-25.33
LAE3	-116.487	34.618	0.50	-2.00	17.70	15.08	-42.40	-40.29
LAE4	-116.329	34.734	-19.30	-16.81	-74.50	-70.83	-24.20	-23.26
LAW1	-116.588	34.542	-2.30	-1.67	11.60	7.03	-12.50	-11.92
LAW2	-116.624	34.527	-0.20	-1.35	6.10	5.41	-8.60	-9.24
LAW3	-116.669	34.502	0.40	-0.99	7.40	4.10	-8.60	-6.39
LAW4	-116.665	34.454	0.10	-0.53	8.30	4.95	-5.40	-3.07
MEEK	-116.617	34.258	0.10	0.80	9.70	7.58	1.40	2.96
OLDD	-116.698	34.391	-0.60	-0.08	4.70	4.58	-1.40	-0.54
OLDW	-116.752	34.389	-0.90	-0.15	6.70	3.25	-3.00	-1.05
RICH	-116.469	34.264	7.26	1.44	17.20	14.93	4.18	5.06
SANH	-116.279	34.255	1.05	1.94	23.07	21.92	3.66	4.62
CTMS	-116.370	34.124	1.40	1.44	10.50	10.23	3.13	2.78
LDES	-116.433	34.267	1.70	1.60	17.96	17.29	5.73	5.42
OAES	-116.068	34.141	0.21	0.50	2.80	4.09	2.48	2.00
WIDC	-116.392	33.935	0.33	0.87	5.26	4.68	1.57	1.22
BSRY	-117.012	34.919	-1.00	-0.77	1.53	1.38	-3.57	-3.57
PSAP	-116.494	33.819	0.71	0.68	3.15	3.07	1.11	0.91
AMBO	-115.742	34.559	-2.50	-1.10	-1.60	-2.13	7.00	8.51
0808	-115.933	34.728	2.60	0.21	-5.40	-7.25	1.30	3.02
SCP2	-115.969	34.419	-0.90	-1.47	-5.50	-10.22	28.40	31.66
SCP1	-116.006	34.267	-1.30	-0.41	-4.80	-4.72	12.00	11.40
MESQ	-116.113	34.193	0.20	0.84	6.90	8.09	2.30	2.60
SCP4	-116.186	34.348	-2.40	-0.29	37.60	36.56	-3.10	0.15
SCP5	-116.237	34.432	-10.10	-5.34	85.40	81.52	-25.70	-23.22
6050	-116.334	34.266	3.10	1.92	23.90	22.29	5.00	5.28
SCP6	-116.345	34.407	1.70	-2.13	51.00	53.54	6.60	8.35
PAXU	-116.390	34.153	2.80	1.52	12.70	11.42	2.20	3.28
LEDG	-116.439	34.502	-1.30	-2.69	37.10	35.61	0.60	-1.44
MAUM	-116.458	34.419	0.40	-0.19	32.10	26.41	6.70	5.87
7001	-116.469	34.560	-2.00	-2.97	22.80	23.60	-22.20	-18.86
LAZY	-116.514	34.344	0.60	0.87	15.30	15.30	4.30	4.90
MEAN	-116.550	34.405	1.70	0.15	17.90	12.98	1.30	2.36
6056	-116.647	34.370	-0.30	0.19	10.30	6.64	-0.40	0.97
GOL2	-116.889	35.425	-1.00	-0.07	1.90	-0.17	-1.00	-0.58

than 3 cm of horizontal displacement are chosen to guarantee a good signal noise ratio. Since many of GPS stations are operated to study the post-seismic motion of the Landers earthquake, the coverage on the western side of the Lavic Lake fault is better than that on the eastern side (Fig. 3.3).

3.6 Finite fault modeling

The slip distribution determined with the GPS data should be similar to that constrained by the seismic data, simply because the source is unique. Unfortunately, we found that there is significant difference existed when we study the Hector Mine earthquake with the individual data sets. While this result can be explained by the assumption that there was large afterslip during the first few days after the mainshock, we will show another scenario here that the difference disappears if the main rupture initiation is deeper than the hypocentral depth determined by the regional seismic network, *TriNet*. After addressing this problem with the inversions constrained by GPS and strong motion data, we will present our preferred finite fault model which is constrained by combining teleseismic body wave, strong motion, GPS and surface break observations.

3.6.1 Hypocentral depth sensitivity

We begin with a finite fault inversion constrained by the GPS data and surface offset. The first model is determined using the GPS data only. Then the surface offset information is added to invert the second fault model, i.e., the shallowest elements were allowed to vary roughly 50 percent from the assigned surface offset values as averaged along each shallow subfault (Fig. 3.1). The smoothing and minimum moment constraints are used. The W_c is 0.2 in both cases. The two slip distributions are plotted in Figure 3.4a and 3.4b, respectively.

Both models explain the GPS observation very well. χ^2 values are 152 and 157 for the models constrained by GPS only and GPS and surface rupture, in contrast with the initial value of 4256. Comparing the two slip models, it is clear that as the slip on the shallowest subfaults is constrained by the surface break, the slip on the deeper subfaults is amplified. Hence the surface offset data are a good compliment to the sparse GPS measurements. However, when we have many close fault static observations, for example, InSar data [*Rosen et al.*, 2000], the surface offset constraint may not be as critical.

The total moment of both models is around 6.2×10^{19} Nm, which is slightly larger than the seismic moment determined by the Harvard CMT (Table 3.1). Most of slip occurs on the two branches of Lavic Lake fault, where the slip amplitudes are up to 7.0 m. Finally, it is noteworthy that there is significant slip around the hypocenter location determined by the *TriNet* (the red star in Fig. 3.4) no matter whether we use the surface constraint or not. In addition, this result should not be affected by the initiation position of the main rupture.

The slip distribution determined by the seismic data is no longer independent of the location of the hypocenter. Instead, the slip pattern near the epicenter is strongly affected by the location of the rupture initiation. Unfortunately, such information was not well determined in this case presumably due to the existence of a foreshock [*Dreger and Kaverina*, 2000]. Even though the strong motion records at the local stations constrain the epicenter of the main rupture initiation really well, the depth is poorly known due to the lack of near-source stations (Appendix A). Here, we try to investigate whether we can take advantage of the initiation independence of the static field and obtain a good estimate of the nucleation depth by performing the combined inversions of both strong motion and the GPS data starting at different depths. If the earth model was correct and there is no afterslip, the model initiating at the correct depth should fit the strong motion and the GPS data and the surface offset observations simultaneously.

We perform four inversion tests with individual rupture nucleation depths from 6.7 km to 14.8 km. The shallow depth is close to that estimated by *TriNet*; the latter depth corresponds to maximum depths of the seismicity in the ECSZ. Since local strong motion data clearly show that the signal of the main rupture arrives 2 sec after the first arrival (Appendix A), we delay the rupture starting time a few seconds

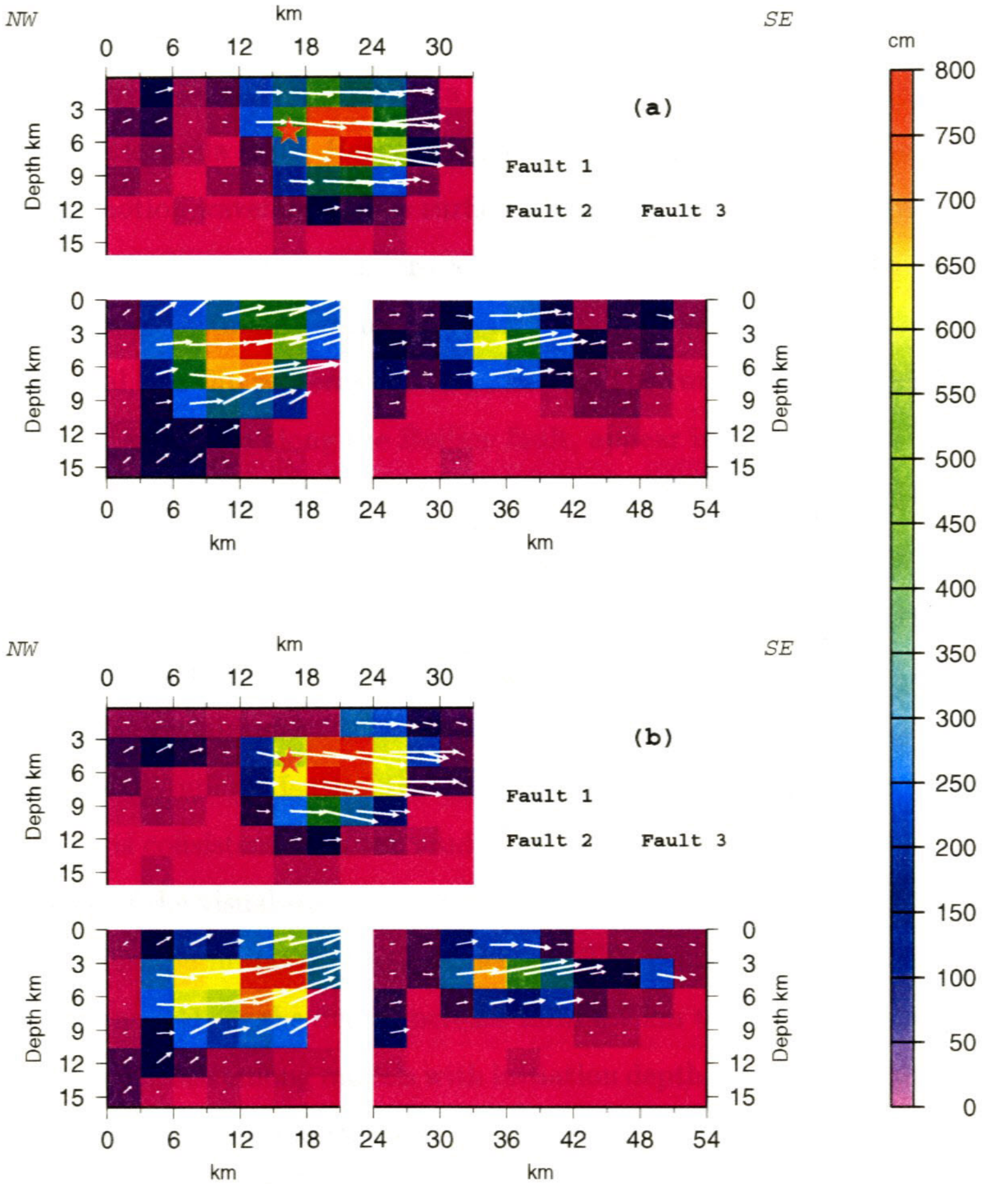

Figure 3.4: Cross section of the slip distribution determined from modeling the GPS data. The color indicates slip amplitude and arrows show the slip direction. The relative positions of three fault segments are indicated in the upper-left corner. (a) Slip distribution constrained by the GPS data only. (b) Slip distribution constrained by GPS plus surface offset measurements.

relative to the hypocentral time (09:46:41.1, *TriNet*) to ignore the foreshock. Even though the rupture delay time will change when the main rupture initiation becomes deeper, the variations are small. For example, when the nucleation depths vary from 6.7 km to 14.8 km, the rupture delay times change from 2.0 sec to 1.8 sec.

We weight the strong motion data 10 times more than that of the GPS data, i.e., $W_{st} = 0.1$ in formula (3.1). Hence, the models determined are mainly constrained by the strong motion waveforms. The surface break data are not used in these tests. The inverted slip patterns are summarized in Figure (3.5), where the red stars indicate the positions of the main rupture nucleation.

In general, the slip patterns are very similar. The two large asperities on the faults 1 and 2, and small slip along the Bullion fault, appear in all inversions. However, the slip pattern near epicenter does change with the hypocentral depths. The edge of the large asperity on fault 1 is about 6 km away from the epicenter in the model with a 6.7 km initiation depth. Then the area of large slip moves toward the epicenter when the depth of the hypocenter increases. When the hypocenter is over 12 km, the slip distribution is visually close to the result of the GPS inversions. The four models also indicate a really unique feature that the slip on the subfaults near the hypocenter is small. This is consistent with the study of *Kaverina et al.* [2000].

Because of the visual similarity, it should be expected that the fit to the GPS data is better when the initiation becomes deeper. The value of χ^2 decreases from 539 to 430 to 337 and 341, as the depth increase form 6.7 km to 14.8 km, respectively. Note the sharp variations among models with initiation depths from 6.7 km to 12.1 km, and little variation between models with the depths 12.1 km and 14.8 km. Similarly, the models with the deeper hypocenter also match the strong motion data better than the shallower ones. However, the improvements are not very large, and the variation in the waveform fit for different depths is less than 8 percent. Such a result is probably due to the fact that most of the strong motion stations are over 75 km away from the epicenter. The model with an initiation depth of 12.1 km fits the waveform data best, even though the model with an initiation depth at 14.8 km fits only slightly worse.

We also compare the slip on the shallowest subfaults with the corresponding aver-

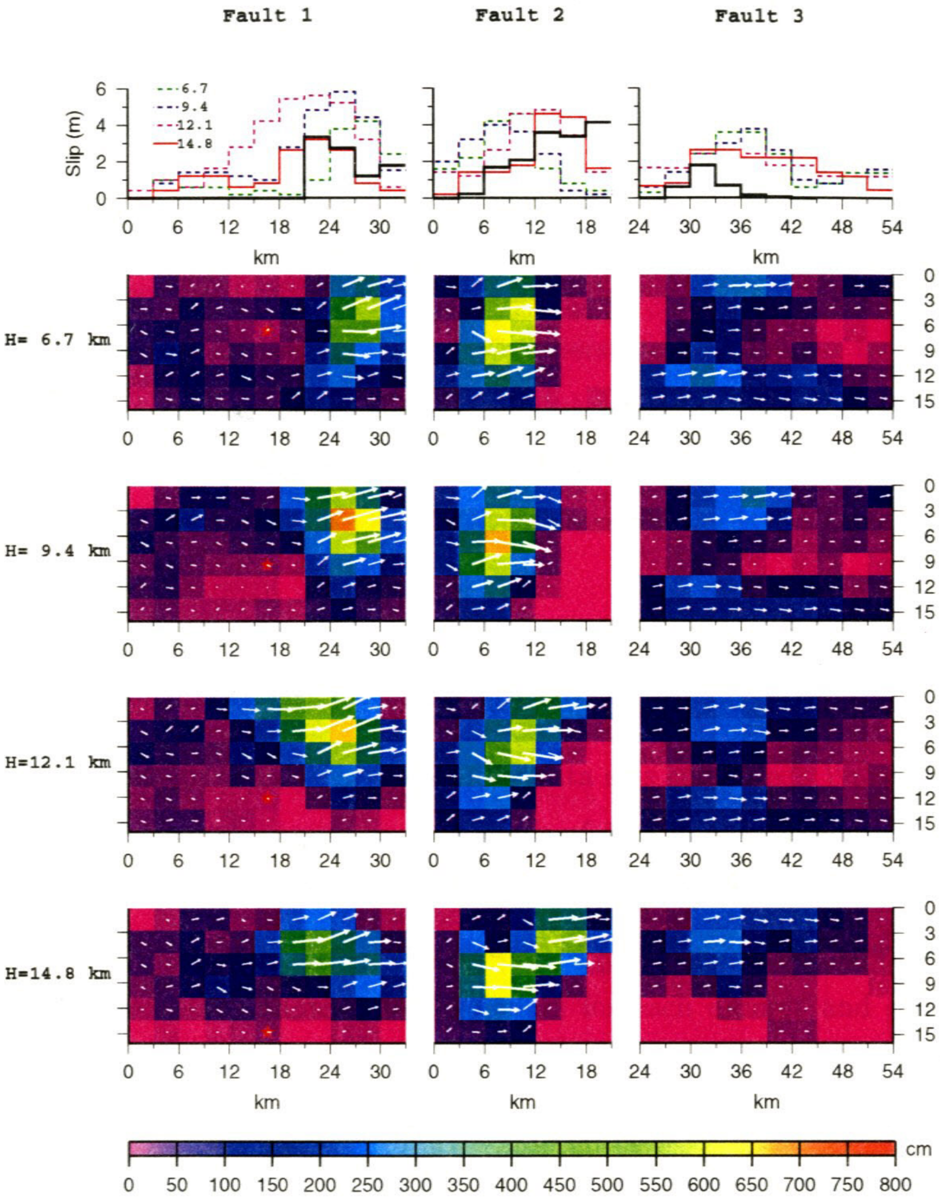

Figure 3.5: Inversion sensitivity to rupture initiation depth. The four fault slip models have different hypocentral depths, and are constrained by strong motion and GPS data. The red stars indicate the positions of main slip initiations. The arrows show the slip directions. The color in each pixel displays individual subfault slip amplitude. The predicted surface slips are compared with subfault-averaged observations (black lines, see Fig. 3.1) in the top diagrams.

age surface offsets from Figure 3.1 (Fig. 3.5). This indicates that the model with an initiation depth of 14.8 km fits best. In contrast, the model with a 6.7 km initiation depth has a "hole" around the epicenter where the slip is only about 1 m, compared with average observed surface slip of 4.1 m.

Hence, modeling of the multiple data sets favors the deeper initiation. Since there are not very large differences in fits to both waveform and GPS data between models with a hypocenter at depth of 12.1 km or 14.8 km, we choose the deeper one simply because it can explain the surface break better. Similarly, *Wald et al.* [1990] assigned the initiation of the 1987 Superstition earthquake to be 9 km based on waveform modeling, though the hypocentral depth determined by the short period seismic network was 2 km. *Abercrombie and Mori* [1994] reported that the location of the large energy initiation for the Landers earthquake is 4-5 km deeper than the network location.

3.6.2 Preferred finite fault model

We now present an inversion with all four data sets combined. We assume that the beginning of larger slip initiates at a depth of 14.8 km, and choose to initiate the inversion 1.8 sec after the hypocentral time (09:46:41.1) (see Appendix A). Since the number of data is greatly increased because of combined data set, a main difficulty was to determine the relative weight factors for each dataset and constraints. In this study, we obtain them by trial and error to insure that none of data sets are strongly degraded. The values of W_c and W_{st} are 0.1 and 1.0, respectively. The preferred inverted model is shown in Figure 3.6. Because the effects from a subfault with a small slip are generally small to both the seismic and static data, the inverted uncertainties in its rise time and rupture velocity are, in turn, usually large. Thus, when we plot our inverted rise times and rupture velocities, only the values of the subfaults with over 0.5 m slip are used.

The synthetics generated fit the data quite well. For the GPS data, the χ^2 estimate is 230 (Fig. 3.3). The synthetic seismograms are also consistent with the velocity

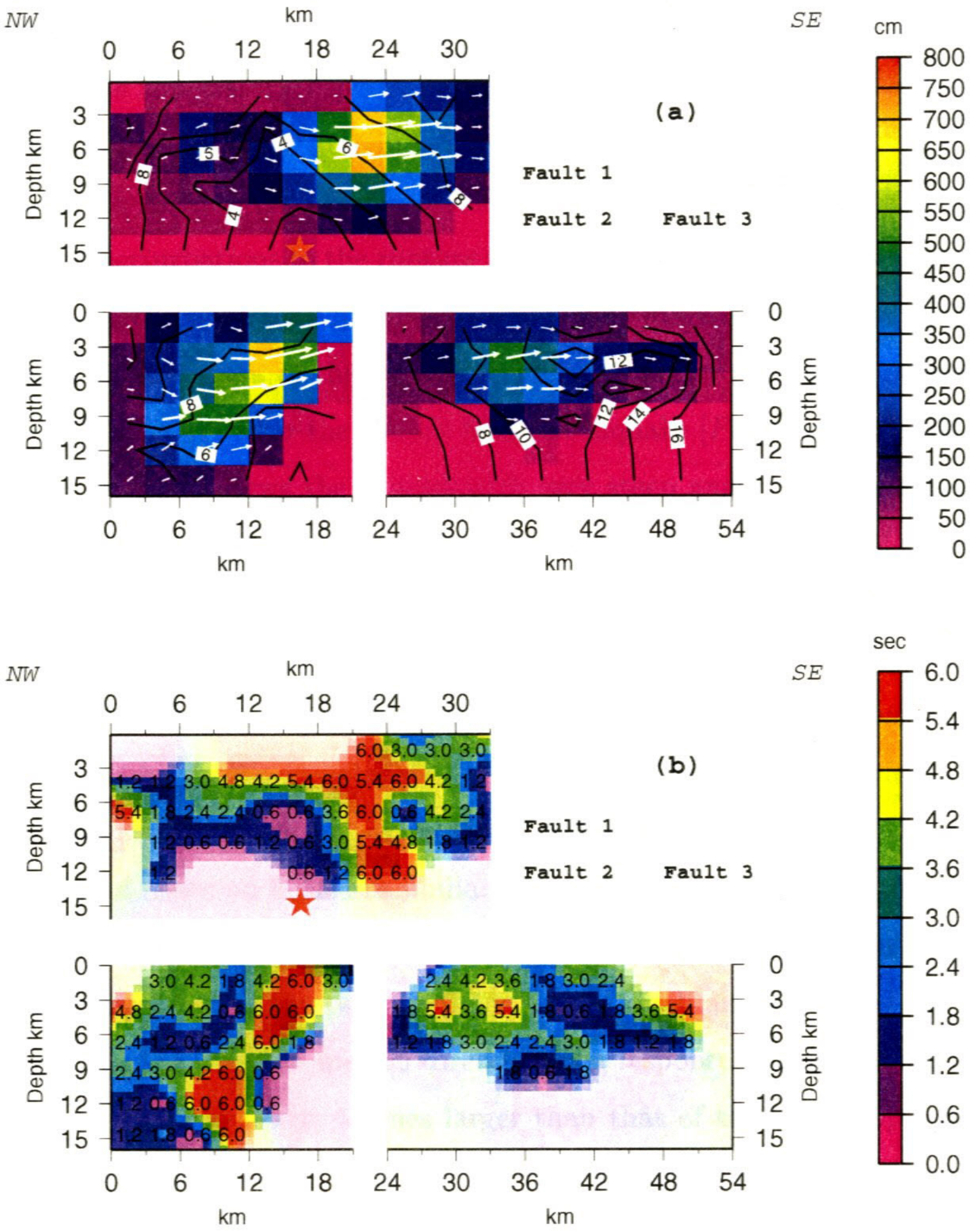

Figure 3.6: Cross section of the slip distribution determined from inverting combined strong motion, teleseismic, GPS, and surface rupture data. The Mojave velocity structure is used. The relative positions of three faults are indicated in upper-right corner. A red star indicates the hypocenter. For plotting, we require a 50 m minimum slip threshold, i.e., if a subfault has less than 50 m slip, the average rupture velocity of the fault segment is used to calculate the initiation time. (a) Slip distribution and rupture initiation time. The slip (cm) is displayed by the color bar. Arrows indicate the rake directions. The contours show the rupture time at 2.0 sec intervals. (b) Rise time distribution. The rise time values of subfaults with over 50 cm slip are also indicated.

strong motion and teleseismic P and SH records (Fig. 3.7 and 3.8).

Before the interpretation of the preferred model, we would like to know its limitations. The slip history depends on the velocity structure chosen in our study as indicated by the synthetic test in Chapter 2 and an inversion of the real data (Appendix B). In general, the effects on the slip and rise time distribution are relatively minor, but perturbations to the rupture time contours are not. For the same purpose, we forward predict the InSAR data in Figure. 3.9. InSAR data measures the surface motion in the direction of the radar line of sight during a time interval one month before and four days after the Hector Mine earthquake [*Fialko et al.*, 2001]. Because the radar generally views the ground with very steep angles, the measurements are usually more sensitive to the vertical motion than the horizontal. More accurately, only the horizontal motions in the direction normal to the ground projection of the satellite trajectory have contributions [*Rosen et al.*, 2000]. In this case, the satellite moved 194° to the north, and looked at the ground with an angle varied from 17° to 23° to the east. We calculated the ground displacements with the layered Mojave model, and then convert them to the motions in radar line of the sight. The predicted and observed fields are similar in general (Fig. 3.9). The apparent discrepancies around the south end of the fault 1 are probably caused by the uncertainty in estimating the dip-slip components. Due to the small angle between the extension of fault 1 and the satellite motion direction, the response of the unit dip slip in the radar line of sight is about 4 times larger than that of the strike slip motion. The dip-slip motion is generally small in this nearly pure strike slip event and hard to determine accurately with our current data sets because of the lack of the close-fault strong motion stations and the large observed error in GPS vertical measurements. Hence, the further improvement is possible if we include the InSAR data set in our inversion.

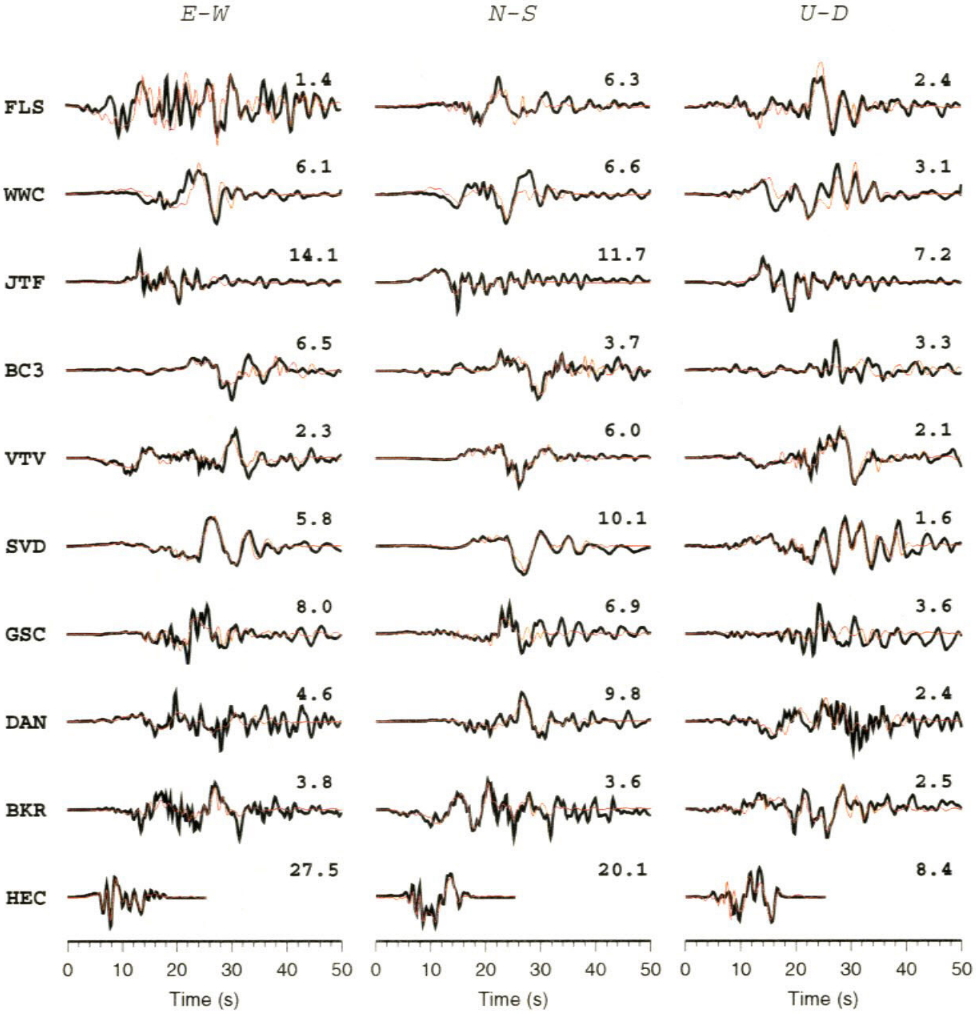

Figure 3.7: Comparison of the strong motion observations (thick lines) and synthetic seismograms (thin lines) generated by the preferred model. The station names are indicated at the right. The data are aligned by the P arrival-time. The peak amplitudes of observed records (cm/sec) are indicated above the end of the traces. The corresponding synthetic seismograms are plotted at the same scale of the observed data.

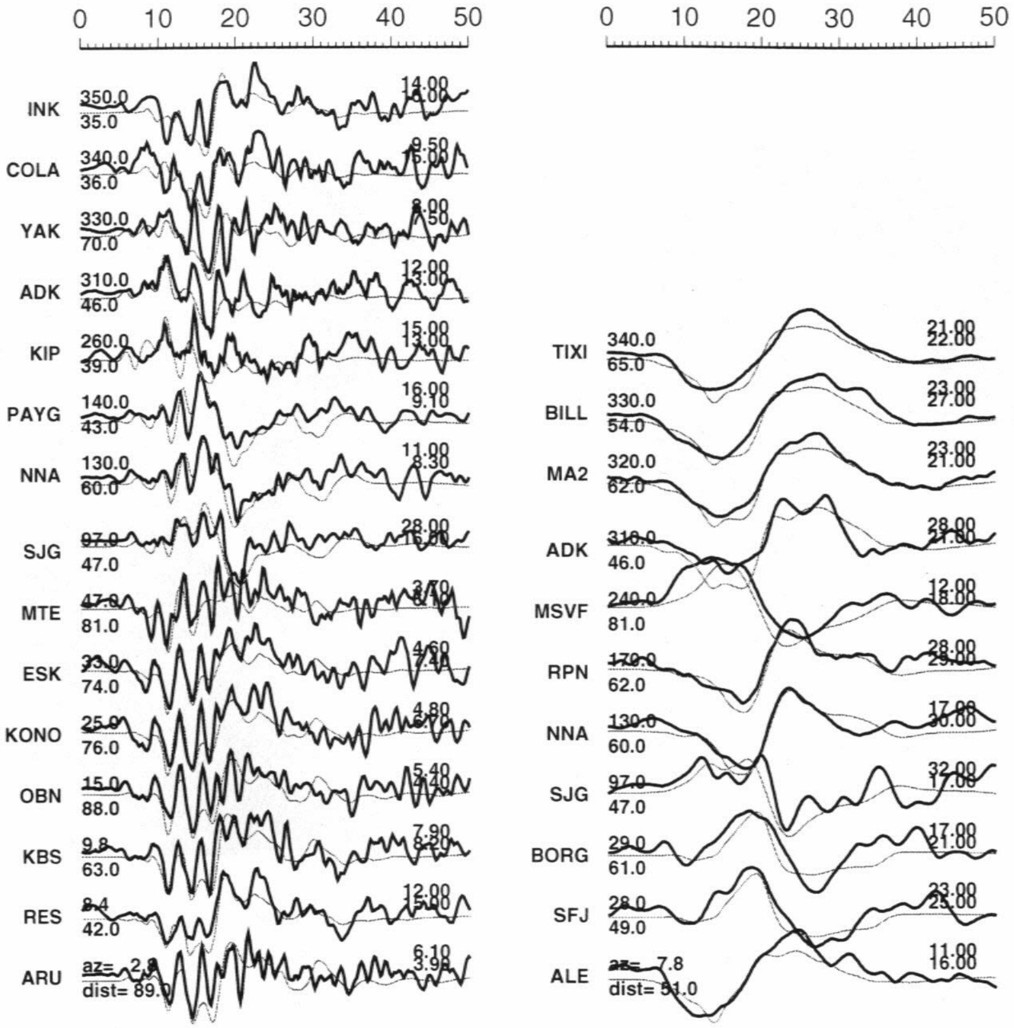

Figure 3.8: Comparison of the teleseismic velocity records (thick lines) and synthetics (thin lines) generated by the preferred model. The left column shows the comparison of teleseismic P-waves and the right column shows SH-waves. The station names are indicated to the right of traces along with the azimuths and epicentral distances in degrees. The peak amplitudes in millimeter/sec were indicated above the end of each trace with the upper number for the data and lower number for the synthetics.

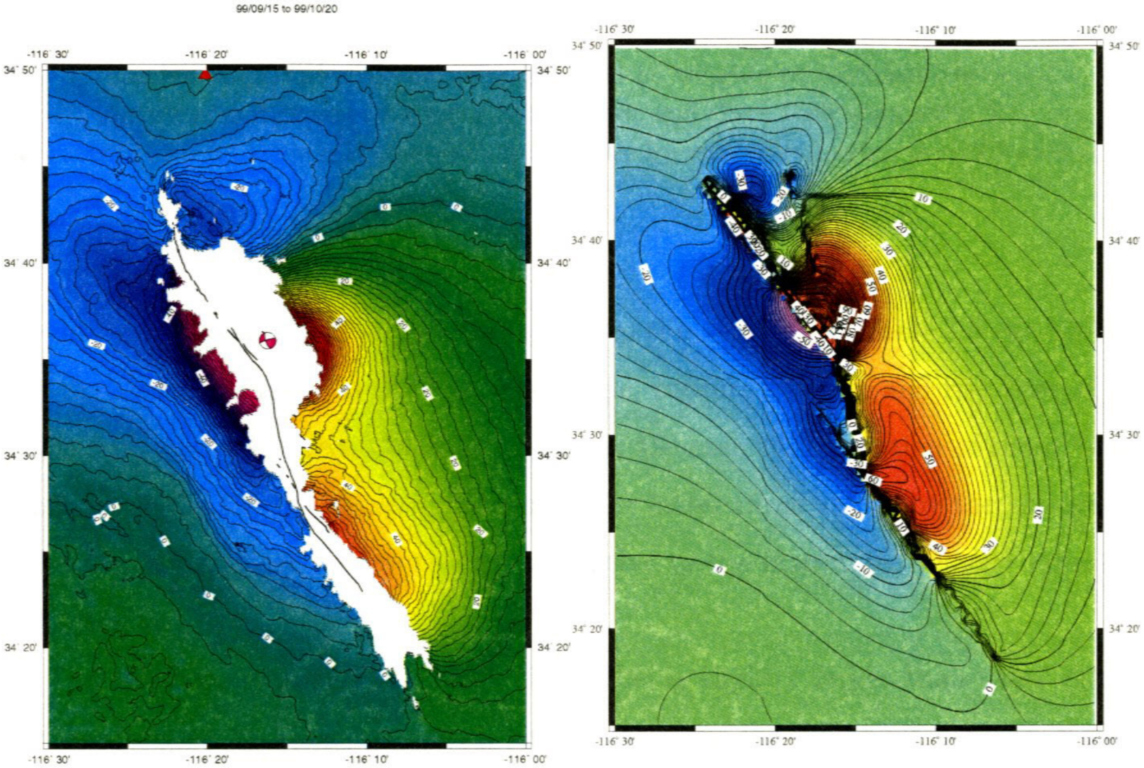

Figure 3.9: Left: Synthetic Interferometric Aperture Radar (InSar) data of the 1999 Hector Mine Earthquake. The azimuth of satellite track is S140°W. The satellite look angle is in 17-23 degrees to the west. The contours (cm) indicate the displacement field in the direction of the radar line of sight. The surface rupture is displayed by black lines. The epicenter is indicated by the focal mechanism. In the white region, the spatial variation of the co-seismic displacement is too large to be measured accurately. Right: The synthetic InSar displacements predicted by the preferred slip model. The Mojave model is used to generate the static field. For simplicity, we approximate the look angle as 20^o.

Table 3.5: Summary information of Hector Mine earthquake

Parameter	Fault 1	Fault 2	Fault 3	Whole Fault
Moment (10^{19} Nm)	2.55	2.30	1.32	6.28
Dislocation (m)	1.6 (2.6)	2.3 (3.0)	0.9 (2.0)	1.5 (2.6)
Rake Angle (^{o})	178	172	178	175
Rupture Velocity (km/s)	1.8	1.8	2.1	1.9
Rise Time (s)	3.7	3.7	2.8	3.5

The dislocation amplitudes of subfaults are used as weights to calculate the average rake angle, rupture velocity and rise time of whole fault and three fault segments. The numbers in brackets are the average dislocation amplitudes for subfaults having over 0.5 m slip.

3.7 Results

We discuss the results of the preferred model in this section. In Table 3.5, we summarize the averaged values of the slip, rake angle, rupture velocity and rise time of the whole fault and the individual fault segments. Because the resolution of those values depends on the slip amplitudes, we weight the latter three values by the slip amplitudes. Such values were shown to be insensitive to the inaccurate velocity structure (Chapter 2).

The total moment is 6.28×10^{19} Nm. This is slightly larger than other results discussed earlier in Table 3.1, which likely represents the difference between a point source and a finite fault approach with multiple fault planes. The 175° average rake angle also agrees well with previous analyses. The average slip amplitude over the entire fault is only about 1.6 m, but 98 percent of the moment is released on the subfaults with slip amplitudes more than half meter. The average slip on these subfaults increases to 2.6 m. Furthermore, since the three fault segments overlap, after we project the slips of three fault segments into a single plane, the average slip increases to 3.5 m in the top 12 km. The rise times are roughly proportional to the slip amplitudes, and the average slip velocity is about 0.8 m/sec. The average rupture velocity over whole fault is only 1.9 km/sec (or 53 percent of shear wave velocity), much lower than more typical values of about 75 to 85 percent of the shear velocity [*Heaton*, 1990].

The moment releases for the fault segments 1, 2, and 3 are 41, 37 and 22 percent of the total, respectively. The strike slip component still dominates the slip in three fault segments, but there is a larger thrust component on fault 2 (14 percent). Both faults 1 and 2 have slower average rupture velocities of about 1.8 km/sec, even though the distributions are not uniform. Their average rise times are about 3.7 sec. On the other hand, fault 3 (Bullion fault) has a relatively faster local rupture velocity (>2.1 km/sec) and a shorter rise time (2.8 sec). These results may imply that the dynamic processes of the Lavic Lake fault and Bullion fault are different.

3.8 Rupture history

The subfault initiation time can be calculated with inverted rupture velocities of individual subfaults. Because the rupture time is resolved only for subfaults with significant slip, when we plot the result, for a subfault with slip less than 0.5 m, we use mean rupture velocity averaged over the corresponding fault segment (Table 3.2) instead. The initiation time is depicted by contours with 2.0 sec intervals (Fig 3.6).

We give the rupture velocity substantial freedom. The average rupture velocity between hypocenter and rupture region can vary from 1.6 km/sec to 3 km/sec. With this approach, the local rupture front speed can be as much as 4.5 km/sec. Furthermore, there is no "causal" constraint that a subfault further from hypocenter should rupture later than one that is closer. Thus the local rupture velocity can be negative. However, a subfault with a negative local rupture velocity, will be indicated by non-sequential initiation time contours (Chapter 2). In the combined inversion model, the rupture is orderly in the substantial slip regions along fault 1 and 2. However, we find such features on the fault segment 3, where the surface rupture data imply a complex rupture process as discussed below.

The main rupture initiated on fault 1, which represents the east branch of the Lavic Lake fault. It then bilaterally propagated in both directions with different rupture velocities. The slip was small during the first 2-3 sec, then the asperity south of the hypocenter started to rupture. Fault 2 was triggered at about the same time and ruptured northward. Significant slip on fault 3 began after about 10 sec. The small slip amplitude along the northern end of fault 3 may not be a reliable feature because of the lack of close-in data. The total rupture propagated for about 14 sec and more than 70 percent seismic moment was released by the two large asperities on faults 1 and 2 during the first 10 sec.

The slip history near the initiation region is probably well resolved by the seismic data. During the Hector Mine mainshock, both slip amplitude and rise time on the initiation region are relatively small (Fig. 3.6). The rise time is around 1 sec, in contrast with 3.7 sec average rise time of the fault 1. The rupture initiation of asperity on fault 2 is also accompanied by a short rise. These two results are well constrained by the high frequency observations in the station HEC (Fig. 3.10). A shorter rise time at the beginning of rupture has been reported in the studies of several other larger earthquakes, e.g., Northridge earthquake (e.g., *Wald et al.*, 1996; *Hartzell et al.*, 1996). Because of the limitation of the inversion, we can not remove the possibility that the real derivative rise time function is actually a sharp triangle function followed by a long but small amplitude tail. Such an observation would reflect the strong high-frequency radiation at the boundary of the asperity as suggested by the theoretic analysis of the dynamic crack rupture (e.g., *Madariaga*, 1983).

The rupture history of fault 3 is different than that of the fault 1 and 2. It has the fastest average rupture velocity and shortest rise time among the segments. However, the resolution test (Appendix B) also indicates that inversion result in this region is strongly sensitive to the velocity structure. And, the mapped surface break bifurcates into two distinct branches about 1 km apart at the southern end (*Scientists from the U.S. Geological Survey et al.* [2000]; Fig. 3.1), which implies a more complex fault geometry than the single plane we assumed. This may be the reason that we found some "early" subfaults, i.e., subfaults rupturing earlier than surrounding ones. Unfortunately, no close-in strong motion station exists that could be used to investigate this in detail.

3.8.1 "Y" structure in the north

An interesting feature of the Hector Mine earthquake model is the peculiar "Y" shape structure in the north. Is it possible to explain the observations using fault 2 alone without rupture on north portion of fault 1? In order to answer this question, we display the horizontal records of station HEC combined with the synthetic seismograms generated by the three separate fault segments shown in Figure 3.10.

The horizontal ground motion at the station HEC show very different characteristics in the N-S and E-W directions. The peak amplitude of the ground displacement along the N-S direction (47.8 cm) is three times larger than that along the E-W direction. And the waveform in the N-S direction shows more long period signal than in the E-W direction. While the radiation pattern can be used to explain the amplitude difference, it is difficult to match the different frequency content using a single source. Because the station HEC is near the nodal plane of fault 1 and N-S is near the radial direction, the large motion must be generated by the northwestern section (fault 2). This argument has been supported by the inverted slip distribution (Fig. 3.6). However, the high-frequency waveform in the E-W direction requires an additional source, i.e., if the slip also happens on fault 2, the amplitude on the N-S component will be larger than along the E-W compenent. Figure 3.6 indicates that the larger velocity motions in the E-W direction are generated by the middle section (fault 1) on which the motion starts early. The rupture time contours on fault 1 can be used to explain the high-frequency character in the E-W direction. During the first 2-4 sec of rupture, the rupture front propagates northward with a rupture velocity more than 2.5 km/sec. Moreover, the subfaults in the rupture region have very short rise times. These combined produce the large peak ground velocity at E-W component of the station HEC, which is the largest velocity recording during the Hector Mine earthquake. Hence we conclude that the "Y" rupture pattern in the north is favored by the observations.

Unfortunately, we can not find more evidence in the other seismic records. The seismic energy radiated from the subfaults north of the hypocenter was released in

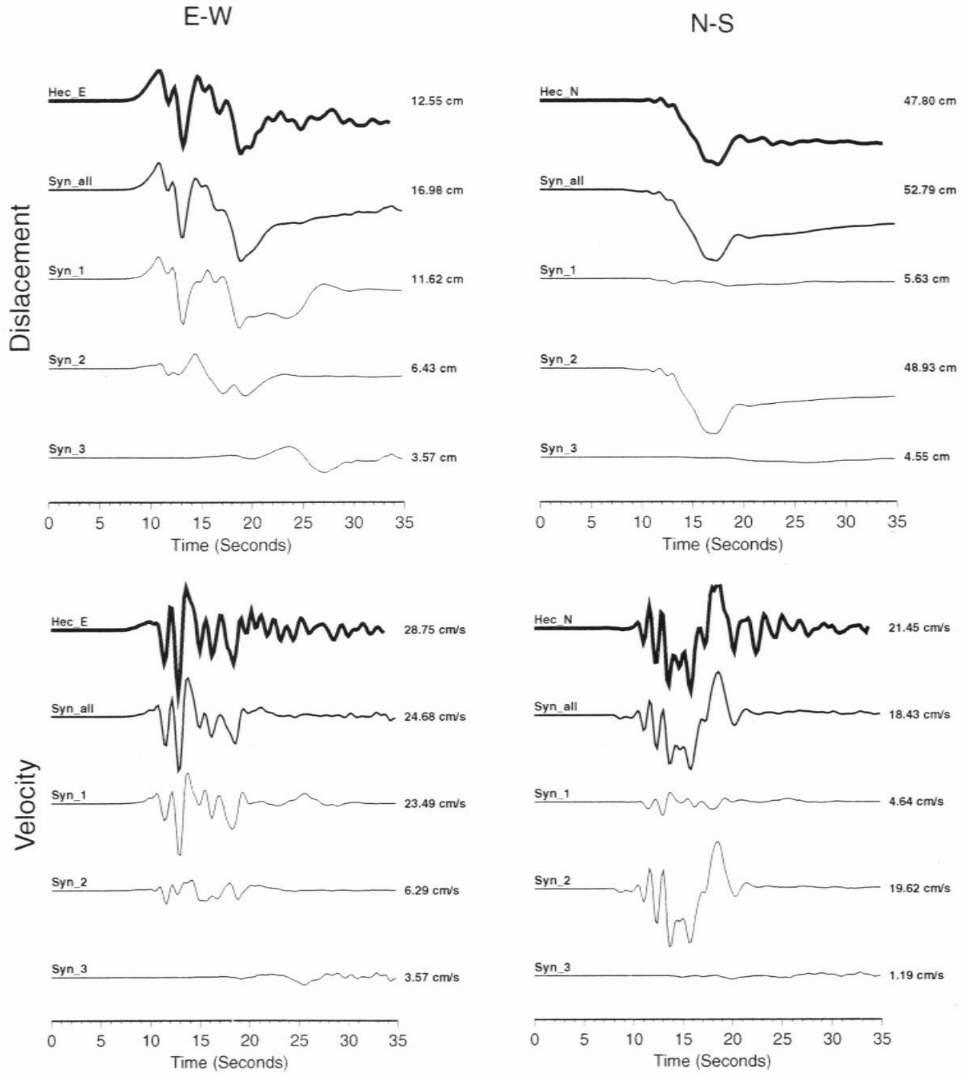

Figure 3.10: Contributions of the three fault branches at station HEC. We compare horizontal displacement, and velocity records with synthetic seismograms generated from the whole fault (Syn_all) and three separate fault branches (Syn_1, Syn_2, and Syn_3). The thick lines show the data.

the first 10 sec after initiation, which is also the time that two larger asperities on the faults 1 and 2 rupture. Hence, it is difficult to distinguish them uniquely in the more distant strong motion or teleseismic records.

The occurrence of the "Y" structure is not unprecedented in the Mojave events. The surface break of the 1992 Landers earthquake consisted of overlapped multiple faults. *Wald and Heaton* [1994] found significant slip on the overlapped fault segments in their finite fault inversion. However, without the special source station geometry we have here, it is quite difficult to distinguish whether the slip was concentrated on one of fault segments or both [*Cotton and Campillo*, 1995], and whether or not they ruptured simultaneously.

3.8.2 Comparison of the Hector Mine and Landers earthquakes

Since the 1992 Landers and 1999 Hector Mine earthquakes are so close in both space and time, it is natural to compare rupture models from these two events. Both earthquakes occurred in the ECSZ, and are nearly pure strike slip. Moreover, two events involved multiple fault planes, and slip started on the fault segments with a N15oW orientation, which may be explained with the block rotation and faulting model [*Nur et al.*, 1993] or crustal heterogeneity (Langenheim, personal comm., 2001).

The average rise time of the Hector Mine earthquake is also close to that of the Landers events. We calculate the weight average rise time of the Landers earthquake based on the slip model of *Wald and Heaton* [1994]. In that study, they used six 1-sec wide triangles to represent the derivative of the rise time function on each subfault. We define the rise time as the time required to accumulate from 10 to 90 percent of the total slip, and find the average rise times of the fault segments and entire fault range from 3.8 to 4.3 sec. This result is similar to the 3.6 sec average rise time we find for the Hector Mine earthquake.

However, the rupture propagation styles and speeds are notably different. The Landers earthquake ruptured unilaterally northward whereas the Hector Mine event ruptured bilaterally. Furthermore, there are significant differences in rupture velocities. Even though about 1 km/sec rupture velocity was reported in the overlapped parts of fault segments [*Wald and Heaton*, 1994], the average rupture velocity over entire Landers fault is 2.5-2.9 km/sec (e.g., *Wald and Heaton*, 1994; *Cohee and Beroza*, 1994; and *Dreger*, 1994), or 70- 80% of average shear wave velocity. This is similar to the average value obtained from other earthquakes [*Heaton*, 1990]. In contrast, the rupture velocity for the Hector Mine events is lower, averaging 1.9 km/sec. Dynamically, a slower rupture velocity implies that more energy is used to fracture rock [*Kanamori and Heaton*, 2000]. This may be explained by either a long slip-weakening distance or a high strength excess based on the slip weak hypothesis [*Guatteri and Spudich*, 2000], both of which suggest that the Lavic Lake fault should be stronger than the major faults involving in the Landers earthquake.

3.9 Conclusions

We have developed a model of the rupture history of the 1999 Hector Mine earthquake by the combined inversion of the strong motion, teleseismic and GPS data. The slip amplitude, rake angle, rise time and rupture velocity are recovered simultaneously. The wavelet transform approach allows time-frequency localization which allows for recovery of rupture timing and slip distribution. Our model has an average 1.9 km/sec rupture velocity, but the rupture velocity on the Bullion fault exceeds 2.1 km/sec.

Similar to other large earthquakes [*Ellsworth and Beroza*, 1995], the Hector Mine earthquake started with a foreshock or nucleation phase of 1.8 sec, and then the main rupture initiated deeper (12-15 km). The total slip duration (with the delayed origin time) was about 18 sec, close to the 22-24 sec duration of the 1992 Landers event. The total seismic moment was 6.28×10^{19} Nm. The rupture on fault 1 (eastern and central branch of the Lavic Lake fault) lasted 10 sec, and contributed over 41 percent seismic moment. Most energy is radiated by the asperity south of the hypocenter that had a long rise time. Rupture extended from the surface to over 12 km. Fault 2 (western branch of the Lavic Lake fault) was not triggered until about 3 sec later.

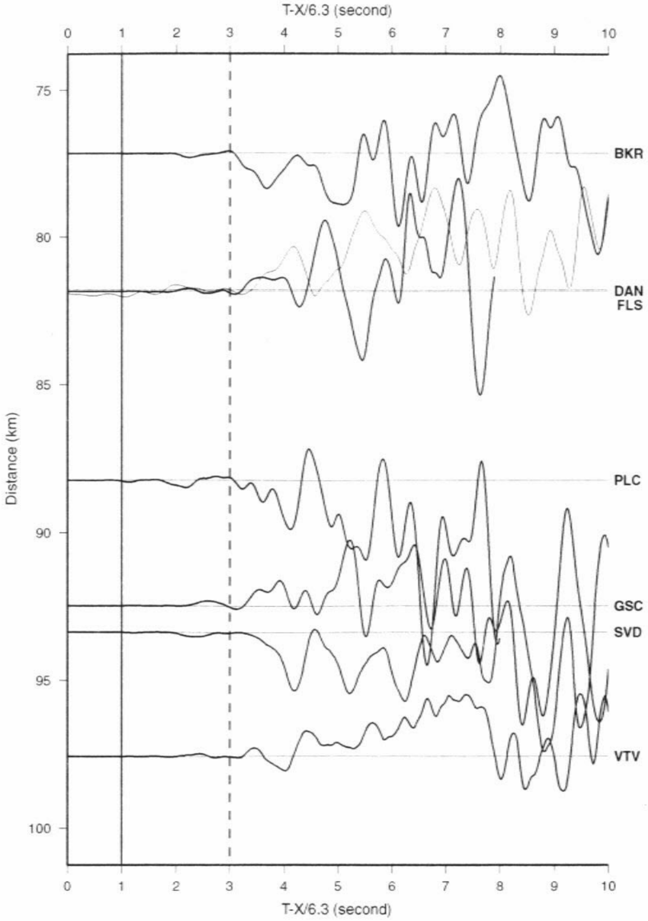

Figure 3.11: Beginning portions of vertical velocity records at several nearby stations for the Hector Mine mainshock. The data is low-pass filtered to 2 Hz. The traces were first reduced by a velocity of 6.3 km/s and then aligned to 1.0 sec. Note there is little energy in the first two seconds, followed by significant arrivals at all stations.

It then ruptured for 7 sec, releasing 37 percent of total seismic moment. Fault 3 (the Bullion fault) ruptured from 8 to 14 sec, and contributed the remaining 22 percent of the seismic moment. The slip on this segment was concentrated in the upper 9 km.

In the northern part of the fault system, we find evidence for a "Y" shaped rupture pattern where the two branches ruptured nearly simultaneously.

3.10 Appendix A

Ellsworth and Beroza [1995] summarized seismic evidence to indicate that beginning of the major slip during earthquakes is usually after a foreshock or a nucleation phase.

The records of the Hector Mine earthquake also displayed such a phenomenon. Figure 3.11 shows the vertical component of the velocity records at several of the closest stations to the earthquake. Note, in the first two seconds, there were very small amplitudes, then the larger signals arrived at nearly same time. In view of that the relative time-shifts of such larger signals in different stations were within 0.2 s, and the initiation of mainshock was within 2 km of the epicenter determined by *TriNet*. But, because all of those data are more than 75 km, we do not have a very good constraint on the hypocentral depth.

The records of closest station HEC set an upper-limit to the nucleation time (Fig. 3.12). Because the station is close to the P-wave nodal plane, we analyze the SH wave on the E-W component. Based on the Mojave model, the Sg wave should arrive at 8.3 s (T2 in Fig. 3.12), or 2.4 s before the observed Sg phase (T3 in Fig. 3.12). Hence, the nucleation time must be less than 2.4 sec. The difference in nucleation time estimated from Pg and Sg may be caused by inaccurate velocity structure, or deeper or southward initiation of the main rupture. However, if we use the network epicenter and the Mojave velocity structure, the depth of the rupture initiation should be around 14 km.

In this work, if we assume that the hypocentral depth is 12 - 15 km, then main rupture starts 1.8 s later after considering 0.2 s delay caused by deeper hypocenter.

3.11 Appendix B: Sensitivity to the crustal velocity structure

It was pointed out that velocity structure around the Hector Mine earthquake is relatively simple [*Hauksson*, 2000]. For the inversions presented, we choose the 1D Mojave model to build the Green's functions. However, this model is not perfect, and potential variations should exist compared to the real 3D earth. Such differences, in turn, should cause the uncertainty in the inverted finite fault model (Chapter 2). Here, we try to investigate this possible uncertainty by performing an inversion with

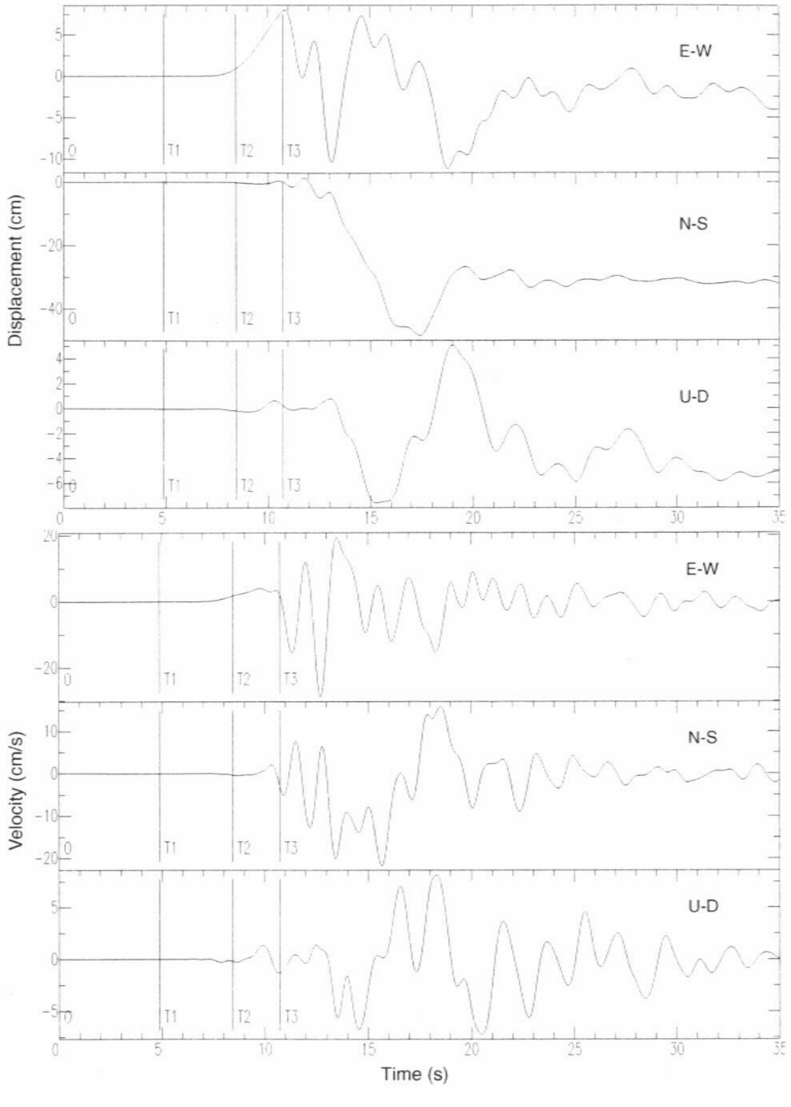

Figure 3.12: The three-component displacement and velocity records in station HEC. The data are low-pass filtered to 1 Hz. The time-mark T1 indicates the arrival time of P wave. Labels T2 and T3 are the predicted and observed Sg-wave arrival times, respectively.

a different velocity structure.

In Chapter 2, we discuss the effect of an inaccurate velocity structure with synthetic data. This showed that the inverted slip history changes can be significantly affected. Here, we use the southern California standard model (SoCal, see Fig 3.2; *Dreger and Helmberger*, 1993) to calculate the Green's functions and invert the fault model with exactly the same parameterization and data sets as those of our preferred model. Note that in contrast to the resolution test in Chapter 2, the surface offset data is used here. The result is shown in Figure 3.13.

In general, the variation in velocity model does not greatly reduce the fit to the data, but the inverted slip history is altered. The inversion to the slip distribution seems to be relatively robust. The overall patterns on fault 1 and 2 are quite similar to the preferred model, but the variation on fault 3 is large. The slip becomes deeper on fault 1 but shallower on fault 2. The largest effect of velocity structures is shown in the inverted rupture time distribution, particularly on fault 3. Even for fault 2, which is close to station HEC, we notice that the contours no longer vary smoothly as in our preferred model; one subfault slips earlier than the surrounding subfaults. Such phenomenon was also observed by the numerical tests in Chapter 2.

It is relatively difficult to evaluate the effect on the rise time distribution, simply because the small changes in slip distribution will bring the large variation in spatial distribution of the rise time. For instance, on fault 2, both models have a long rise time region (red region in Fig. 3.6 and Fig. 3.13), but this region in Figure 3.13 extends further southward accompanying a similar shift in the slip distribution. Hence, for rise time distribution, the relative pattern is more reliable than the absolute shape, which seems to be preserved.

These results reflect the fact that fault parameters have different sensitivities to the velocity structure. First, the slip distribution is robust because of the additional surface constraint. Second, if the rupture velocity does not change rapidly, the rise time of a subfault usually determines the frequency contents of radiating seismic waves. Unless shallower layers have much lower velocities, the frequency content of the dominant phase, S_g, is very robust with respect to velocity structures. Thus the

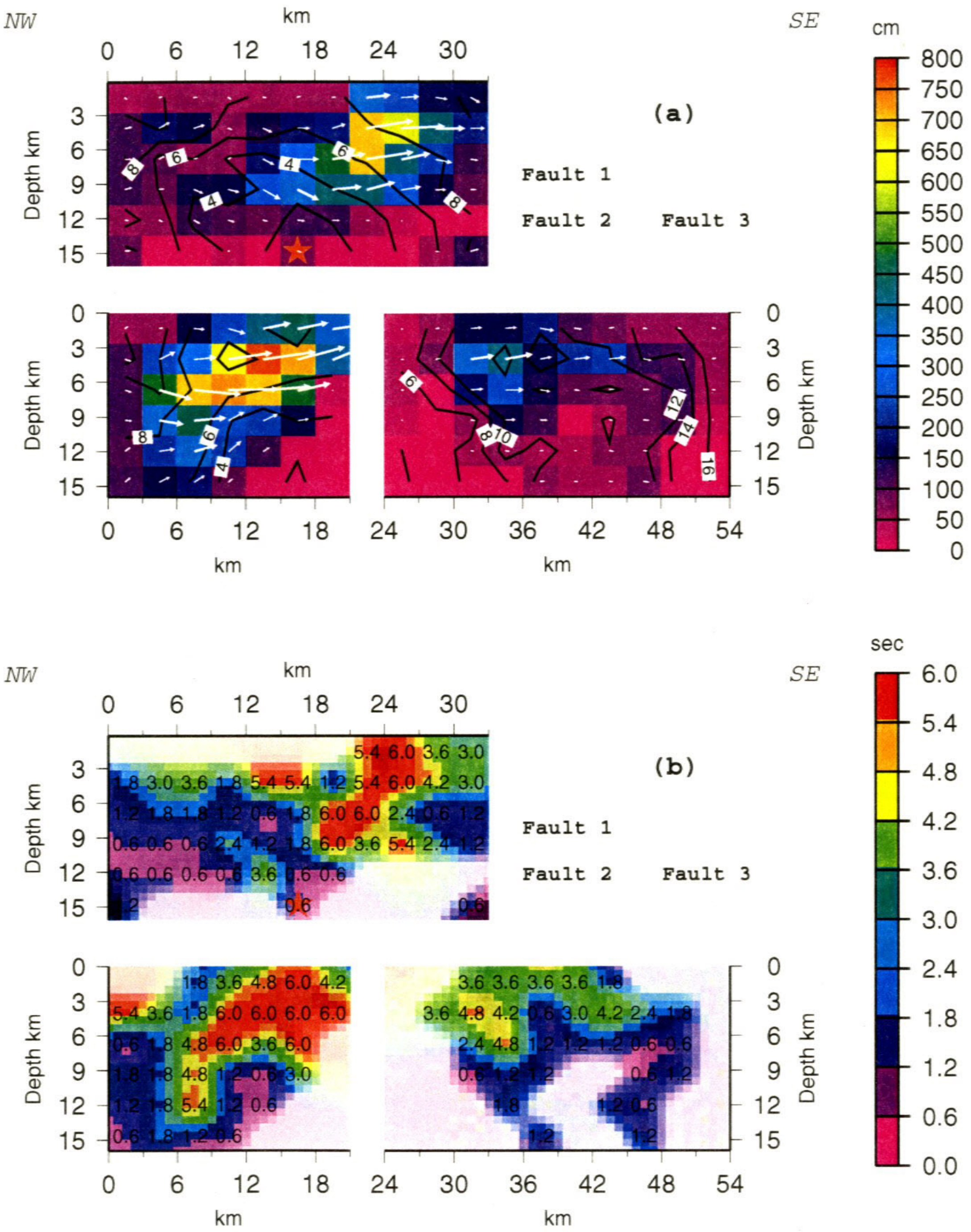

Figure 3.13: Cross section of the slip and rise time distributions determined from inverting combined strong motion, teleseismic waveform, GPS and mapped surface rupture data. The caption is same as for Figure 3.6. Note that in this inversion the Green's functions are generated from the SoCal velocity model (Fig. 3.2).

rise time distribution is fairly stable. Finally, the variation in velocity structure does affect when the phases reach the strong motion stations, so rupture velocities must change to compensate such effects. Even though the effect caused by the uncertainty of the Mojave model may be smaller than what we see here, the influence should definitely exist. Hence, when we analyze the results of our preferred model, the above possible variations should be taken into account.

Chapter 4 Fault geometry and slip distribution of the 1999 Chi-Chi, Taiwan, earthquake

4.1 Abstract

We report on the fault complexity of the large ($M_w = 7.6$) Chi-Chi earthquake obtained by inverting densely and well-distributed static measurements consisting of 119 GPS and 23 doubly integrated strong motion records. We show that the slip of the Chi-Chi earthquake was concentrated on the surface of a "wedge shaped" block. The inferred geometric complexity explains the difference between the strike of the fault plane determined by long period seismic data and surface break observations.

4.2 Introduction

Located at the "corner" of convergence between the Philippine Sea and Eurasian plates (Fig. 4.1), Taiwan results from the east-west (E-W) collision during the last 4 Ma [*Teng*, 1990]. Currently, southern Taiwan is still under intense collision due to the eastward subducting Eurasian plate underneath the Philippine Sea plate, but the tectonic style in northeast Taiwan reflects the northward subduction of the Philippine Sea plate beneath the Eurasian plate (e.g., *Teng et al.*, 2000). We expect that central Taiwan, where the 1999 Chi-Chi earthquake occurred, would contain a transfer zone where the convergence of subduction changes from E-W to N-S. The location of this transfer zone has not previously been resolved, presumably because of the complex surface geology in the Taiwan orogenic belt.

The Chi-Chi earthquake initiated at a depth of 10 km and ruptured the Chelungpu fault (CLPF) producing a 80 km long complex surface rupture pattern [*Kao and Chen*, 2000]. The fault surface offsets increase from south to north with 7 m of vertical and over 8 m horizontal offsets observed (e.g., *Lee et al.*, 2000). While the GPS data indicate the existence of large northward oblique motion on the northern part of the fault (Fig. 4.1), the surface trace does not continuously follow the mapped CLPF; instead, it turns to the east and extends another 15 km striking N80°E (Fig. 4.1). It is not obvious whether this extended piece of surface break is just a near-surface effect caused by slip on the CLPF, or corresponds to a large asperity on an unmapped fault. We address this question by modeling surface static displacement data following a finite fault approach [*Ji et al.*, 2002a] and try to constrain a reasonable fault geometry for the future study of the dynamic rupture.

4.3 Analysis

Observations in the vicinity of the surface rupture were selected and include 119 GPS displacements and 23 doubly-integrated strong motion accelerograms (Fig. 4.1, *Yu et al.*, 2001). Taken together, these data comprise one of the best static data sets yet recorded for finite analysis of a large earthquake. The inversions were performed on two finite fault model geometries. The first includes only one rectangular plane following the downdip extension of the portion of the CLPF that showed surface rupture. The second is composed of three planes that follow the strike of the three major segments of surface break (Fig. 4.1).

In contrast with the half-space earth model used in *Johnson et al.* [2001], here a more realistic layered earth model (Table 4.1, *Ma et al.*, 1996) is used to generated static response [*Xie and Yao*, 1989]. The apparent discrepancy between the vertical and horizontal observations noted by *Johnson et al.* [2001] can be explained by introducing a softer surface condition. For example, numerical tests presented in Figure 4.2 show that for a pure thrust fault with 30 degree dip angles, the response generated by a half-space earth model will be up to 10% smaller than that of the layered model in the hanging wall and over 30% larger in footwall.

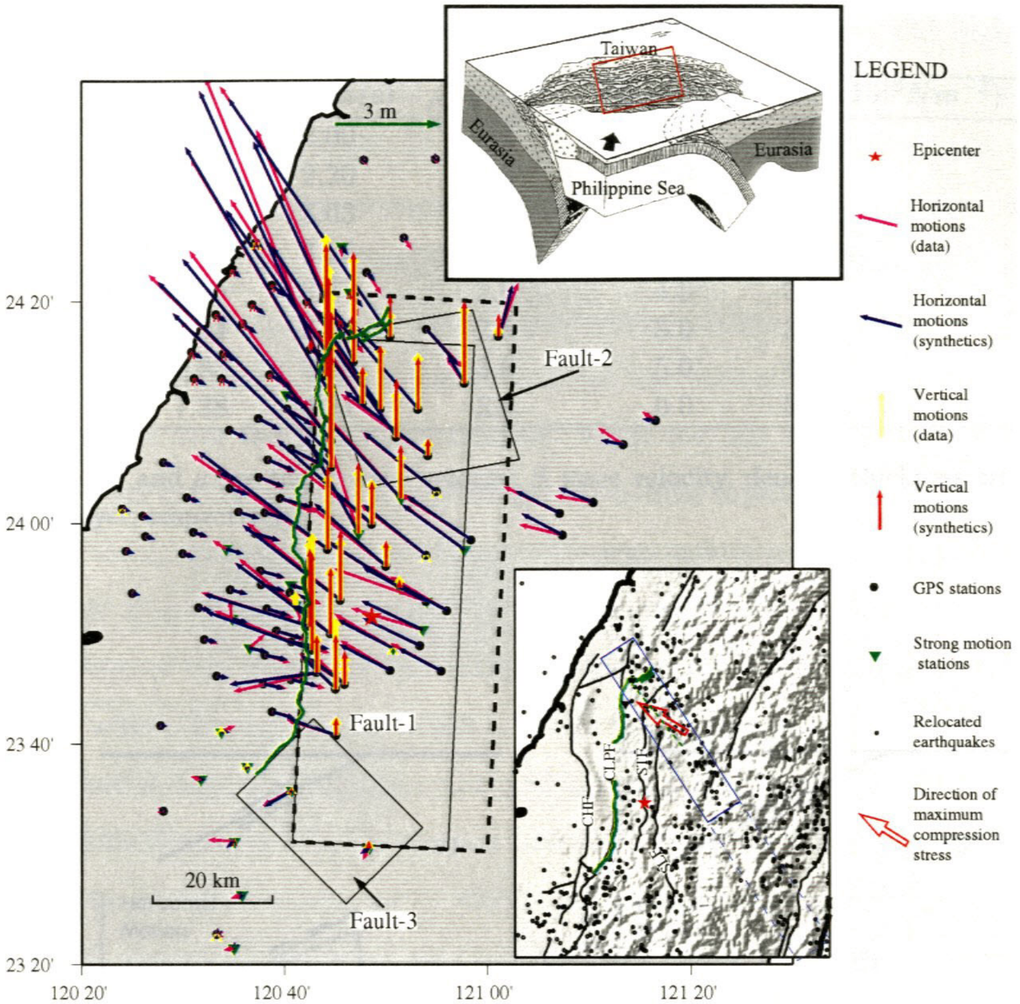

Figure 4.1: Upper-right inset shows the regional tectonic framework (Modified from *Angelier* [1986]); a red box is used to indicate the study region. The surface fault break is displayed as a heavy green line in the lower-inset along with topography map and the major faults (thin lines, CHF = Changhua fault; CLPF = Chelungpu fault; STF = Shuangtung fault; SLF = Shuli fault). The relocated small earthquakes during 1991-1993 [*Ma et al.*, 1996] are used to display the position of SanYi-Puli seismic zone (solid blue box). The trend of maximum compressional stress direction is 302±22° [*Hu et al.*, 1996]. Two fault models are displayed in the main figure. The first idealizes the entire event as a rectangle striking N3°E with a dimension (37 km by 95 km) (dashed line box). The second approximates the faulting with three faults: Fault-1 again striking N3°E, Fault-2 striking N80°E along the northern segment and Fault-3 striking N45°E along the southern segment. All fault segments dip 30° to the east. The synthetic displacements were generated from the second model.

Table 4.1: Central Taiwan crustal model

V_p (km/s)	V_s (km/s)	ρ (g/cm^3)	Thick (km)	μ $(\times 10^{10} Nm^{-2})$
3.50	2.00	2.0	1.0	0.8
3.78	2.20	2.3	3.0	1.1
5.04	3.03	2.5	5.0	2.3
5.71	3.26	2.6	4.0	2.8
6.05	3.47	2.6	4.0	3.1
6.44	3.72	2.6	8.0	3.6
6.83	3.99	3.0	5.0	4.8
7.28	4.21	3.0	0.0	5.3

V_p, V_s, ρ, th and μ are the P wave velocity, S wave velocity, density, thickness and rigidity of each layer, respectively.

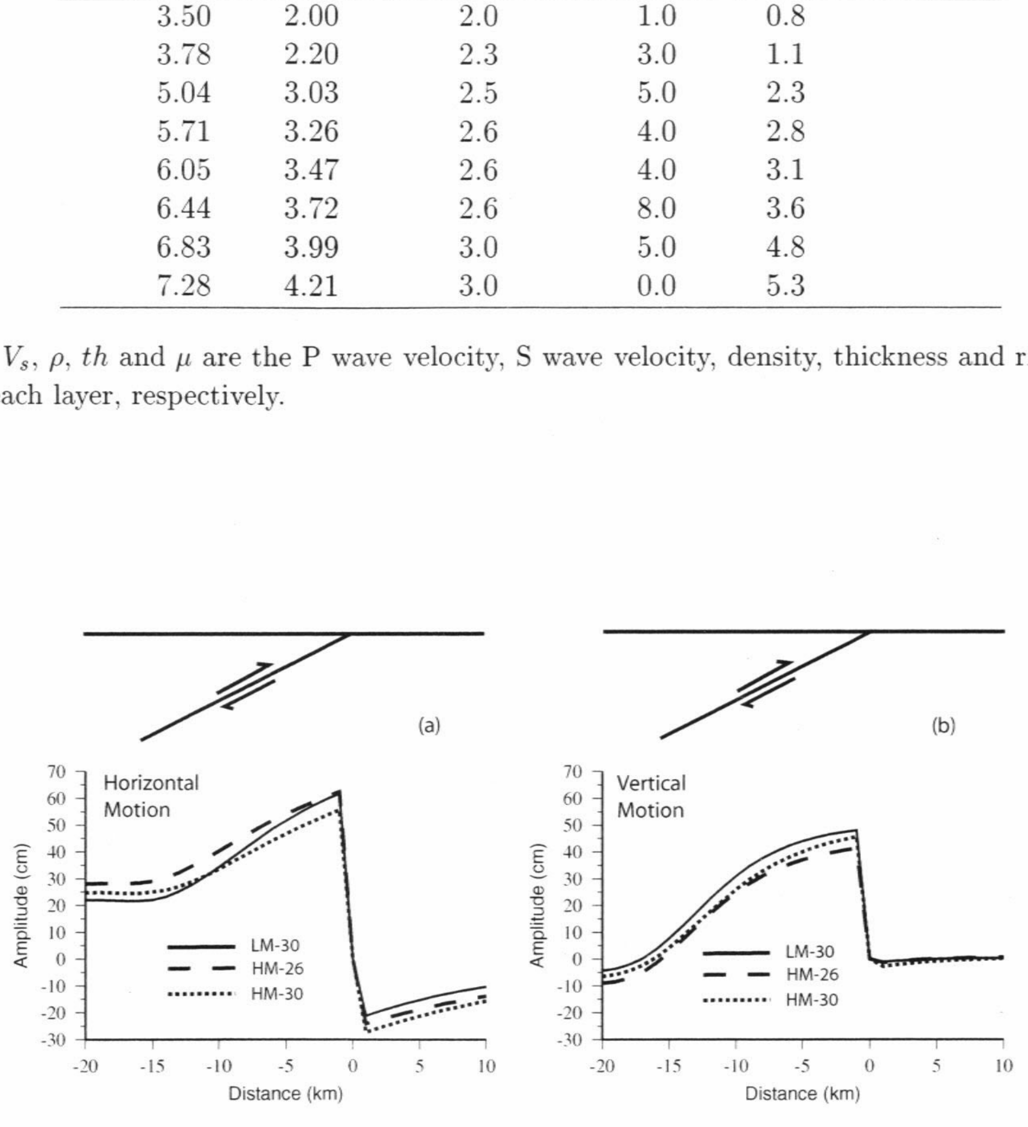

Figure 4.2: The surface displacements along a crosssection of a 2D thrust fault with 1 m uniform slip, 20 km fault width and 30° dip are plotted with (a) horizontal motion and (b) vertical motion. The solid and dot lines represent the response of the Central Taiwan earth model and a half space earth, respectively. Note that there are about 10% horizontal misfit for hanging wall and over 30% for footwall. While the horizontal motion of a half space earth can be increased if we use a smaller dip angle, say 26°, the vertical motion will be reduced (long dashed lines).

We employ a simulated annealing algorithm to find the global optimal solutions [*Ji et al.*, 2002a]. A series of inversions are performed to test the importance of fault dip-angles, essentially by grid searching all possible dip angles. For example, the error function is nearly constant when the fault dip of Fault-2 changes from 20° to 30°, but increases dramatically for other dip angles. Sizes of the fault planes were also examined to insure enough elements. Figure 4.3 displays the final inversion results for the two assumed faulting geometries. The inversions indicated that the single-plane model fits the data quite well, except at the two ends. With the optimum multi-plane model (Fig. 4.3a and 4.3b), we further reduced the total sum-squared error an order of magnitude over the single-plane model. Moreover, the slip pattern recovered by the optimum model suggests a very plausible physical rupture scenario. In Figure 2a, we plot the spatial distribution of the multi-plane solution. It appears that Fault-1 and Fault-2 cross each other and form the surfaces of a "wedge shaped" block. The intersection of two planes, or the margin (edge) of the block, extends from the free surface, where the fault break makes a nearly right angle turn, to the bottom of the planes, and is displayed in Figure 4.3b and 4.3c by a thick black line. Note that there is very little slip below this intersection boundary, while there are large displacements just above it. Such results are probably not an artifact produced by the inversion since our approach suppresses slip heterogeneity [*Ji et al.*, 2002a]. Thus, the slip appears to be confined entirely to the "wedge" which produced a massive uplift as displayed in Figure 4.5. Note that the sense of slip on the wedge surface is fully compatible with the maximum stress direction as indicated in Figure 4.1. Moreover, this direction is in agreement with the trend of the P (compression) axis derived from the multi-plane model (Table 4.2), and the aftershock fault plane solutions [*Kao and Chen*, 2000]. The fault geometry and slip distribution are consistent with the work of *Johnson et al.* [2001], even though entirely different forward and inverse approaches were used. The smaller optimal dip angles ($20 - 25^o$) they reported are probably due to the half-space earth model used. The slip distribution is also similar to that estimated by teleseismic inversions [*Ma et al.*, 2000].

The multi-plane model explains the apparent disparity between the Harvard Cen-

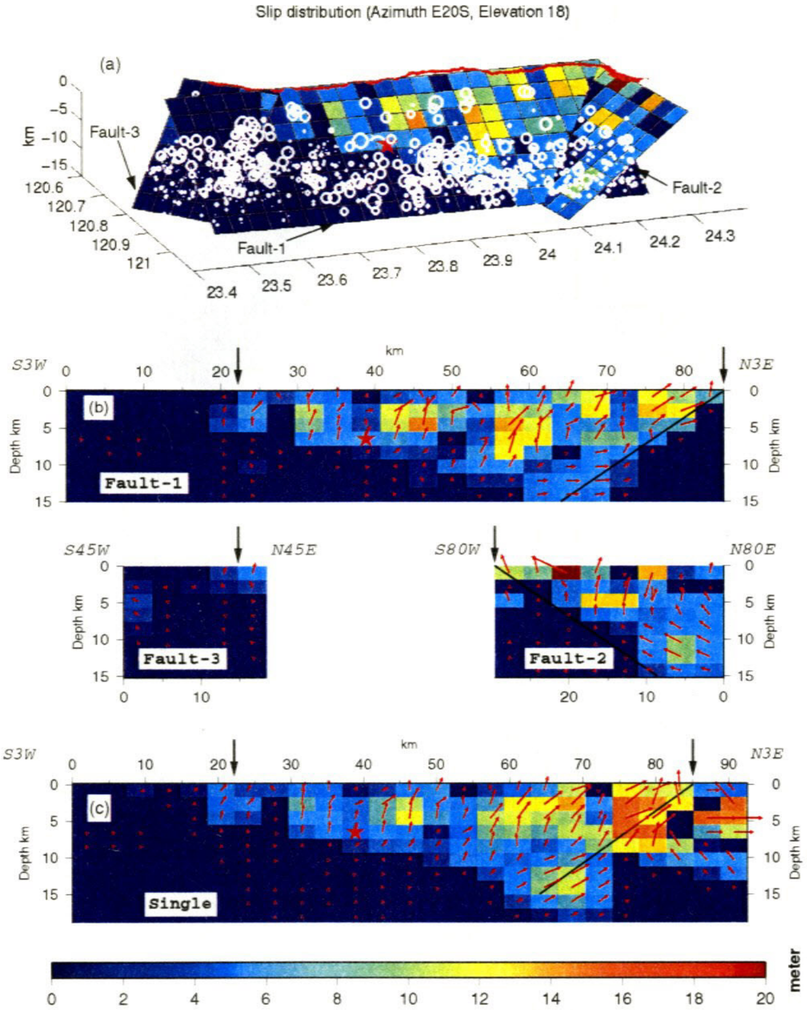

Figure 4.3: The top panel (a) displays the fault geometry for the multi-fault plane model with the main branch along the CLPF (Fault-1) and two secondary segments, Fault-2 and Fault-3. Plan views of these three faults are given in the second panel (b). The white circles show the aftershocks (Central Weather Bureau, Taiwan). The bottom panel (c) displays the results for a single-plane model. The color and arrows are used to indicate the slip amplitudes and directions. We have included a heavy dark line indicating the intersection points between Fault-1 and Fault-2. Note the absence of slip below this line in the multi-plane model and the rapid changes in the one-plane case in the vicinity of the boundary.

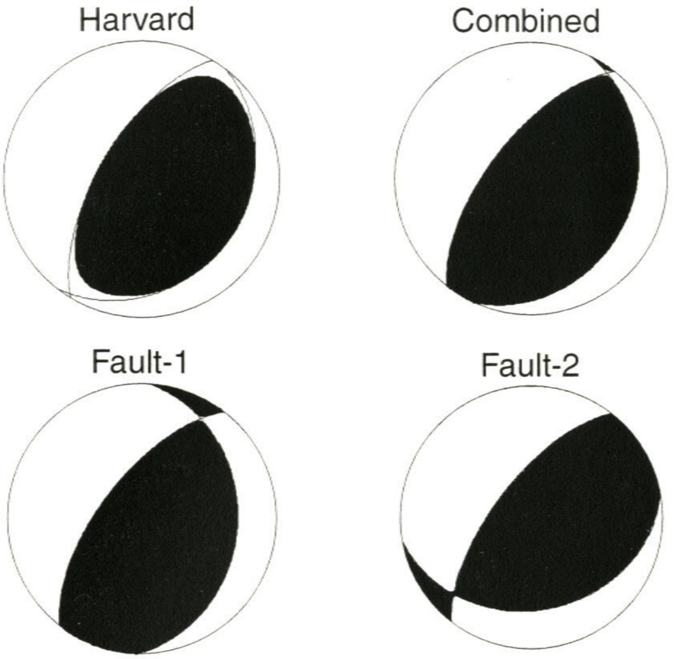

Figure 4.4: Focal mechanisms of Fault 1, 2 and whole faults are compared with the Harvard CMT solution.

troid Moment Tensor (CMT) solution and the CLPF orientation (see Table 4.2). Note the strike of Fault-1 differs by more than 30° from that derived from CMT. However, such a result is expected because the slip of the Chi-Chi event involved multiple fault planes. The CMT solution is primarily based on long period seismic waves with wavelengths over 300 km, hence the 80 km extent of this earthquake can be roughly approximated as a point source. The CMT solution, thus, reflected the vector summations of all contribution from the variable-geometry multi-fault segments. In Table 4.2, we show that the best double couple solution of the combined model is very close to the CMT solution. The corresponding focal mechanisms are shown in Figure 4.4.

Since our solution is mainly controlled by numerous GPS measurements, one might wonder if some of this slip occurred during the numerous large aftershocks [*Kao and Chen*, 2000]. We address this issue by computing the dynamic solution with our static models. For each point on the multi-fault plane, we define its rupture distance as the shortest on-fault-plane distance from the hypocenter, and its rupture initiation time is assumed to be the ratio of the rupture distance to the average rupture velocity along the shortest distance path. Then the seismic waveforms at

Table 4.2: Comparison of fault plane solutions

	Plane 1			Plane 2			P Axis	
	θ	δ	λ	θ	δ	λ	Az	Pl
Harvard	37	25	96	211	65	87	303	20
Combined	25	25	78	218	65	96	304	20
Fault-1	3	30	59	218	65	107	295	18
Fault-2	80	30	128	218	67	70	322	19
Single	3	30	57	220	65	107	297	18

θ, δ and λ are the strike, dip and rake angles, respectively. Az and Pl are the azimuth and plunge angles of P axis. The units of all values are degrees.

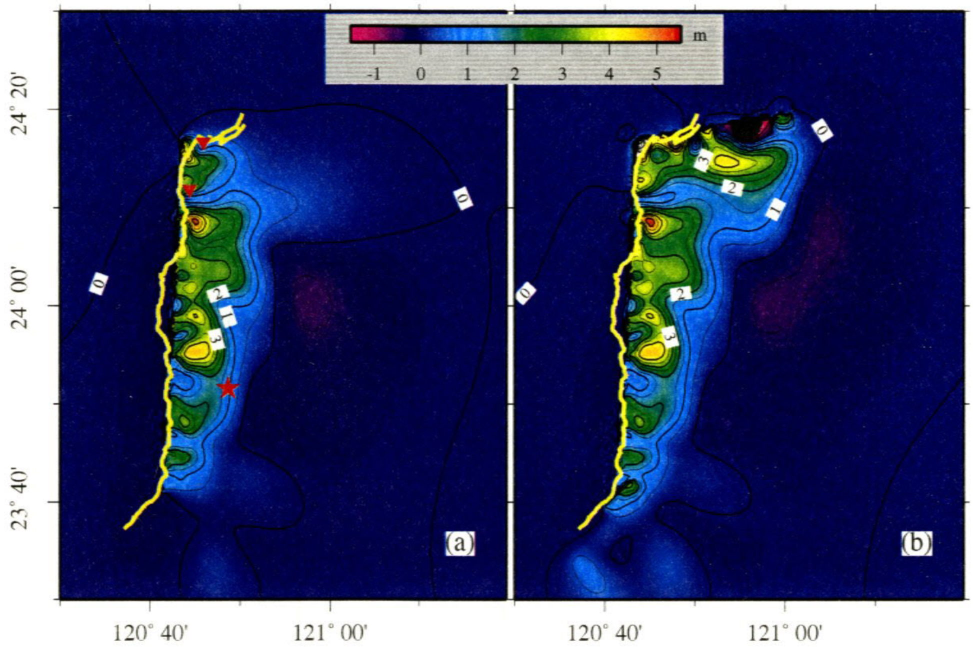

Figure 4.5: Uplift predictions at the surface produced by the multi-plane model with the contribution of Fault-1 on the left and the combined fault on the right. The motions are given in contours expressed in meters. The peak values reach about 5 m at the surface, and the total uplift volume is $2.4 \times 10^9 m^3$. Note that Fault-2 plays a major role in generating the static field at many northern stations. The triangles denoted two strong motion stations used in Fig. 4.6

two strong motion stations at the northern end (Fig. 4.5), where the largest GPS motions were observed, can be simulated very well with the multi-plane slip model and very simple assumptions of the rise time and the rupture velocity (Fig. 4.6). Note the displacement at T068 (the northern station) is dominated by the contribution of Fault-2, whereas the contribution of Fault-1 dominates the displacement of T052. While the single-plane model solution can explain the waveforms of station T052 equally well, it fails to model those at station T068, even though these stations are less than 10 km apart. Further research will be directed toward a combined inversion of seismic and geodetic data with the inverted fault geometry. That will help us to clarify this question.

4.4 Discussion

It appears that motions of two major fault planes of the Chi-Chi earthquake exhibit mechanical characteristics similar to the larger scale interaction between two plates. The CLPF and two adjacent faults to the east, the Shuang-Tung fault (STF) and the Shu-Li fault (SLF), formed by the east-west collision between the two plates [*Teng*, 1990], either turn to the east or are truncated by the east-west trending valley near their northern ends (Fig. 4.1, lower-inset). The surface projection of the hinge axis (green dashed line in Fig. 4.1) of the Chi-Chi earthquake rupture surface appears to connect the bending or truncation points of the two other faults. A linear seismic zone (the Sanyi-Puli seismic zone, lower-inset of Fig. 4.1) also follows the trend of the hinge axis and small earthquakes are concentrated on northeast side of the zone where the new faults, like Fault-2, are forming. Finally, the southeast extension of the Sanyi-Puli seismic zone meets with the coastal line at approximately 23.4^oN. This point roughly separates the coastal region into two domains. The geophysical observations in the southern domain indicate strong crustal shortening, deep seismicity and positive offshore free-air gravity anomalies, reflecting the existence of a deep subducted Eurasian slab. Observations in the northern domain show small component of crustal compression, shallow but strong seismicity and large negative offshore gravity

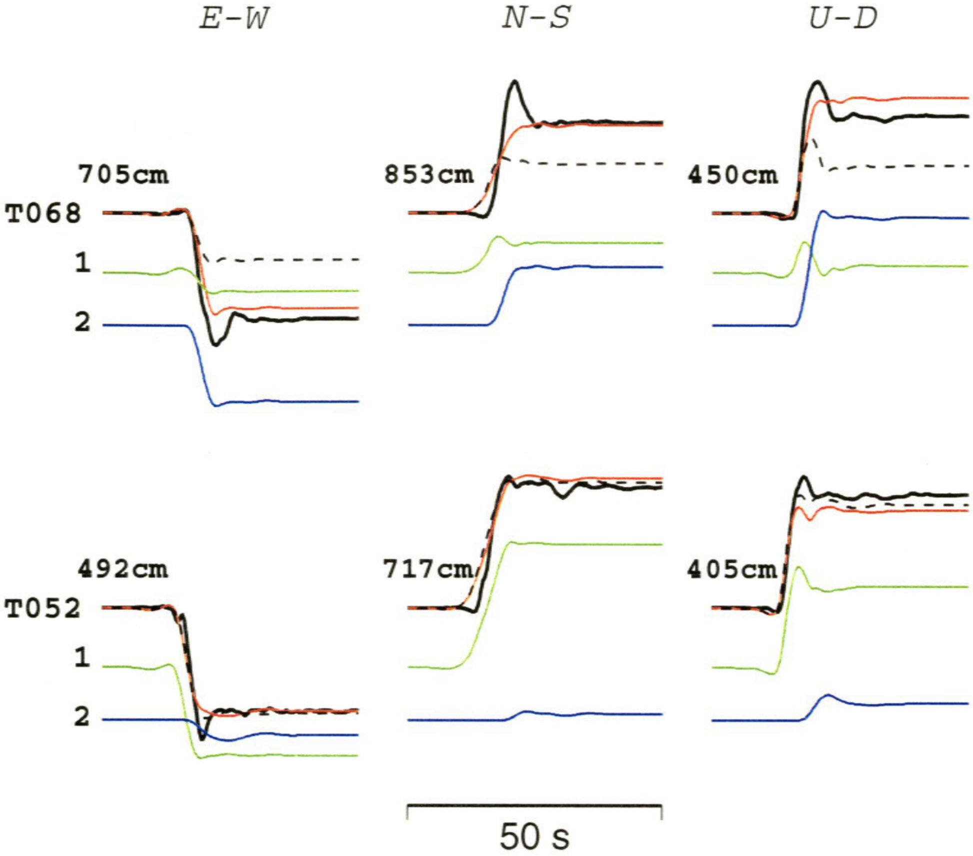

Figure 4.6: Comparison of observed strong motion displacements and synthetic seismograms at two stations, T052 (south) and T068 (north) as displayed in Figure 4.3. The black traces are data. The dashed traces were produced by the single-plane model and red by the combination of Fault-1 (green traces) and Fault-2 (blue traces). All the traces are aligned on the P-wave first arrivals and a rupture velocity of 1.9 km/sec is required to produce such alignment (assuming the velocity model in Table-1). We assume that all elements have the same rise-time function with a width of 7.5 sec.

anomalies, suggesting that in this region, the Philippine Sea plate has already started to subduct beneath the Eurasian plate (e.g., *Chemenda et al.* [1997]). Hence, the hinge in the "wedge" shape occurring in the Chi-Chi rupture surface may mark the present position of the transfer zone where the change in subduction polarity occurs.

The rupture pattern produced by this event involving old and new faults, similar to other recent studies (e.g., the 1992 Landers earthquake, *Nur et al.* [1993]; the 1999 Hector Mine earthquake, *Ji et al.* [2002b]), is related to evolutionary stress conditions and may provide unique information pertaining to the spatial and temporal patterns of tectonic processes.

Chapter 5 Slip history and dynamic implications of the 1999 Chi-Chi, Taiwan, earthquake

5.1 Abstract

We investigate the rupture process of the 1999 Taiwan earthquake, using high quality near source observations including three component velocity waveforms at 36 strong motion stations and 119 GPS measurements. A three-plane fault geometry derived from our previous inversion using only static data [*Ji et al.*, 2001] is applied. The slip amplitude, rake angle, rupture initiation time and rise time function are inverted simultaneously with a recent developed finite fault inverse method that combines a wavelet transform approach with a simulated annealing algorithm [*Ji et al.*, 2002a]. The inversion results are validated by the prediction of an independent data set, the teleseismic P and SH ground velocities, with notable agreement. The results show that most of slip occurred in a triangular-shaped asperity involving two fault segments, which is consistent with our previous static inversion. The total seismic moment from this inversion is 2.7×10^{20} Nm, in agreement with the Harvard moment estimation. The rupture front propagates with an average rupture velocity of about 2.0 km/sec and the average slip duration (rise time) is 7.2 sec. Three interesting observations related to the temporal evolution of the Chi-Chi earthquake are also investigated, which include: (1) The sinuous fault plane of the Chelungpu fault strongly affects both spatial and temporal variation in slip history, (2) Long-period peak slip velocity increases as the rupture propagates, and (3) the peak slip velocity near the surface is in general higher than on the deeper portion of the fault plane as predicted by dynamic modeling (e.g., *Oglesby et al.*, 1998).

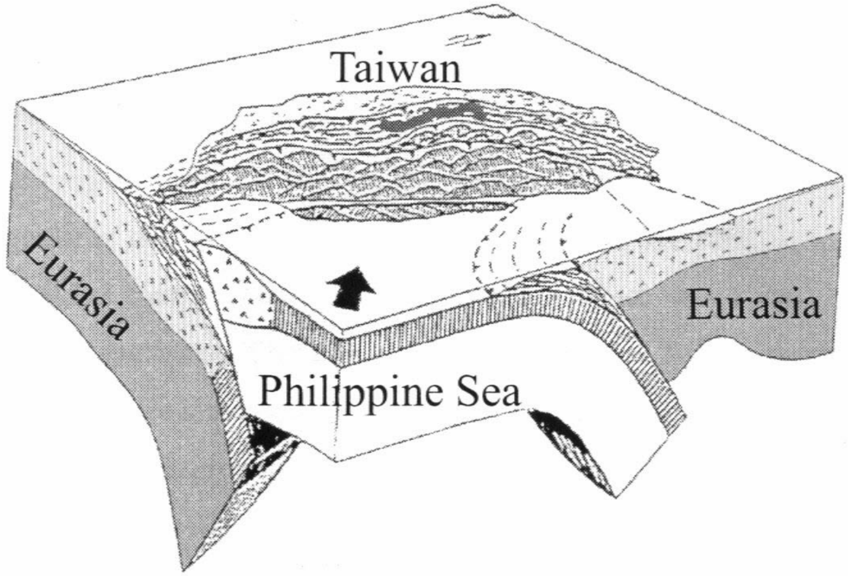

Figure 5.1: Tectonic background of the Taiwan region (modified from *Angelier et al.* [1986]) showing the complex plate-interaction involving the uplift of Taiwan. The surface rupture trace of 1999 Chi-Chi earthquake is indicated by the heavy line.

5.2 Introduction

In recent years, geologists and geophysicists have witnessed a revolution in the development and implementation of an array of new tools for measuring motions of the earth's crust, including global positioning satellites, interferometric synthetic aperture radar, and broadband digital seismic systems, allowing tremendous advances in motion detection accuracy. Japan and Taiwan took the lead in the installation of these instruments and the recent Chi-Chi Taiwan earthquake (1999) sequence produced a remarkable set of data. About 150 GPS static measurements and 200 strong-motion acceleration records at distances less than 50 km are now available for the main event, MW = 7.6 [*Lee et al.*, 1999; *Yu et al.*, 2001]. Such a "lifetime" data set offers a unique opportunity to understand the earthquake process and the generation of strong ground motions. In particular, we can rely on the GPS data to investigate the fault complexity and static dislocation field, and use the strong motion data to constrain the temporal evolution of the rupture involved in producing these offsets.

The Chi-Chi earthquake occurred in the collision zone of Eurasia plate and Philippine Sea plate, where the Philippine sea plate moves with a speed of 7-8 cm/yr. in the N305E direction relative to the Eurasian plate (Fig. 5.1) [*Seno et al.*, 1993; *Yu et al.*, 1997]. Such fast relative motion uplifts Taiwan and is presumably the tectonic cause of the large earthquakes visiting the island and adjacent regions. The 1999 Chi-Chi earthquake is the largest inland event occurring in the 20th century. The event created a 100 km long surface trace, and most of which was along a known active fault, the north-south trending Chelungpu fault (Fig. 5.2) [*Lee et al.*, 2000a]. The surface slip amplitude increased from south to north and reached a peak of nearly 10 meters where the peak ground velocity was about 4 m/sec the largest ever recorded. However, the peak accelerations were recorded in the middle and southern sections of the fault, and there were only relatively modest values associated with the largest surface breakage. *Ma et al.* [2000] suggested that this behavior is correlated with the variation in rupture velocity, where the initial rupture started at 2.5 km/sec, increased to 4.0 km/sec, and then decreased to 1.2 km/sec in the region of largest slip. Their study assumed rupture on a rectangular fault plane to model the strong motions and explained most of the complexity of the recordings in terms of localized asperities with large slip offsets. A similar result was obtained by Chi et al. [2001], where the many local strong motions recording were well matched. However, the geodetic data (GPS) require a more complex rupture process involving multiple fault planes as in analysis of the 1992 Landers [*Wald and Heaton*, 1994] and 1999 Hector Mine [*Ji et al.*, 2002b] earthquakes. In particular, after the right-angle turn near the northern end of the fault, the surface break actually extends about 12 km to the east (Fig. 5.1) and requires significant moment release along this portion according to analysis by *Johnson et al.* [2001]. They model this fault bending by introducing 3 planes and inverting the GPS data (static field) assuming a half-space crustal model. *Ji et al.* [2001] found that the modeling error could be greatly reduced by assuming a more realistic, layered crust (see Table 5.1) and approximating this geometry with two rectangular fault planes as displayed in Figure 5.2. The motions on these planes produced a "wedge" shape up-lifted block near the northern end as discussed in [*Ji et al.*, 2001]. Here we investigate the kinematic rupture history of the Chi-Chi earthquake with this new fault geometry and analysis of the waveform data as a continuation of our previous static study referred to as Chapter 4.

The joint inversion of both the static and dynamic data requires considerable care and attention to the faulting geometry, primarily due to the unprecedented abundance of near-source data. For such a complex inverse problem we apply a new set of inversion tools developed by *Ji et al.* [2002a]. By combining a wavelet transform approach with a simulated annealing algorithm, we demonstrate that our inversion results are robust enough to independently predict the teleseismic waveforms to a high degree of accuracy.

5.3 Data

We used 119 3-component GPS measurements from the dataset collected by the Institute of Earth Sciences, Academia Sinica [*Yu et al.*, 2001] for static constraints as discussed in the Chapter 4. *Yu et al.* [2001] noted that the afterslip in the first few days following the mainshock is included in the final estimates of co-seismic displacements in some epoch-surveyed stations. However, he estimated that the effect is quite small for most stations (less than 5%). Presumably, the static recovered from the waveform data can be used to constrain the fault model. We will address the issue of afterslip later.

Waveforms recorded at 36 strong motion stations (Fig. 5.2) are used in the inversions. This data set was subdivided into three groups. Group 1 includes the 11 stations that are directly above the assumed fault plane discussed later (open triangles). Group 2 is composed of 13 stations (solid triangles), which are located on the western side of the Chelungpu fault (footwall side). Even though all of these are within 20 km of the surface break (thick trace), most of these stations are located on the foreland sedimentary basin (e.g., *Kao and Chen*, 2000). The last group includes 12 stations (squares) that form a rather uniform array covering the rest of fault plane.

Because of a Y2K problem, some of the strong motion stations did not have the correct trigger times [*Huang*, 2001]. Fortunately, the first arrival of each record can

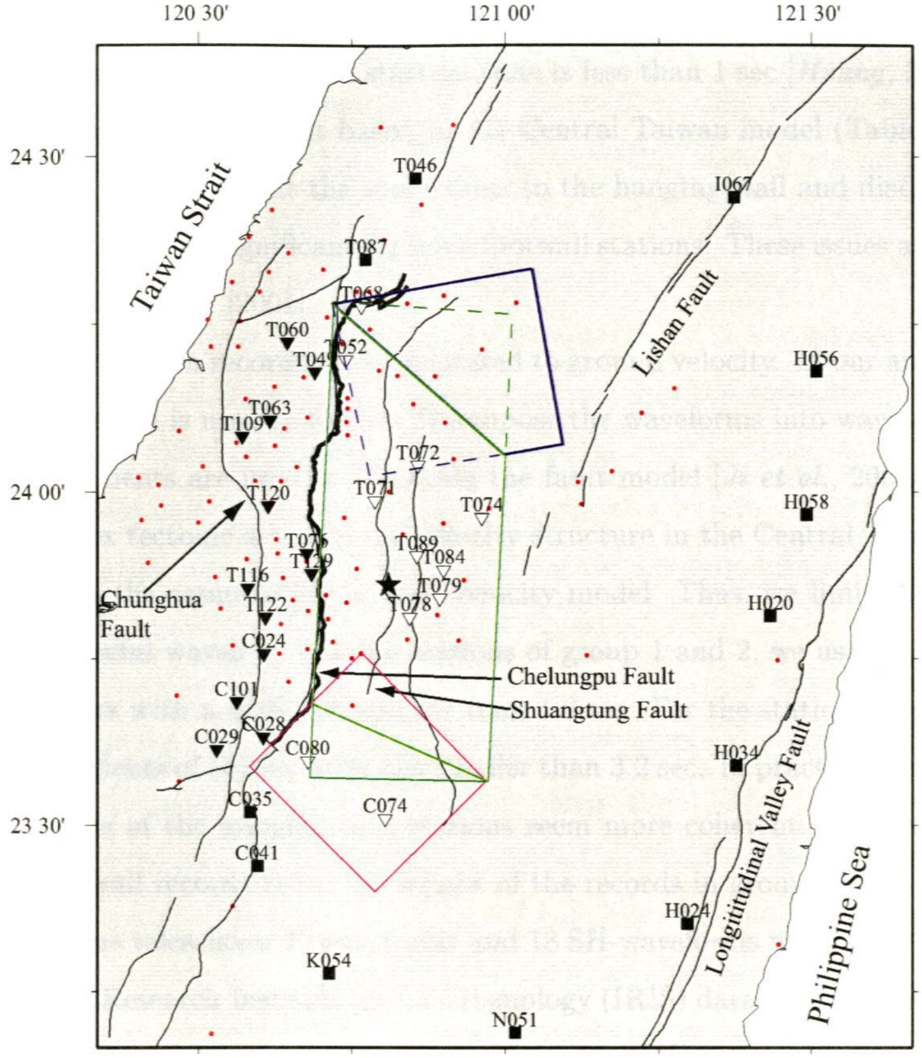

Figure 5.2: Fault geometry of the Chi-Chi earthquake with GPS station displayed as red dots and strong motion stations as squares and triangles. Symbols of strong motion stations are discussed in the text. A star is used to represent the epicenter. The surface break of 1999 Chi-Chi earthquake is plotted with thick lines; other major faults are shown as thin lines. The map projection of preferred fault geometry is displayed by three boxes with green for Fault-1, blue for Fault-2 and pink for Fault-3. Note that the GPS stations have much better coverage in the northeastern portion of the rupture.

be picked easily because the records include a 20 sec pre-event memory and the first arrival are impulsive for this thrust event. *Huang* [2001] suggested a possible way to correct for timing. He first picked the arrival time of each record, and then aligned it with the synthetic first arrival calculated with the 1D layered Taiwan model. After such processing, the error in the starting time is less than 1 sec [*Huang*, 2001]. Here, we use a similar approach but based on 1D Central Taiwan model (Table 5.1, Ma et al., 1996). It turns out that the corrections to the hanging wall and distant stations are small, but become significant for some footwall stations. These issues are discussed at length in *Chi et al.* [2001].

All strong motion records were integrated to ground velocity. In our approach, the wavelet transform is used to further decompose the waveforms into wavelets, and the wavelet coefficients are used to constrain the fault model [*Ji et al.*, 2002a]. Because of the complex tectonic activity, the velocity structure in the Central Taiwan is more complex than the assumed 1D layered velocity model. Thus, we limit the frequency contents of useful wavelets. For the stations of group 1 and 2, we use the coefficients of the wavelets with a scale not smaller than 1.6 sec. For the stations of group 3, we use the coefficients of the wavelets not smaller than 3.2 sec. In practice, we notice that the waveforms of the hanging wall stations seem more coherent. Thus we assigned the hanging wall records twice the weight of the records in groups 2 and 3.

Twenty-one teleseismic P-waveforms and 18 SH-waveforms were selected from the Incorporated Research Institutions for Seismology (IRIS) data center, which provided good azimuthal teleseismic coverage of the source. We removed their instrument responses and then converted them to ground velocity. This far-field data set is not used directly to constrain the model; instead, we use them later to verify the preferred model constrained by local observations, i.e., the GPS measurements and strong motion waveforms.

5.4 Fault geometry and method

The fault geometry determined by our previous static study (Chapter 4) is displayed in Figure 5.2. Three fault segments are used to represent the fault rupture during the Chi-Chi mainshock. Fault 1 is along the north-south trending Chelungpu fault and has a strike of N3°E. Fault 2 follows the east-trending surface rupture at the northern end of the rupture and has a strike of N80^{o}E. Fault 3 was added to match the bend in the surface break at the southern end and has a strike of N45^{o}E. All fault segments have a dip angle of 30^o as discussed in Chapter 4. Finally, we extend the three fault segments from the surface to a depth of 17 km; preliminary models extending below this depth demonstrated that this depth is adequate. We divide the fault plane into small rectangular regions of equal area, or subfaults. The response of each subfault can be represented as the function of its slip amplitude, rake angle, rise-time function and rupture velocity. Thus the motions (displacements) can be generated as summation of all subfaults by equation (2.1).

Note that each subfault Green's function is represented as summation of 81 point sources to take the directivity inside a subfault into account, which is very important in modeling the hanging wall stations where single point source representation for a subfault is inadequate. In this study, we divide the 3 fault planes into a total of 360 subfaults each with dimensions of 3.8 by 3.7 km. However, not all subfaults are used to generate the synthetic response. In Chapter 4, we confirmed a physically plausible assumption that slip was limited to the surface of a "wedge" shape block, and not on subfaults below the intersection of the planes in the north and south (see Fig. 5.2). So for the subfaults below the wedge surface, we set the slip amplitudes to zero to restrict the number of parameters. Preliminary checks of this assumption proved accurate in that these elements generated negligible motions. This constraint limited the number of contributing subfaults to 324.

In this work, we used an asymmetric cosine function (equation 2.3) to represent the time function. With this approach, the derivative rise function is determined by just two parameters, i.e., starting-phase time t_s, and the end-phase time t_e (Fig. 2.1).

This approach permitted us to model the asymmetric "pulse" like ground velocity that are clearly displayed by observations near the surface break. Even though this approach has one more degree of freedom than the symmetric cosine function used in our previous study of hector mine earthquake [*Ji et al.*, 2002a], it is still far fewer than the multiple time window approach [*Ma et al.*, 2001; *Chi et al.*, 2001]. Because of this simple parameterization, our inversion only intends to investigate the first order slip characteristics of rupture. The real slip process may be more complex, and simple parameterization will cause the misfit of strong motion waveforms to some extent. However, we will show that such a simple representation in fact can give a very good waveform fit for most of the strong motion waveforms and predicts the teleseismic waveforms quite accurately.

For all fault segments, we allow the slip amplitude of each subfault to vary from 0 to 24 meters. On fault 1 and 3, the rake angle are fixed in a range from 0 to 180 degrees; in other word, we do not allow downward slip. On fault 2, we let the rake angle vary from 0 to 360 degrees because there are surface observations of normal faulting. We let the average rupture velocity vary from 1.5 km/sec to 3.0 km/sec. The simulated annealing method [Sen and Stoffa, 1991] is applied to find a global minimum of an error function defined by equation (2.15). A balance of fitting to the strong motion, GPS and smoothness of model is controlled by weights W_{st} and W_c, which is determined by trial and error.

5.5 Modeling the data

The seismic data proves much more difficult to model relative to the static data because of its sensitivity to crustal structure and its intrinsic complex nature. That is the near field and far-field contributions from several subfaults interfere with each other to produce patterns that are controlled by both the spatial and temporal slip functions. We have attempted to reduce this interference by choosing a relatively simple time history with the two-parameter approach. Many inversions with differing combinations of weighting Wst and Wc were attempted to achieve compatible fits to both the static and strong motion and we adopted $W_{st} = 1$ and $W_c = 0.1$. The preferred model constrained by the static and strong motion data is displayed in Figure 5.3. The total moment release is 2.7×10^{20} Nm with the rigidity converted from the 1D Central Taiwan model (Table 5.1). The slip distribution is close to the result of the static inversion (Chapter 4) with relatively small offsets near the hypocenter and a large triangular shaped asperity with an apex at a depth of about 15 km. This result is similar to other models based on seismic data alone too [e.g., *Ma et al.*, 2000; *Chi et al.*, 2001]. However, the asperity in our model involves both Fault-1 (Chelungpu fault) and Fault-2. In fact, the subfault with maximum slip (20 m) is located on Fault-2, where the surface break bifurcates and two branches separate by about one km. The slip there is not always pure thrust, and in fact, there is a small piece of Fault-2 displaying downward motion to fit one of the GPS measurements. However, this motion could also be caused by some associated slip on the ShuangTung fault [K. Sieh, personal comm.] or by some other complexity in the fault geometry not addressed here.

The comparison of synthetic static displacements and GPS measurements is displayed in Figure 5.4. In general, the new model can explain the GPS observations nearly as well as the model constrained by the geodetic data alone (Chapter 4). However, some local discrepancies are apparent, particularly in the region around the hypocenter, which is probably due to the afterslip as suggested by *Yu et al.* [2001]. Another region showing misfit is at the eastern end of surface break (Figure 5.4). Both data and results of Chapter 4 show small vertical motion, but not in the model of the combined inversion. This reflects the conflict between static and strong motion data near the northern portion of the fault, and is probably caused by our simplified fault plane which only approximates the complexity of the fault trace. This feature will be further addressed in a future effort, involving smaller subfaults and more complex fault plane geometries.

The fits to the waveform data are displayed in Figure 5.5. In order to be compatible with the information used in the inverted fits, we low-pass filtered the data and synthetics before the comparison. For hanging wall and footwall stations (group 1

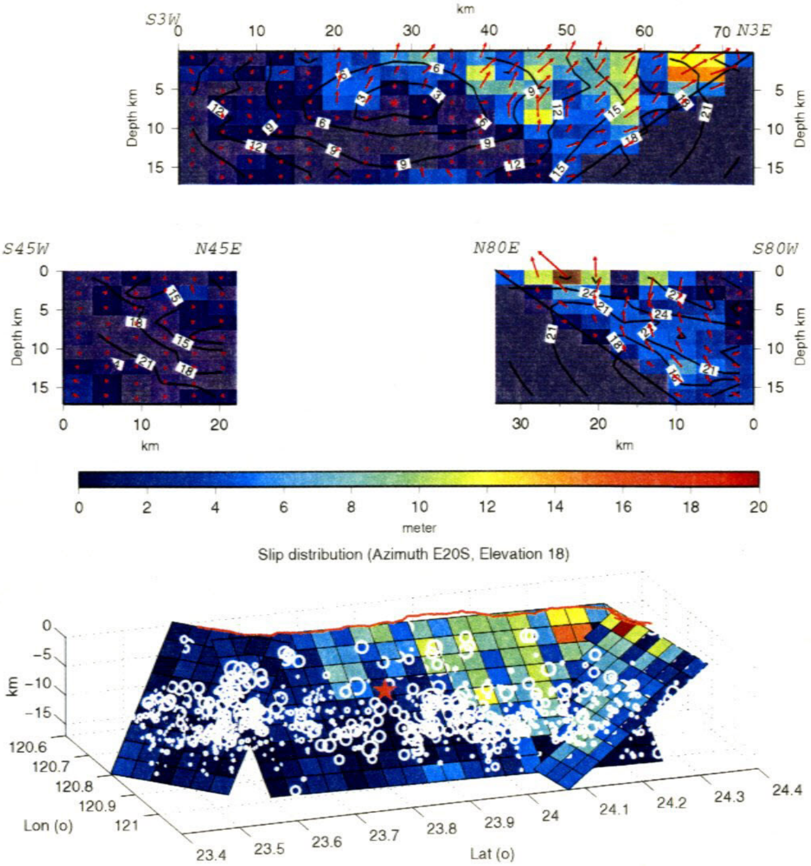

Figure 5.3: 2D and 3D views of slip distribution of the preferred combined model. Upper panel displays the slip distribution in planar view. Fault-1 is on the top, and Fault-2 and Fault-3 are on the low-right and low-left portions, respectively (Fig. 5.2). Color indicates the magnitude of slip, arrows represent the slip directions and contours show the rupture initiation time with 3 sec intervals. A red star displays the location of the hypocenter. A black line indicates the intersection of the Fault-1 and Fault-2. The lower panel displays 3D view of the same slip distribution. The color represents the slip in each subfault with same color bar (upper panel).

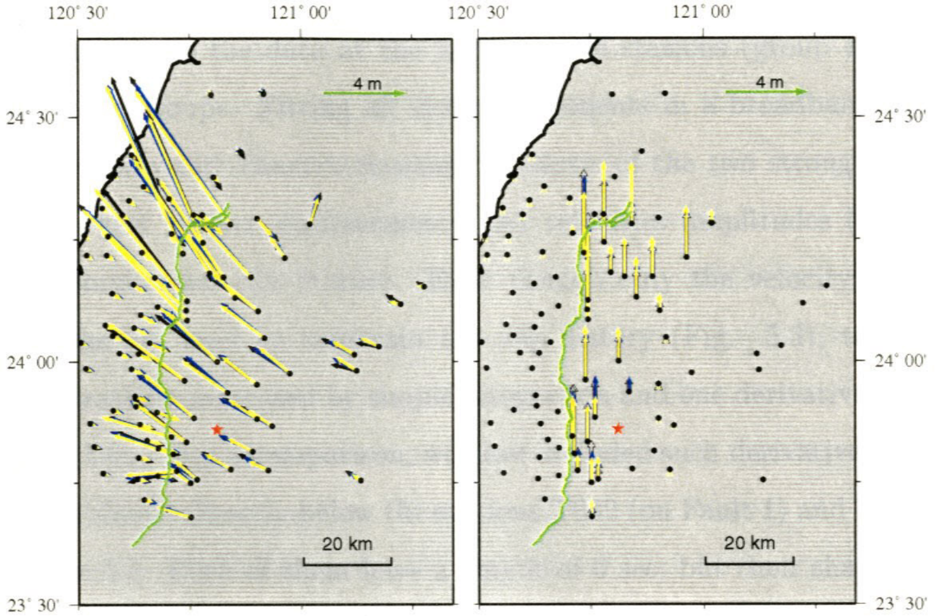

Figure 5.4: Comparison of GPS observations and synthetic static displacements with the horizontal motions shown in the left and vertical motions in the right. The GPS data is shown in black, and nearly overlaps by the synthetic displacements (in blue) generated by the slip distribution of static only inversion (Chapter 4). The synthetic displacements generated by the preferred, combined model are plotted with yellow arrows. The surface breaks are plotted with green lines.

and 2), a low-pass filter with a corner frequency of 0.8 Hz was chosen, which is the highest frequency content in the smallest scale wavelet used, i.e., scale s =1.6 s. For the distant records (group 3), the corner frequency is 0.4 Hz. The inverted model can explain the hanging wall and distant records very well, but it does not reproduce all of the details of the footwall records (group 2, Fig. 5.5b). This is mainly due to the fact that the simple 1D velocity model used is not sufficient for modeling the complex 3D sedimentary basin structures in the west of the Chelungpu fault [e.g., *Kao and Chen*].

The fits to the data at the hanging wall stations (group 1) are the best among the three groups. Fitting all three components in a broadband sense is largely due to the "wavelet" characterization. Analysis of the two strong motion stations with the largest ground displacements and velocities amplitudes (T052 and T068, Fig. 5.6) emphasizes this feature. Even though only the velocity records at those two stations are used to constrain the slip history (Fig. 5.3), the displacements and accelerations generated by simple integration and one derivative fit the data very well (Fig. 5.6a). For a comparison, we have included such derivative rise time functions of the subfaults directly below the stations T052 (on Fault 1) and T068 (on Fault 2) into Figure 5.6. Both of them have a length of 6 sec, but their shapes are different. The subfault beneath station T052 has a symmetric derivative rise time function, while that beneath station T068 has a much shorter starting time (t_s). It is noteworthy that the derivative rise time functions of these two subfaults are very similar to the shapes of the vertical velocity records at the stations right above, but are simpler and narrower than the horizontal records. Such phenomena can be explained intuitively by the different radiation pattern of P-SV wave and SH waves, i.e., when a hanging wall station near the surface break, it is close to the nodal plane of both far-field P and SV radiation generated by the slip on the distant subfaults. However, the far-field SH wave radiation has the maximum amplitude. Simply because the SH wave only influences the horizontal motion, the horizontal components are influenced more by the distant subfaults than the vertical component. Thus, the hanging wall vertical records of a thrust event become important in reducing the trade-offs in the inverse problem. Unfortunately, perhaps due to a bias based on the experience with previous studies of mostly strike-slip events, where the vertical components are small in amplitude and hard to model with the simple 1D structure, the hanging wall vertical records were not used in the several previous Chi-Chi earthquake studies [e.g., *Chi et al.*, 2001; *Zeng and Chen*, 2001].

Theoretically, the fault model constrained by local datasets should also be able to explain the far-field observations, because the source is unique. However, using such data as an independent verification of a proposed source model is rarely done. In Figure 5.7, we compared the teleseismic velocity records with the synthetics generated with our preferred model. In this calculation, the 1D Central Taiwan layered model (Table 5.1) is used to generate the source excitation. An attenuation factor, expressed as a t^* of 1 sec is used for P waves and a 4 sec factor is used for SH waves [*Langston and Helmberger*, 1975]. The agreement between synthetics and data is remarkable, considering we assume the stations are sited on a half-space earth which is a poor approximation for the higher frequency waves. Thus, most of the disagreements are probably caused by the local structures beneath the teleseismic stations rather than the earthquake excitation. Thus the calibration of sites of the teleseismic stations by studying the aftershocks may be required both in timing and waveform distortion before including these records into inversions.

5.6 Rupture kinematics

In addition to the slip distribution, both the rupture initiation time and the rise time function are determined per subfault as displayed in Figure 5.3. For the convenience of discussion, we convert the slip history into a series of snapshots in 3 sec intervals. They are plotted in Figure 5.8 accompanied by the surface break trace during the Chi-Chi earthquake for reference. The overall rupture is slow (average rupture velocity is 2.0 km/sec) but very heterogeneous (appendix). It starts with a slower than average velocity, then gradually increases to 2.1 km/sec and propagates bilaterally to the south and north. The northward propagation is well determined by several hanging

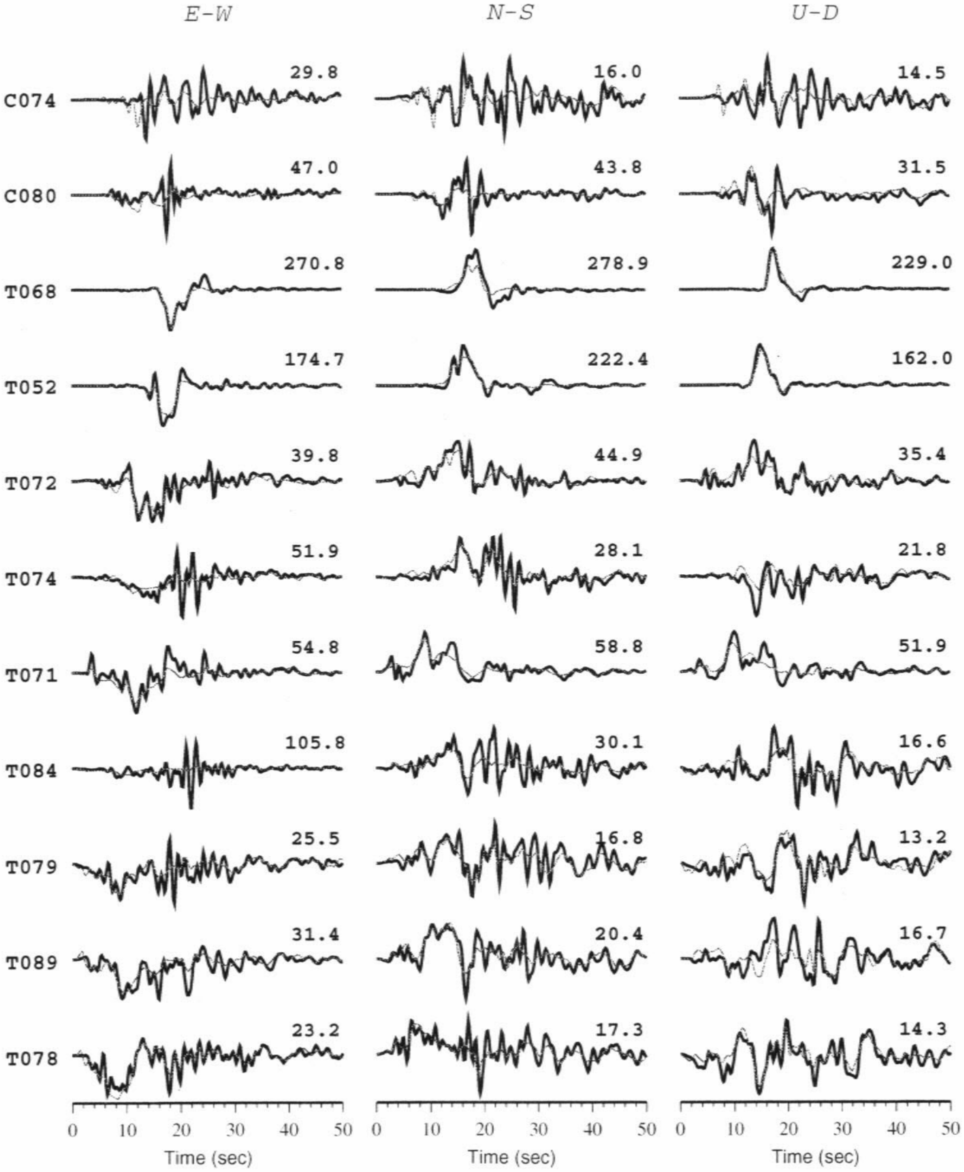

a

Figure 5.5: Comparison of strong motion velocity data (thick lines) and synthetic seismograms (thin lines). Both data and synthetics are aligned by the P arrival. The number at end of each trace is the peak velocity (cm/s) of the data and both data and synthetic seismograms are normalized by this value. (a) hanging wall (Group-1). (b) footwall stations (Group 2). (c) distant stations.

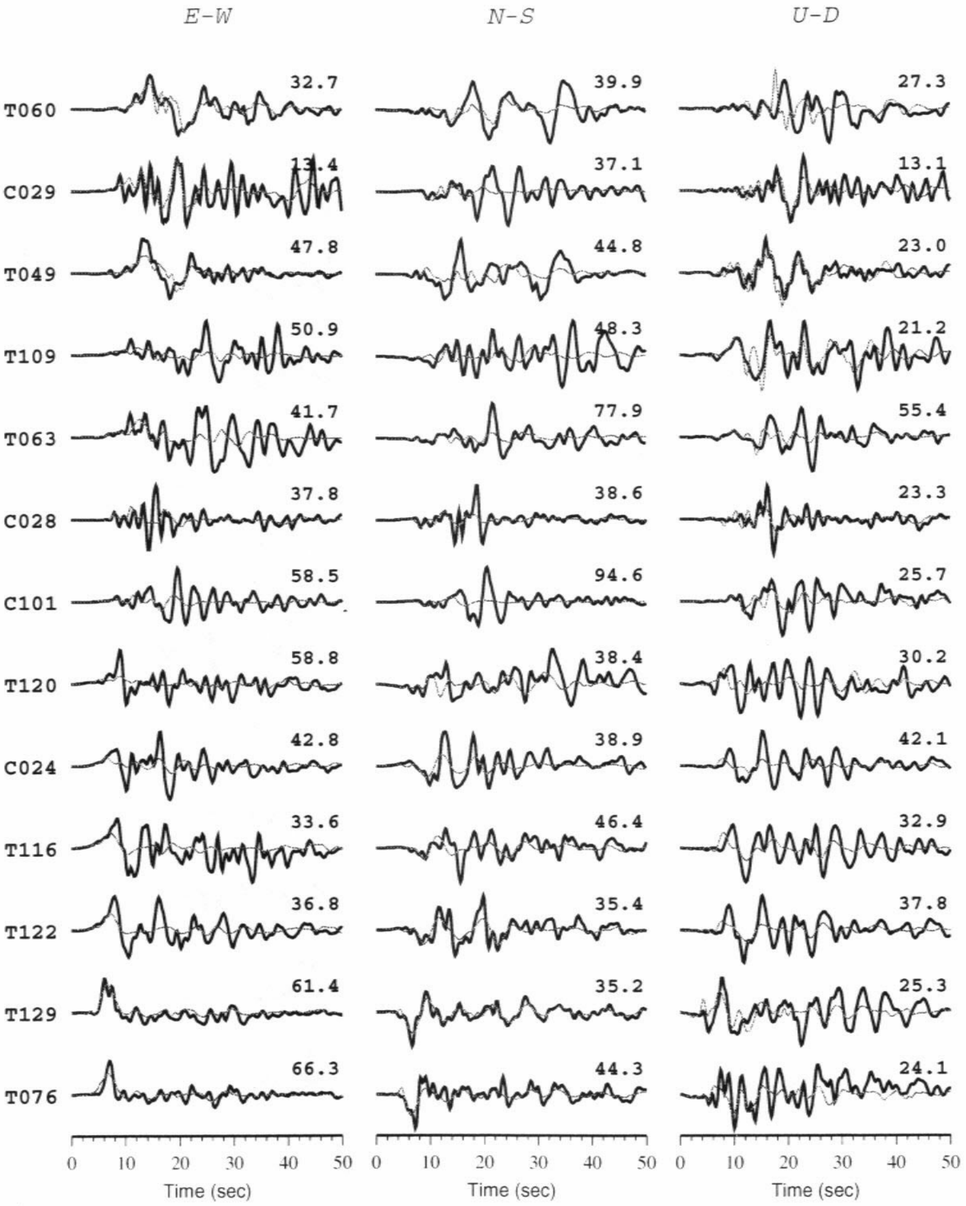

b

Figure 5.5b continued

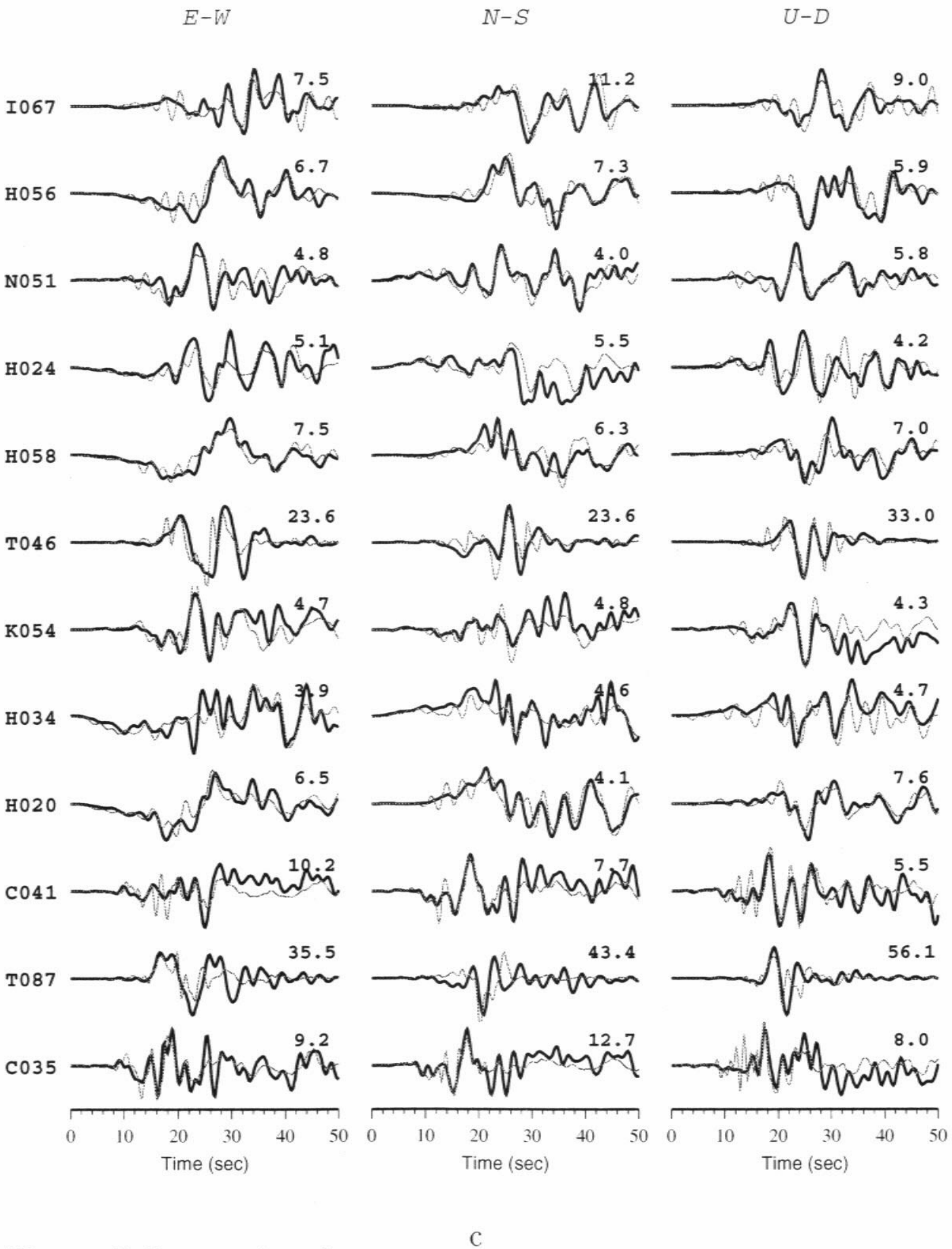

Figure 5.5c. continued

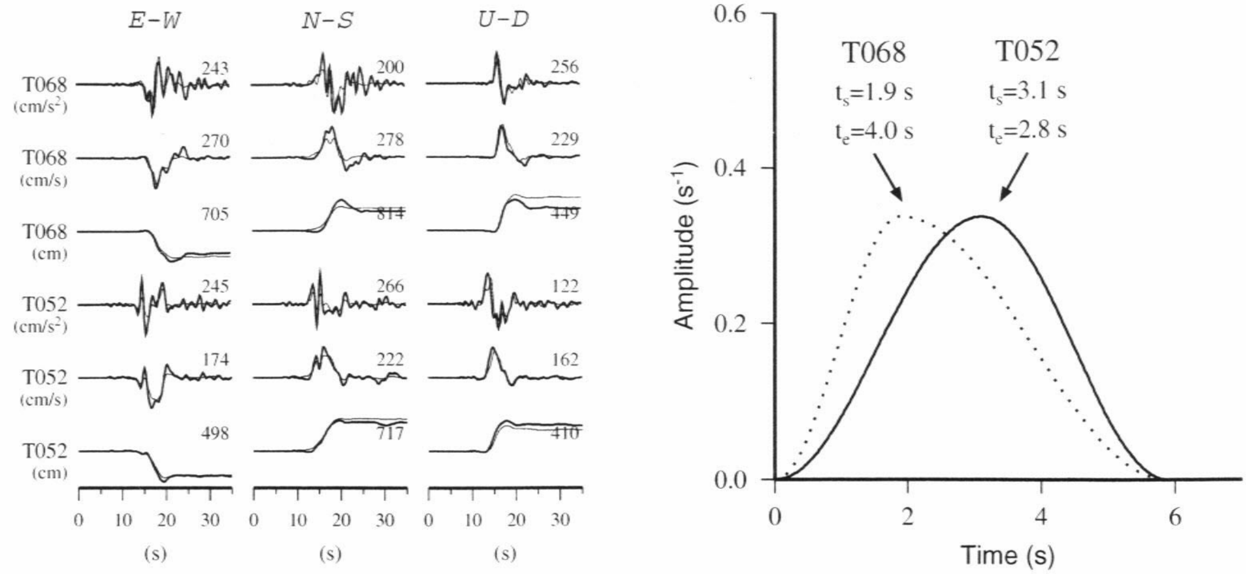

(a) (b)

Figure 5.6: (a) Forward predictions of stations T068 and T052. The displacements, velocities and accelerations of these two stations are compared with the synthetic predictions. Note that only the velocity records are used in the inversion. (b) The derivative rise time functions of the subfaults located beneath these two stations.

wall stations and shows a strong correlation with the bends of the Chelungpu fault. This will be addressed in detail later.

The "starting phase" and "end phase" times are inverted separately. The sum of them represents the particle slip duration or rise time *Heaton* [1990], which is displayed in Figure 5.9. Apparently, the distribution of slip duration is not totally random and seems roughly proportional to the slip amplitude. Furthermore, the big triangular asperity seems to be surrounded by a region with extended rise times. Such observations are also appeared in the slip history of several previous studies [e.g., *Ma et al.*, 2001; *Chi et al.*, 2001; and *Zeng and Chen*, 2001]. The average rise time over entire Chi-Chi rupture and weighting by the slip amplitude is 7.2 sec, which is significantly larger than the values of the previous studied earthquakes [e.g., 1992 Landers earthquake; 1999 Hector Mine earthquake].

The ratio of the "starting phase" and "end phase" times is not a constant value, instead, it varies over a broad region. In Figure 5.9, we also show the probability distribution of such ratios in a logarithmic-decimal plot. Note that there is a large peak around 1, and the average value is 1.3. Hence, although the slip on some subfaults show strong evidence that asymmetric derivative rise time function are required (e.g., Fig. 5.6); symmetric ones are still the most favorable solution on average for most of the fault. However, the average ratios may be specific to this earthquake; this feature may or may not be a general characteristic of large earthquakes based on our observations alone.

5.6.1 Rupture propagation on a rough fault plane

Usually, the surface expressions of thrust faults are much more sinuous than for strike-slip faults [P. Tapponnier, personal comm., 1999]; this appears true for the Chelungpu fault. In particular, there is a "bulge" [*Zeng and Chen*, 2001] at about 12 km to 25 km north of the epicenter indicated by arrows in Figure 5.9. The adjacent Chunghua and ShuangTung faults have similar curvature (Fig. 5.2 and 5.9) with the initial western step located at roughly the same latitude. In our simple model, such curvature and the potential downdip extension (corrugations) are not taken into account. However, the slip distribution seems to show a clear correlation with the shape of the fault trace. In the fault plane east of the hypocenter, there are three low slip zones extending east west (indicated by arrows, Fig. 5.9a). Two of them connect with the beginning and end of the "bulge", the last one links with the small curve just south of station T052. The downward extension of the low slip zones suggests that the surface curvature is a deep-seated feature.

Zeng and Chen [2001] noticed the rupture slows down when it crosses the above "bulge" and suggested that such geological curvatures acted like a barrier and blocked the northward oblique rupture propagation. This feature also appears in our preferred model but in a more detailed and physically plausible way. For the slip on the fault plane shallower than 8 km, the rupture front does not extend during the 12 to 15 sec interval (Fig. 5.8) when the rupture front meets the northern edge, or right-step of the "bulge". In contrast, the rupture front crosses the south side, or left-step without any delay. Hence, for a left lateral oblique motion, the north side of "bulge" rather

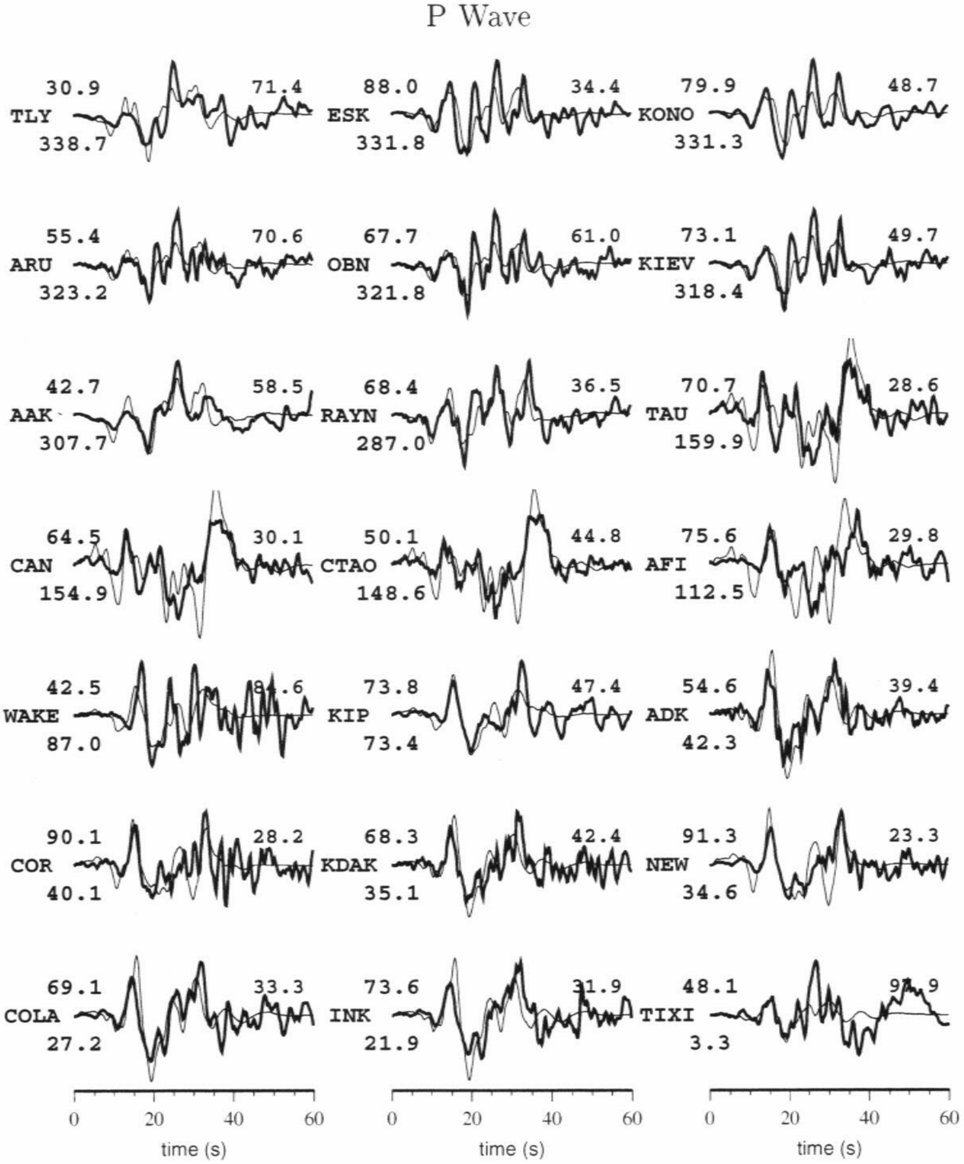

(a)

Figure 5.7: Comparison of teleseismic velocity data and synthetic predictions. The data are aligned by the P or SH arrival, respectively. The number at end of each trace is the peak velocity of data in microns per second. It is used to normalize both data and synthetic seismograms. The number above the station name is the epicentral distance and below it is the azimuth. (a) Comparison of P waves. (b) Comparison of SH waves.

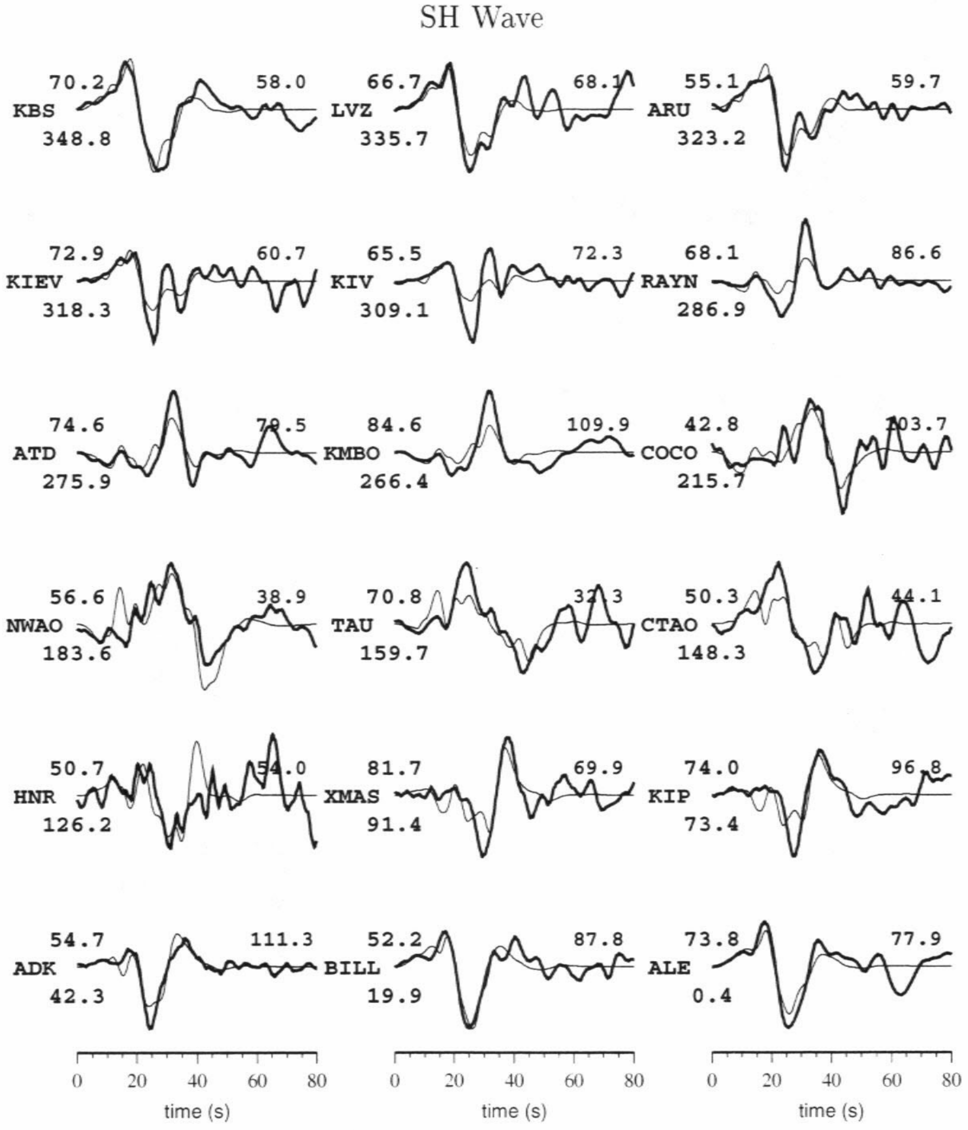

(b)

Figure 5.7. continued.

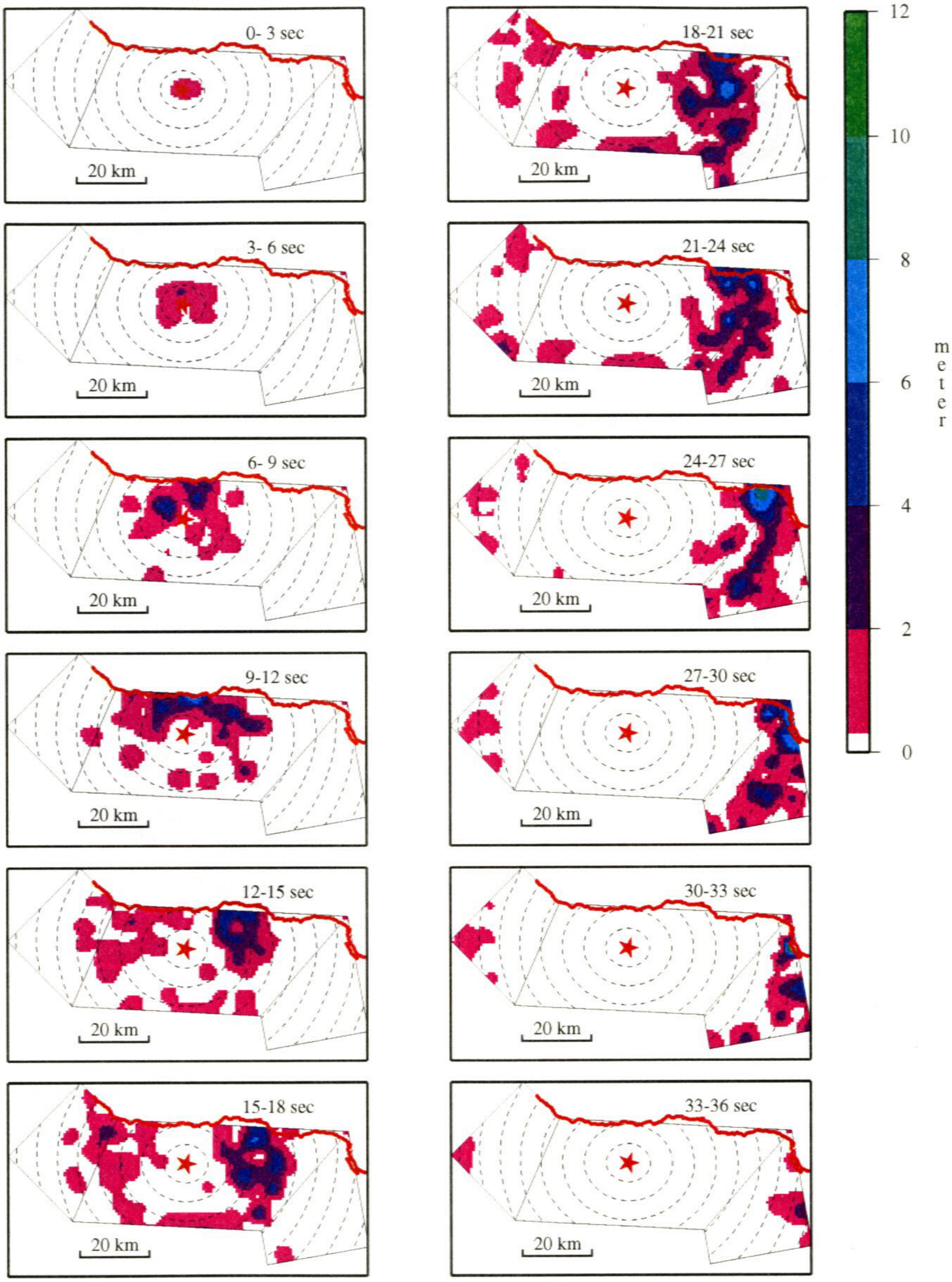

Figure 5.8: Snapshots of the 1999 Chi-Chi earthquake source rupture. The color shows the slip amplitude and a red star indicates the hypocenter. The surface trace is also plotted for reference. The contours show the positions of rupture front in a 3 sec interval if rupture velocity is 2.1 km/s.

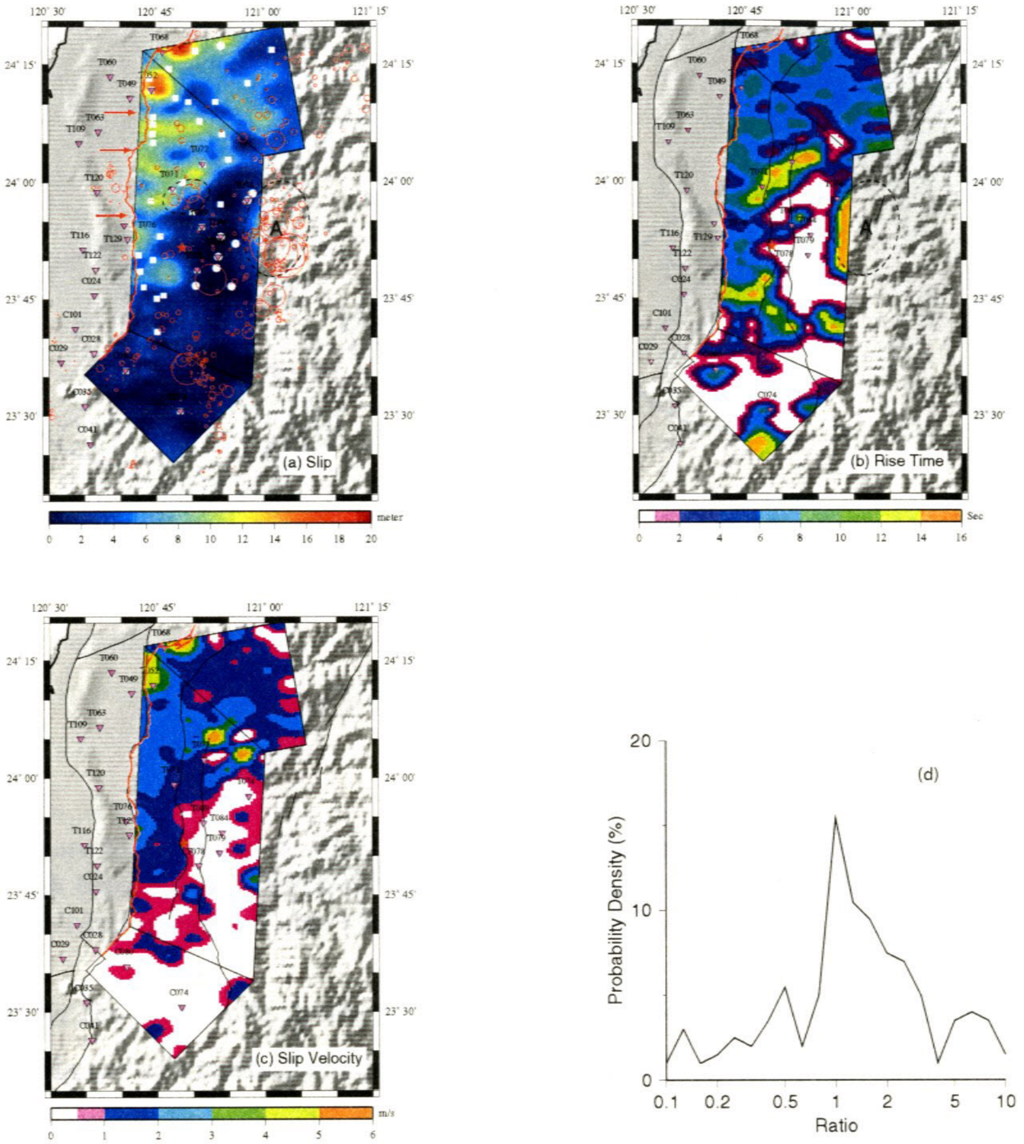

Figure 5.9: Map views of rupture characteristics of our preferred model. (a) Slip distribution on the base map of local topography and local active faults. We use color to shows the slip amplitude, the red star for the epicenter, circles for the aftershocks, red traces for the surface break, black lines for the local major faults. Five faults are plotted, the ChungHua, Chelungpu, ShuangTung, and LiShan fault from west to the east, respectively. The size of circle is proportional to the M_L of the events. Several near fault strong motion stations are also plotted as triangles. Note the aftershock cluster to the east of hypocenter (region A) and the small cluster in the south of station T071 (region B), which are discussed detailed in text. (b) Rise time distributions. Note that if the slip amplitude is less than 1.0 m, its rise time is probably hard to determine reliably. Only the subfaults with over 1 m slip are displayed. (c) Slip velocity distribution. The color is used to show the peak slip velocity. The 1 m amplitude threshold is also used. (d) Distribution of the ratios of starting and ending phase times.

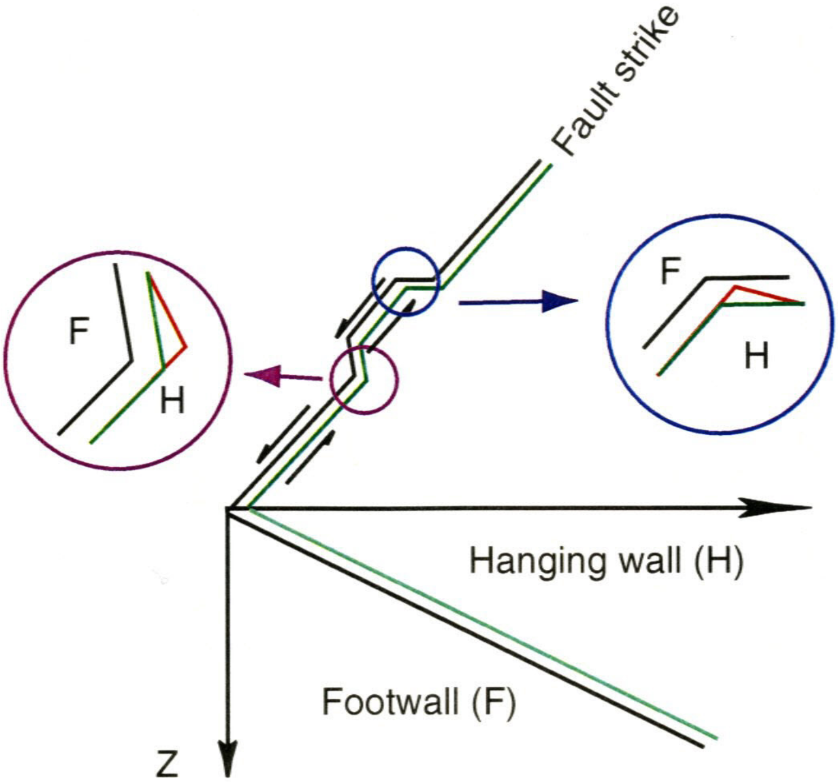

Figure 5.10: Effect of a fault step-over. The 3D cartoon displays the Chelungpu fault with black line, the footwall fault surface (F), and green line (before rupture) and red line (during rupture) for hanging wall surface (H).

than the south side decelerates the rupture propagation. This observation can be explained schematically with the cartoon in Figure 5.10. Note that left lateral oblique motion will kinematically "open" the fault zone between the hanging and footwall at the left-step in the "bulge" but "close" that at north boundary. Effectively, these represent dilatational and compressional step-overs, which reduce the normal stress on the south boundary but increase it on the north side, changing the fault friction and causing the alternative kinematic behavior shown in Figure 5.8. Such quasi-static effects had been suggested by *Segall and Pollard* [1983] in the study of the strike-slip events of California, and discussed in detail in *Scholz* [1990].

However, the slip on the fault plane in deeper regions (8-12 km) yields a different scenario. From the snapshots during 6 to 15 sec, we note that the rupture front clearly delays in this region compared with both the shallower and deeper rupture

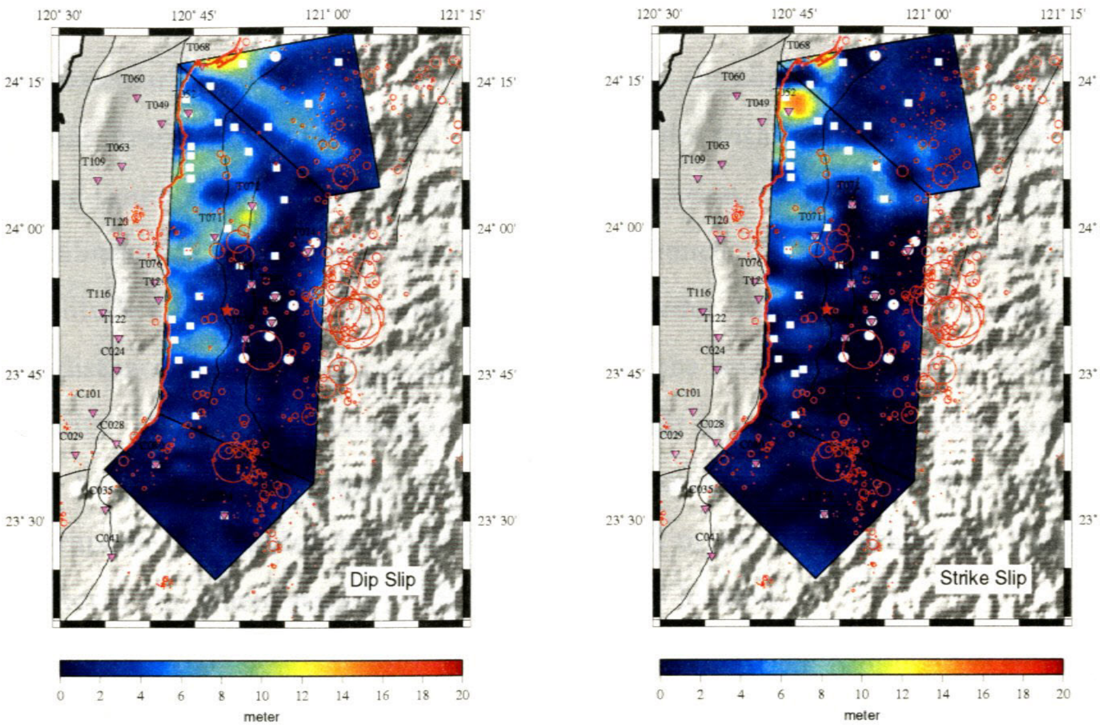

(a) (b)

Figure 5.11: Slip decomposition. The oblique motion of the Chi-Chi earthquake is separated into the dip slip component (right) and strike slip component (left). The slip amplitude is shown by color. Note that the increment in strike slip component when the slip is close to the intersection.

(snapshot at 9-12 sec, Fig. 5.8). We should point out that such a result is not at odds with the earlier example because the slip direction in this region changes from an oblique thrust to a nearly pure thrust (Fig. 5.11). The aforementioned mechanism is suitable for the strike-slip motion. The variation in slip direction implies that the pre-stress accumulations are different between this part and rest of fault plane. It is noteworthy that in a map view, a small cluster of aftershocks at the southeast of station T071 (Fig. 5.11) is close to the interface separating the two regions with different slip directions, and it is probably related to this feature even though their precise hypocentral depths are not known. A careful analysis of the aftershock cluster probably could shed new information related to this interesting puzzle.

5.6.2 Peak slip velocity distribution

A particularly interest result of this study is that the slip and rise time distributions appear directly related (Fig. 5.9), i.e., the subfaults with large slip amplitude require a long time to slip. To further display this observation, we plot the peak slip velocity distribution in Figure 5.9c, which indicates a much simpler pattern than the slip amplitude and rise time distributions. To first order, the slip velocity increases with the distance of rupture propagation related to the southeast boundary of the large asperity. The southeast boundary of the triangular asperity has larger slip amplitudes with longer rise times where its slip velocity is small (in the range of 1 m/sec). As the rupture propagates, this value increases to 2 m/sec and reaches over 3 m/sec at the north tip, where stations T052 and T068 are located.

For low angle thrust faults that break the surface, dynamic numerical simulations indicated the surface boundary condition plays an important role in dynamic rupture [*Brune*, 1996; *Oglesby et al.*, 1998]. Numerical and laboratory experiments show that the slip velocity will be amplified in the top few km. In our result, we find the slip velocities on the near-surface subfaults are larger in general. But the increments related to the deeper subfaults are not as large as the theoretical prediction *Oglesby et al.*. However, both the theoretical simulation and inversions are limited. The Chi-Chi event is not pure thrust event, and large strike-slip motions are involved. The behavior of the oblique slip in such an irregular fault surface has not been well resolved in the dynamic simulation yet. Secondly, our inversion assumes large subfaults with uniform rise time and slip Hence, our results here reflect averaged effects. Further studies with fine subfaults should help to evaluate this theoretical prediction.

Dynamics simulations also indicated that the hanging wall moves rather independently of the footwall, and the motions are concentrated in the hanging wall [e.g., *Oglesby et al.*, 1998; *Oglesby and Day*, 2001]. *Brune* [1996] and *Ni et al.* [1999] further argued that a dynamic decoupling of the hanging wall from footwall will cause the fault plane to be opaque to seismic radiation and will prevent the hanging wall motion from radiating to the far field. This simply implies that the far field radiation energy

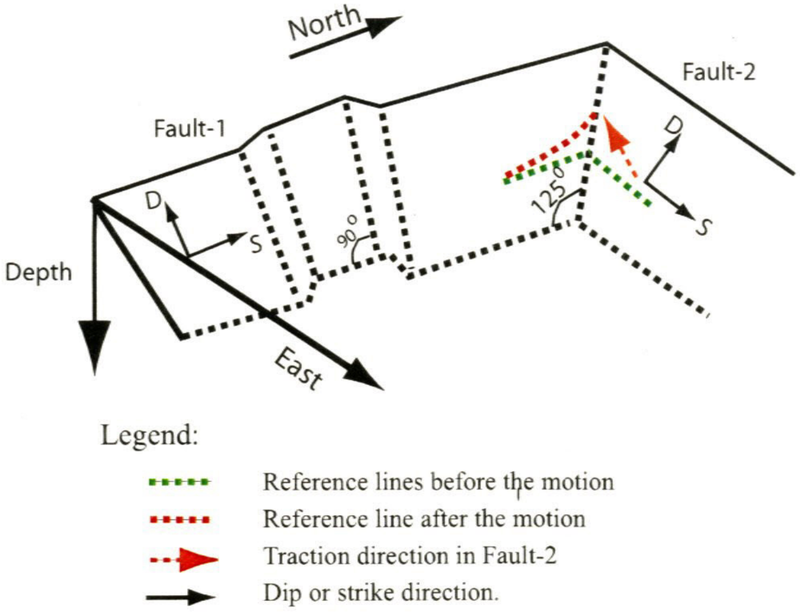

Figure 5.12: Effect of the intersection of Fault-1 and Fault-2. The 3D cartoon represents the footwall of two major fault segments of the Chi-Chi event. The green lines represent a reference line on the hanging wall. The corresponding after slip position in Fault-1 is shown by red dashed line. Note that the motion on Fault-1 will create a westward traction on Fault-2 accompanied with an uplift traction.

will be lower than expected *Brune* [1996]. However, since we have ignored this possible opaque behavior, the favorable forward prediction of the teleseismic body waves (Fig. 5.6) suggests that the difference is very small. This result is consistent with the numerical simulation of *Aagaard et al.* [2002].

5.6.3 Intersection between the Fault-1 and Fault-2

The previous static inversion (Chapter 4) indicated that these two fault planes form the surface of a "wedge" shape block. The co-seismic slip was limited to its surface. Because the rupture direction changed roughly 90 degrees across the hinge line, the intersection of these two planes, or the "hinge line" of the block, seems to be an important barrier to the propagation of the dynamic rupture. Unfortunately, our resolution around this intersection is limited because of absence of strong motion stations right above this region. It is the reason why we use a rather sharp intersection here, even though the "hinge line" probably needs to be addressed with smaller grid size and assumed as a narrow transition zone.

However, the overall kinematics characteristics near the hinge line are fairly determined. The rupture front reaches the bottom of the hinge line first, and then arrives near the surface portions about 6 sec later (Fig. 5.3 and 5.8). We have not observed significant delays when the rupture crosses the intersection (Fig. 5.9). In fact the rupture is slightly faster than the average value as indicated by the snapshots at 15-18 sec and 18-21 sec seen in Figure 5.8. The variation of slip velocity around the "hinge line" is relatively complex. They are extremely large on some deep subfaults close to the hinge line, which are possibly related to the rupture initiation of the transition zone. For the slip in the intermediate depth range (4-10 km), the hinge line separates the region in Fault-1 with over 2 m/sec slip velocity from the region in Fault-2 with less than 2 m/sec as we discussed early.

There are two interesting questions related to the rupture of the intersection. First, it seems difficult to understand why the initiation time of rupture does not have a large delay when traversing the intersection even though the rupture propagation direction has changed by over 90 degrees. Because of the existence of large strike-slip motion in the side of Fault-1, it seems to be a contradictory example of our previous quasi-static explanation, i.e., compressional step-over does not slow the rupture down. Second, for the strike slip motion, the hanging wall of Fault-1 extends to the north (left lateral); the favorable motion direction of hanging wall of Fault-2 seems to be east (left lateral) instead of west (right lateral).

Even though we probably need to perform a 3D numerical simulation to really understand these two questions, the quasi-static cartoon in Figure 5.12 will help us to address them to some extent. Note that the intersection is no longer normal to the fault strikes. Instead, the "hinge line" has a rake of 55° in Fault-1 and a rake of 125° in Fault-2. In this particular geometry, the uplift of the hanging wall near the "hinge line" will make the northward extension of the hanging wall of Fault-1 (left lateral) and the westward extension of the hanging wall of Fault-2 (right lateral) easier. Such mechanism is supported by the fact that strike-slip component in Fault-

1 (Chelungpu fault) increases on the subfaults close to the intersection (Fig. 5.12). Then, quasi-statically, the "close" effect at the "compressional step-over" (Fig. 5.9) is compensated by the "increment" in extension space to some extent. Hence, the effects of the "hinge line" are very complex, but their accumulated influence to the rupture propagation is probably small. Or in other words, the nature of faulting proceeds an efficient way.

The previous static inversion (Chapter 4) indicated that even though the slips on both Fault-1 and Fault-2 have important strike slip components, the vector sum of co-seismic slip was in good agreement with the nearly pure thrust focal mechanism solution of Harvard CMT. The derived maximum compressional axis has an azimuth of N303°E, nearly identical to the CMT solution (N304°E), and matches the trend of local compressional stress direction obtained by analyzing geological and geophysical data [N302 ± 20°E, Hu et al, 1997]. Such direction is also close to the N305°E plate convergence azimuth [Seno et al, 1993]. The vector summation result does not change in our current model. Combining this agreement in stress direction with the observation that the relatively large slip around the intersection of Fault-1 and Fault-2 suggests that the slip involving two fault planes is likely due to pre-stress and that the occurrence of Chi-Chi earthquake reflects the "wedge" shaped block motion pushed by the local tectonic stress field (Chapter 4).

5.6.4 Effect of afterslip

In this study, we invert for the slip history of the Chi-Chi event by fitting both seismic and static data simultaneously; the inversion routine tries to find the model that has a minimum value of the objective function defined by formula (2.15). It is noteworthy that such a result may not be the solution closest to the real rupture, particularly when the data contain significant noise. Since the GPS measurements of the Chi-Chi mainshock included the effects of some aftershocks and aseismic afterslip [*Yu et al.*, 2001], additional slip should expect to be included in the inversion results to match the GPS measurements. However, the strong motion data only include the effects of co-seismic slip during first minute after the rupture initiation. The aforementioned additional slip is more likely to decrease the fit to them rather than improve. The only way to improve the fit to the GPS measurement without a large degradation of the fit to the seismic data is to increase the slip duration simultaneously. During this study, we find an example of such inverted artifact in the region where large afterslip might be expected.

In a map view, the biggest aftershock cluster shown in Figure 5.10a is located at roughly east of the hypocenter. This cluster has two Mw>6 aftershocks which are included in the epoch surveyed static measurements [*Yu et al.*, 2001]. The source parameters of these two events have been determined independently [e.g., *Kao and Chen* [2000]]. One event (1999/9/22) had a moment magnitude of 6.2 but was 29 ± 3 km deep, another (1999/9/25) is the largest aftershock of the Chi-Chi event, and had a magnitude of 6.4 and was 15±4 km deep [Kao and Chen, 2000]. Thus the latter one generated the most of static effect which was predicted to be 10's of cm. In our inverted model, there is a small asperity composed of four subfaults at the bottom of Fault-1 (about 15-17 km, Figure 5.3), which is close to the aforementioned aftershock cluster (Figure 5.10). The seismic moment of the four subfaults is equivalent to an earthquake with moment magnitude of 6.6, slightly larger than that of the biggest aftershock. Finally, all subfaults of this asperity have the longest rise time permitted in our inverted procedure. Hence, it has a very small contribution to the velocity strong motion waveforms. This is an unprecedented recovery of post-seismic slip (a large aftershock), where the static signal necessary to fit the "contaminated" geodetic data is given a sufficiently long rise time to avoid misfitting the seismic waveforms.

Fortunately, on most of the fault surface with large slip, significant aftershocks are absent. The continuous GPS measurements also suggested few afterslips are in the northern portion of the Chi-Chi rupture plane [Yu et al., 2001]. So it is probably safe to constrain the slip model with both GPS and seismic data, even though the interpretation of the results must be handled carefully.

5.7 Conclusions

We have inverted both strong motion records and GPS data to generate the rupture characteristics of the 1999 Chi-Chi earthquake using the inversion procedure developed by *Ji et al.* [2001]. Three-plane fault geometry constrained by the static only inversion *Ji et al.* [2001] is applied to investigate the kinematic rupture characteristics using 119 three-component GPS measurements and 108 velocity seismograms.

We found that there is no difficulty encountered in explaining the strong motion data with this new fault geometry. In addition, the inverted fault model can explain the independent teleseismic P and SH velocity waveforms quite well. The total seismic moment of Chi-Chi is 2.7×10^{20} Nm, in agreement with the seismic moment estimates of Harvard and the USGS. Most of the moment is released in a big triangular shaped asperity beginning 12 km north of hypocenter and involving both fault segment 1 and 2. After analyzing the slip distribution and rupture evolution, we find the complexity of rupture during the Chi-Chi earthquake has the following relations with the fault geometry.

1. The occurrence of 1999 Chi-Chi earthquake reflect the motion of a "wedge" shaped block driven by the local tectonic stress. Because the trend of the current compresional stress direction is not normal to the pre-existing weak zone, the Chelungpu fault and the unnamed fault segment (Fault-2), the strike slip motions make an important contribution on both Fault-1 and Fault-2 even though the vector summation of them is nearly pure thrust.

2. The slip distribution implies that the jog in the fault trace of the Chelungpu fault is a deep-seated feature. The kinematic rupture behavior of the Chi-Chi earthquake is consistent with the expected affect of such a geometry on the occurrence of the strike slip motions.

3. The intersection between the Chelungpu fault (Fault-1) and Fault-2 does not act as a "barrier" that delays the rupture. This result is also consistent with that particular fault geometry around this intersection.

4. The peak slip velocity in Chelungpu fault seems to increase as the distance

of rupture propagation; it also becomes larger near the free surface as predicted by physical experiments [*Brune*, 1996] and dynamic simulations [e.g., *Oglesby et al.* [1998]].

5.8 Appendix: Rupture velocity of 1999 Chi-Chi earthquake

The determination of the kinematic rupture velocity is very important for the purpose of understanding earthquake dynamics. Particularly, the ratio of rupture velocity to shear velocity is tightly related to the fracture energy, the earthquake energy used in break the rock. It is generally established that the rupture velocities for large shallow earthquake are about 75-85 percent of shear velocities [*Heaton*, 1990], which implies that the fracture energy is only a small portion of seismic energy and can be neglected [*Kanamori and Heaton*, 2000]. However, the recent study of 1999 Hector Mine earthquake showed an exception, where the average rupture velocity was only about 1.9 km/sec, or 55 percent of the shear wave speed [*Ji et al.*, 2002b]. The 1999 Chi-Chi event was recorded by the best strong motion coverage to date, so it provides a unique opportunity to more accurately determine the rupture velocity, or rupture evolution.

The previous results from various groups are close but significantly different from what we found here. Yugi and Kikuchi [1999] reported the first slip distribution of this event on their WebPage. They used an average rupture velocity of 2.5 km/sec to model the teleseismic data. With same dataset but with an Empirical Green's function approach, Ma et al. [2000] reported that the distribution of rupture velocity is very heterogeneity, and varied from 1.6 km/sec to 4.0 km/sec. A rupture velocity of 2.5 km/sec seems to be confirmed by the finite fault studies preformed by *Wu et al.* [2001], *Chi et al.* [2001] and *Zeng and Chen* [2001] in the special issue of BSSA. Taking advantage of many close fault-trace records, *Chen et al.* [2001] estimated the rupture velocity directly by the time delay between the S first arrival and signal from rupture pulse that nucleated from an asperity near and underneath the stations. They found the rupture velocity varied from 2.28 to 2.69 km/sec with an average rupture velocity of about 2.49 km/sec. Thus, even though there are some scatter, all previous studies seem to favor a fast rupture velocity of 2.5 km/sec, in contrast with 2.0 km/sec found in this work.

We found that such differences can be explained by the uncertainties embedded in these methods. In general, above studies can be separated into three catalogs based on the ways measuring rupture velocity. The first one includes near all finite fault studies except the work of Zeng and Chen [2001]. In this catalog, the Green's function of each subfault is pre-calculated with a constant rupture velocity, and such default rupture velocity is usually larger than the highest possible rupture velocity. For example, *Wu et al.* [2001] used a value of 3.0 km/sec. The slip rate function, or derivative rise time function of each subfault, is modeled by multiple time windows. If the real rupture velocity is slower than the default one, the slip will occur at later time windows. However, with this approach, The rupture initiation time of each subfault does not vary continuously. Instead, it changes discretely with half-width of time windows, which is 1 sec in the several previous studies. This will cause the uncertainty in rupture velocity estimation. For instance, suppose, for a partcular subfault, the real rupture starts at 0.5 sec later than the beginning of its first time window, we would expect that, in the inverse result, the rupture time will still be the beginning of its first time window. Or in other words, the average rupture velocity determined by methods in this catalog will expect to be faster than the real condition.

The fault representation of *Zeng and Chen* [2001] is very similar to what we used here. In this catalog, the rupture initiation time becomes a free parameter, and the above bias is limited. The difference in rupture velocity is probably caused by differences in the data processing and alignment. In our study, we aligned data by the P wave first arrivals, while they used S waves instead. Because there is no report of a fore-shock, it is probably safe to use P wave instead of S wave. As we discuss next, the S wave from the hypocenter is notoriously difficult to pick. What we get is more likely arriving from a later portion rupture rather than the exact nucleation. If so, the estimated rupture velocity in their result would be greater. However, we admit that because the slip-rate functions used are not as flexible as the first approach, the uncertainty in rupture velocity also exists. Hence, additional analysis is required.

Chen et al. [2001] attempted to measure the rupture velocity directly from the seismograms. Their results depend on the pick of the slip pulse, and the S wave as well as S wave velocity structure. However, the later two are very rough and questionable. The largest rupture velocity they obtained is 2.69 km/sec, which is the average rupture velocity from hypocenter to the station T129. In Figure 5.13, we show the records at stations T129 with 4 time marks. The time marks P and S are the arrival time of P wave and the predicted S arrival time with the central Taiwan velocity structure (Table 5.1). The S' marks the S arrival time picked by *Chen et al.* [2001], which is 0.65 sec later than the theoretic prediction. The time mark S1 labeled the phase from the slip pulse nucleated near the station T129. Because the hypocentral distance is only 16.2 km [*Chen et al.*, 2001], the difference between S and S' is too large to be entirely attributed to error in velocity model. The differential time between time marks S' and P is 2.9 sec. We found that a P wave velocity of 9.4 km/sec is required to generate such a difference if we use the same shear velocity of 3.46 km/sec as [*Chen et al.*, 2001]. Furthermore, if we logically assume a Poisson medium, the shear velocity will be only 2.36 km/sec. Hence, the pick of S wave is not correct, even though it looks reasonable. This illustrates the difficulty in picking the S first arrival time for such a finite source. Here, we suggest using P wave rather S wave to estimate the rupture velocity. Simply assuming a P wave speed of 6 km/sec and using the S1 pick of *Chen et al.* [2001], we get a rupture velocity of 2.3 km/sec, 0.39 km/sec smaller than the previous value. Such analysis can be further improved, since we can estimate the original time of each record reasonable well [*Huang*, 2001]. Then the rupture velocity value becomes 2.1 km/sec and is very close to what we obtain in the inversion. Because the difficulty in pick S wave is a common feature, most rupture velocities determined by *Chen et al.* [2001] are overestimated. Based on the new approach, the average rupture velocity will drop to about 2.0 km/sec in which case the results are also consistent with *Huang* [2001]. Based on a layered earth model, the average rupture velocity of 2.0 km/sec is about 66 percent of shear velocity in a depth from 4 km to 9 km, and about 90 to 100 percent of shear velocity in the top 4 km.

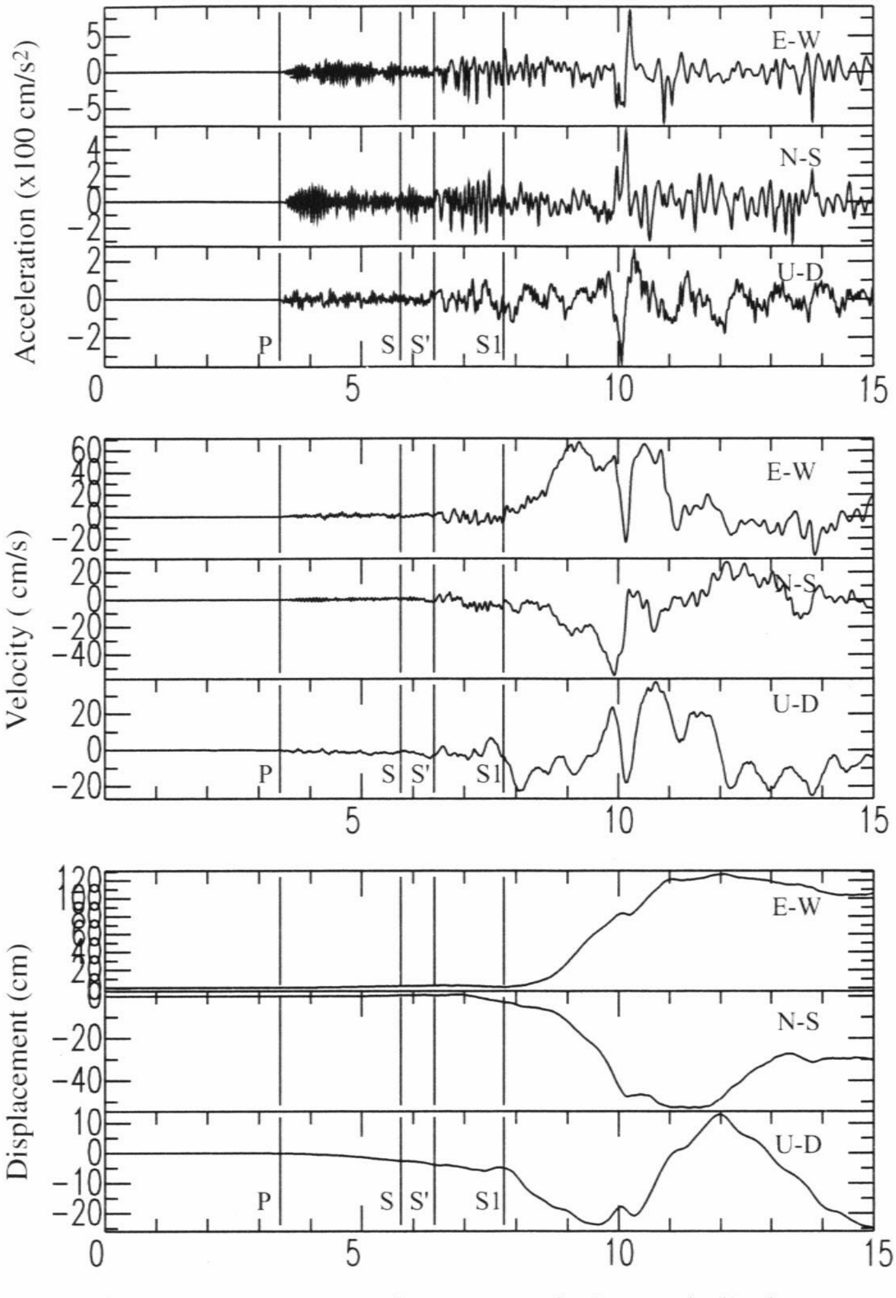

Figure 5.13: Three-component acceleration, velocity and displacement at station T129. The station T129 is west of the epicenter at a hypocentral distance of 16.2 km *Chen et al.* [2001].

Chapter 6 Central Taiwan transfer zone

6.1 Introduction

The island of Taiwan is located at the boundary of the Eurasian plate (EP) and Philippine Sea plate (PSP); It witnesses the oblique relative motion of these two plates (Fig. 6.1). Currently, the EP subducts beneath the PSP in the south of Taiwan but is atop the PSP in the northeast of Taiwan (Fig. 6.2). The convergence rate between the PSP and EP near Taiwan is estimated by *Seno et al.* [1993] and *Yu et al.* [1997] to be 7-8 cm/yr. in N306°-309°E direction. Taiwan is formed by the collision between the strong part of the PSP, Luzon arc (Fig. 6.1), and the Asia continental shelf. Due to the oblique convergent characteristic, the collision moves progressively southwestward. It started at Northern Taiwan about 3 million years ago, and reached Taitung about 1 million years ago. In the future, the collision will occur at some place near Hong Kong (e.g., *Lallemand et al.*, 2001 *Lee et al.*, 1991). It appears that the southern Taiwan is still rising up due to the intense collision, but the tectonic style in northeast Taiwan has already evolved beyond the collision phase and is in the process of collapsing [*Teng et al.*, 2000]. The transition from collision to collapsing phases should be happening in the central and northern Taiwan, even though the location and mechanism have not been well elucidated.

As one of few active fold-and-thrust belts, the Taiwan orogeny has received much attention from the geoscience community. *Suppe* [1981] proposed the first comprehensive model for the formation of Taiwan. He suggested that the major topographic effect of the arc-continent collision is the expansion of the accretionary wedge in width and height as the Luzon arc encountered the thick sediments of Chinese continent margin. The mechanics of this process is similar to the deformation of a wedge of soil in front of a bulldozer [*Davis et al.*, 1983]. The soil deforms until a critical taper is attained. The critical taper is the shape for which the strength of the material within the wedge is balanced by the friction along the basal decollement. Because this model has been successful in explaining many elevation profiles along the slope of the western foothills (Fig. 6.1), the Taiwan mountain belt, in fact, has become a classical example for the critically tapered wedge model. Based on this theory, the mountain building in Taiwan will be limited to the top 15 km of crust.

There has been great improvement in geophysical observations of Taiwan during the last decade. Since 1991, the Central Weather Bureau seismographic network (CWBSN) with 75 stations, covering the whole island of Taiwan, started to report more reliable locations of local earthquakes (e.g., *Ma et al.*, 1996). The Broadband Array in Taiwan for Seismology (BATS), established in the later 1990's, offered more reliable focal mechanism solutions for earthquakes Mw $>$ 4 [*Kao and Chen*, 2000]. In addition to the advancement in seismic observations, the Taiwan GPS Network, composed of 131 annually surveyed geodetic monuments and 9 permanent stations, was established in 1989 to analyze the present-day crustal deformation. A surface deformation rate map of the entire Taiwan island was produced from the 1990-1994 record [*Yu et al.*, 1997]. Furthermore, the satellite-derived free air gravity anomaly map [*Sandwell and Smith*, 1994] and high-quality local Bouguer gravity anomaly map [*Yen et al.*, 1998] are rough but robust constraints to the density and topography variations related to the tectonic activity. Finally, the high resolution digital elevation model, side-looking airborne radar and satellite imagery enable us to present an integrated geomorphic description of the Taiwan orogeny [*Deffontaines et al.*, 1994].

These abundant observations have been used to study the structures and geodynamics of Taiwan, and as a result, some modifications to the Suppe's model have been proposed. For instance, *Rau and Wu* [1995] studied the crustal and upper mantle tomographic structures of Taiwan using the high quality data of CWBSN. They observed the thickening of the crust and a root-type structure under the Central Range. *Wu et al.* [1997] then suggested that the collision in central Taiwan involves the upper portion of the lithosphere ($>$ 60 km) of two plates. *Teng et al.* [2000] attempted to understand the flipped mechanism of the two subductions. They hypothesized that in northeast Taiwan, the subducted EP slab breaks off and creates an open zipper,

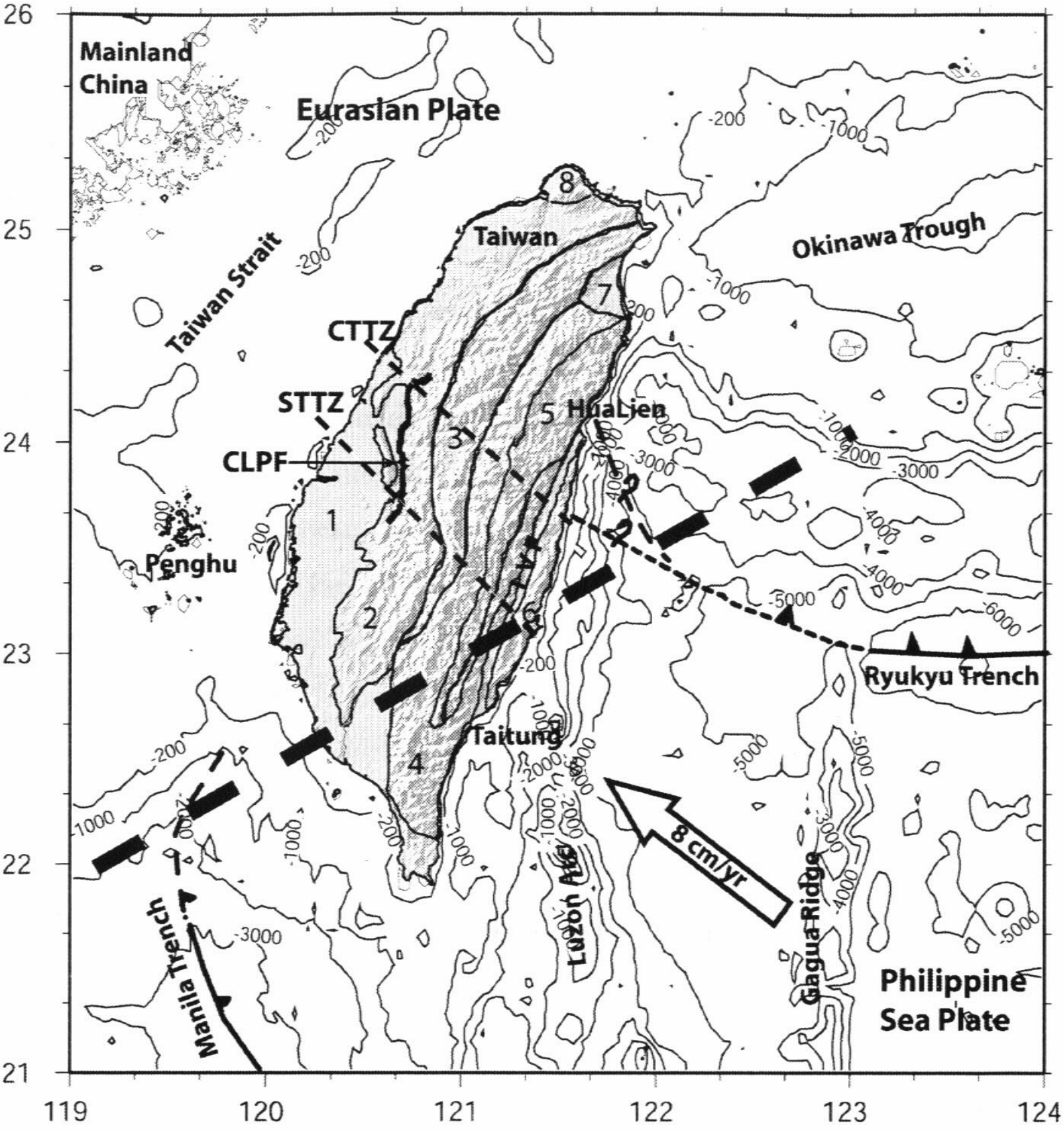

Figure 6.1: The overall plate tectonic map of the area around Taiwan (Modified from Wu et al. 1997). Contours show the bathymetric depth. Subduction along the Ryukyu and Manila trenches are indicated by solid barbs. The main geological boundary units are also indicated. 1=western coastal Plain (Quaternary), 2=Western Foothills (Plio-Pleistocene), 3=Hsueshan Range (Eocene-Miocene), 4=Backbone Range (Eocene-Miocene), 5=eastern Central Range (Pre-Tertiary), 6=Coastal Range (Miocene-Pleistocene), 7=Ilan Plain (Quaternary), 8=Tatun volcanic group (Pleistocene). LVF= Longitudinal Vellay fault. CLPF=Chelungpu fault. Finally, CTTZ=Central Taiwan transfer zone and STTZ=southern Taiwan transfer zone are defined in this study. The thick long-dashed line is the possible ocean-continent boundary of the Eurasian plate and the South China Sea plate.

which the mantle material of the PSP fills in. Such hypothesis was soon supported by a tomography study [*Lallemand et al.*, 2001]. In fact, this study also suggested that a much larger oceanic plate, the South China Sea plate (SCSP), had subducted beneath the PSP before the subduction of the EP [*Lallemand et al.*, 2001].

The complex interaction of two plates and the accumulated effects to the above sediments are probably too complex to be entirely explained without analyzing in a full three-dimensional environment and viewing evolutionarily. However, because the two plates are colliding obliquely, the future stages of collision can be inferred by surveying the collision behaviors further north. Then the sharp variations along the extension of Taiwan become extremely important temporal marks to the investigation of the ongoing Taiwan orogeny. In an initial work [*Ji et al.*, 2001], we noticed that the slip pattern of the 1999 Chi-Chi earthquake reveals an interesting geological observation, i.e., the fault plane turns over 90 degrees where the slip is the maximum. We then suggested that a transfer zone existed in the Central Taiwan following the hinge line of the bending fault surface (Fig. 6.1). We will address this transfer zone and discuss its tectonic implications in the following sections.

6.2 1999 Chi-Chi earthquake and two inferred transfer zones

As the largest inland earthquake in 20th century, the 1999 Chi-Chi earthquake is probably the most reliable indicator of the tectonic processes in the central Taiwan. It happened along a previously recognized active fault, the Chelungpu fault (CLPF), which marks the boundary between the western Taiwan foothills and western Taiwan coastal plain (Fig. 6.1). As the most pronounced feature of this earthquake, its fault trace turns 90 degrees clockwise where the surface slip reached the maximum [*Ma et al.*, 1999]. Based on the static inversions, *Johnson et al.* [2001] and *Ji et al.* [2001] found that such a bend is not just a surface feature; instead, it extends downward to over 10 km (Fig. 6.2). *Ji et al.* [2001] illustrated that the slip pattern is in fact well constrained by the dense GPS stations. Because the northern segment of fault plane dips 20-30 degrees to the south, it can not be explained with a vertical tear fault, which is usually followed by the elimination of large thrust events. Hence, the sharp bending action is not a dynamic effect; instead, it is probably caused by the interaction of pre-existing weak zones and the local stress field of central Taiwan. Such an argument is supported by the fact that the maximum compressional direction of this event is close to that of the plate convergent direction [*Ji et al.*, 2001], but oblique to the strike of CLPF. The turning of the Chi-Chi fault plane is not an isolated tectonic feature. The fault traces of two adjacent faults, the Shuang-Tung fault (STF) and the Shu-Li fault (SLF), either turn to the east or is connected by the east-west trending valley (Fig. 6.3). The fact that the turning points of the three fan shape fault traces fall in a line implies a concentration of the stress field.

The line linking turning points orients N140°E. Its extension meets the east coastal line at 23.4°N (the dashed line in the south, Fig. 6.3). As discussed later, the geophysical observations along the coastal line are sharply separated around 23.5°N, which is probably a transition from lithosphere collision to subduction of PSP [*Wu et al.*, 1997]. So we define an inland transfer zone with a width of 15 km, striking N140°E and bounded by the two dashed lines shown in Figure 6.3. According to its location, we name it the Central Taiwan Transfer zone (CTTZ). However, the geological units are continuous across this zone (Fig. 6.1).

The surface break of the Chi-Chi rupture not only turns at the northern end, it also turns about 45 degree clockwise at the south end [*Ji et al.*, 2001]. After turning, the right lateral strike slip motion occurred co-seismically, in contrast with the pure thrust and left lateral strike slip along the major segment of the CLPF, and right lateral strike slip at the north segment [*Ji et al.*, 2001]. There then is another linear transfer zone in the southern Taiwan. We call it the Southern Taiwan Transfer zone (STTZ), which has a similar orientation to that of the CTTZ. Note that the shape of many geological units have sharp variations across this line (Fig. 6.1), illustrating a significant variation in tectonic activity.

The two transfer zones separate Taiwan into three portions. For the convenience

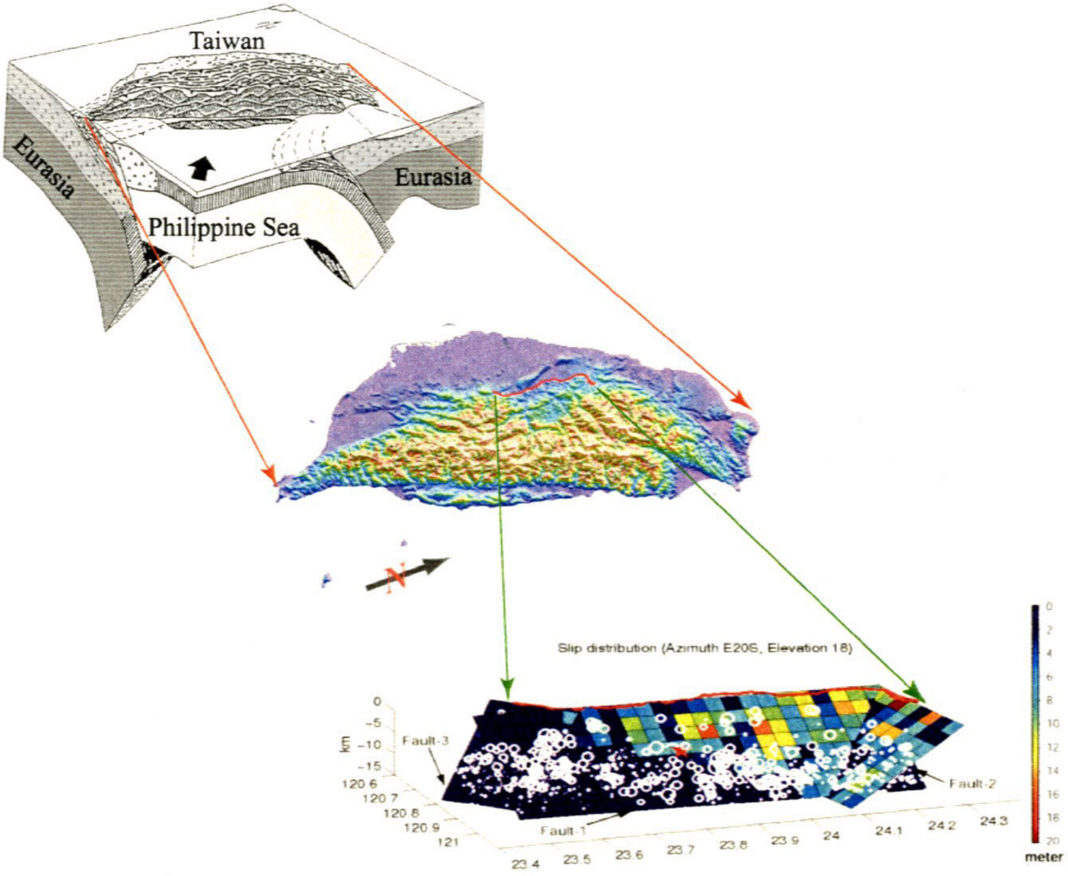

Figure 6.2: Tectonic framework [*Angelier*, 1986], topography and the slip distribution of the 1999 Chi-Chi earthquake [*Ji et al.*, 2001].

of later discussion, we call them southern, central and northern Taiwan, respectively. We should point out that these definitions are not entirely the same as those used in the previous studies (e.g., *Davis et al.*, 1983). In this paper, we will focus on the CTTZ, and provide evidence to illustrate that the CTTZ is a transfer zone at least in a geophysical sense.

6.3 Central Taiwan transfer zone

The CTTZ is cut by the Lishan fault (LSF, Fig. 6.3), which extends in a nearly NS direction. We will discuss the west and east segments separately because they have different characteristics.

6.3.1 West CTTZ

The west segment of the CTTZ extends from the west coastal line to the LSF with a length of 100 km. It cuts through two geological units, the West Foothills and the Hsueshan Range, but does not create large offsets (Fig. 6.1). However, the elevation on northern side is significantly higher than on the southern side. The west CTTZ has been suggested as a transfer zone by the several previous researchers (e.g., *Deffontaines et al.*, 1994) and received intense interest in the geoscience society of Taiwan during the last few years.

We plot the $M_L > 3$ earthquakes from 1990 to 1998 in Figure 6.4. A linear seismic zone inside the CTTZ can be clearly identical, which was called SanYi-Puli seismic zone (SPSZ) in the previous literature (e.g., *Chen and Chen*, 2000). This seismic zone was reported to be very active. For instance, CWBSN cataloged more than 10,000 earthquakes with M_L<5.3 located at the depth above 40 km from 1990 to 1997 [*Chen and Chen*, 2000]. Most of the earthquakes are limited within the two dashed line, and distributed in a depth region from surface to about 50 km (crosssection DD', Fig. 6.4 and 6.5).

The seismicity on the south side of the SPSZ is apparently much more active than that on the north (Fig. 6.4). In addition, the earthquakes on the south side of the

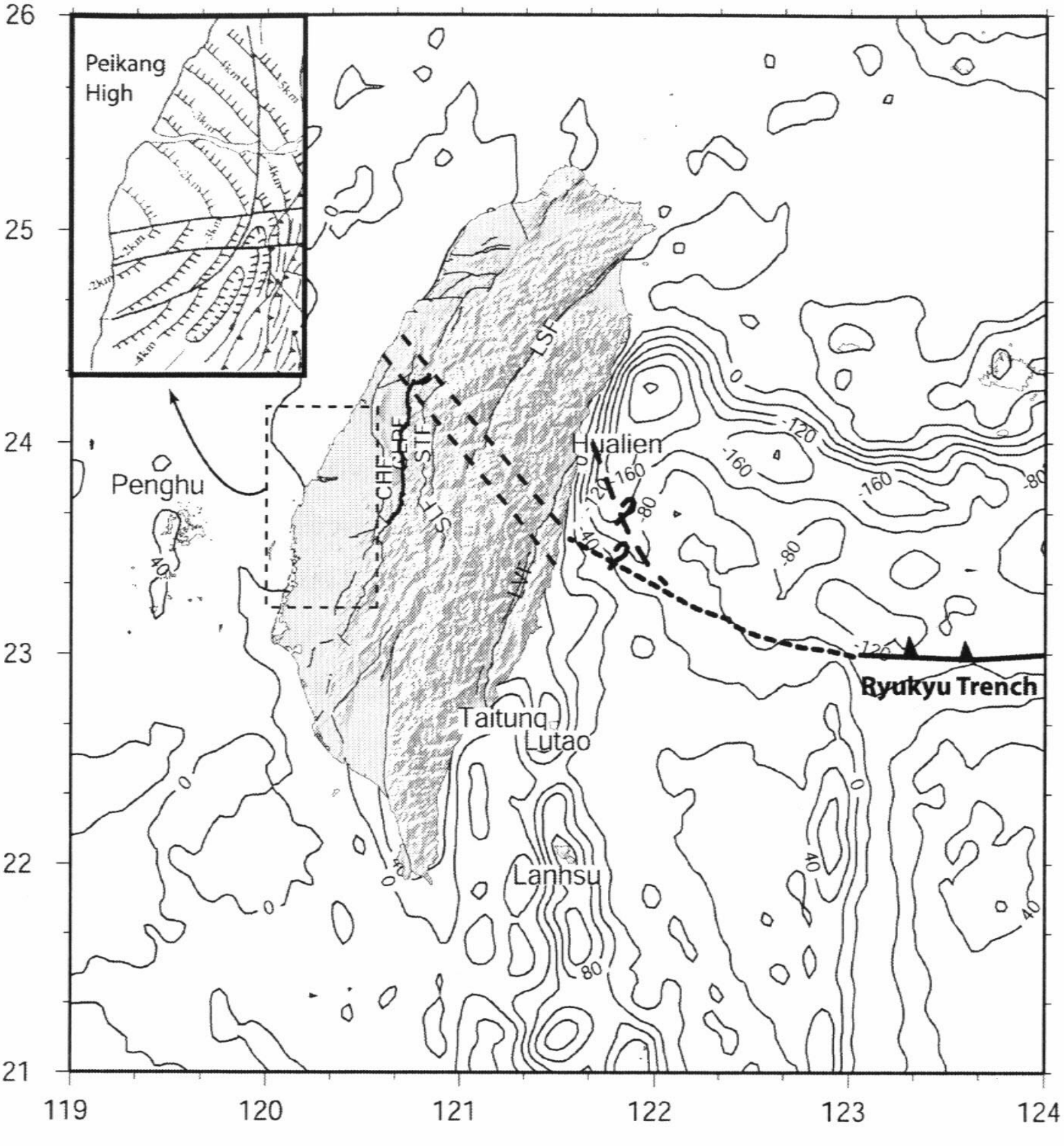

Figure 6.3: Active faults in the Taiwan island. Six fault traces are specified: CHF=ChungHua fault, CLPF=Chelungpu fault, STF=ShungTung fault, SLF=ShiLi fault, LSF=LiShan Fault, LVF=Longitudinal Valley fault. The two inland dashed lines marked the position of Central Taiwan transfer zone. The contours show the free-air gravity anomaly (Sandwith and Smith, 1994). The position of Ryukyu trench is the same as that in Figure 6.1. The dashed box isolated the anomalous region, Peikang high; the sedimentary depth contours in this region are shown in the up-left inset.

CTTZ are distributed throughout the entire crust, whereas these in the north only appear in the top 15-km (Fig. 6.4 and 6.5). The high seismicity rate in the south side suggests a strong continental crustal deformation, while the absence of earthquakes in the north side is also consistent with the argument that the collisional phase is no longer active [*Teng et al.*, 2000]. However, because seismicity is also related to the rheological properties of the crustal rocks (e.g., *Wu et al.*, 1997); in view of the sharp increment in elevation across the CTTZ (Fig. 6.5d), the absence of seismicity in the northern side of the CTTZ could also be caused by the high geotherm, which is due to the strain heating of high mountains [*Barr and Dahlen*, 1989].

The collisional activity can also be inferred from the GPS observations (Fig. 6.6, *Yu et al.*, 1997). Currently, the relative motion between the Penghu and northern parts of the Western Foothills and Hsueshan Range are negligible (Fig. 6.6). In contrast, the motion rates inside and south of the CTTZ are significant (> 1 cm/yr.). In fact, considering the huge co-seismic slip of the 1999 Chi-Chi earthquake, the motion rate in the south side will become as large as 4. cm/yr. [*Dominguez et al.*, 2002]. Such large difference actually implies that this transfer zone is a new feature in a geological time scale.

Moreover, the CTTZ appears to affect other geophysical observations. *Chen and Chen* [2000] reported a high-conductivity anomaly beneath this transfer zone. In the recent published Bouguer gravity map [*Yen et al.*, 1998], central Taiwan is associated with a large negative gravity anomaly, whereas the anomaly becomes significantly smaller in northern Taiwan. This feature is contradicted with the higher mountains in the north, and implies an active tectonic cause. The transition occurs around the CTTZ. In contrast with the east CTTZ discussed later, the small offsets associating with the west CTTZ or Sanyi-Puli seismic zone were identified at the surface. *Deffontaines et al.* [1994] found the fault trace of a Sanyi transfer fault starting at the west coastal line and extending N140°E, according to a multi-source geomorphic study. This trace is close to the northern boundary of the CTTZ (Fig. 6.3). *Hsu et al.* [1996] identified another surface trace inside the CTTZ and named it the Puli fault, which is roughly along the southern boundary of the CTTZ.

The previous focal mechanisms indicated a general left-lateral motion along this transfer zone [*Yeh et al.*, 1991]. This argument seems to be opposite of the aforementioned GPS observations, which suggests a right lateral motion. However, after the Chi-Chi earthquake, the left-lateral argument need to be revised. Note that there is important right-lateral strike-slip component on the shallow portion of the north segment of the Chi-Chi rupture. The orientation of this fault segment is N80°E. If a small part of such motion leaks before the Chi-Chi earthquake, it is also similar to a left-lateral earthquake with fault plane orienting N170°E, which is roughly following the N140°E orientation. For this reason, we consider the CTTZ as a transfer zone rather than a shear zone, even though the N140°E will be continuously used as orientation of the CTTZ for convenience.

The Sanyi-Puli seismic zone becomes broad west of the Chelungpu fault. *Deffontaines et al.* [1997] also indicated that the surface deformation associating the Sanyi transfer fault clearly decreases toward the west. Both of them suggest that the CTTZ seems to gradually die out toward the west coast.

6.3.2 East CTTZ

The east CTTZ separates the Backbone Range, the eastern Central Range and Coastal Range (Fig. 6.1 and 6.3). This segment has not been addressed in the previous literature.

It has been long recognized that the earthquakes are extremely rare in the Central Range (including backbone Range and the east Central Range) south of the CTTZ in contrast with the high seismicity in its east and west sides (Fig. 6.4). Wu et al. (1997) suggested that the significant high geotherm in this area has suppressed the seismicity. However, the cause of high geotherm is not entirely clear. The suggested candidates include strain heating of the mountain [*Barr and Dahlen*, 1989], the fast exhumation of the lower crust materials [*Wu et al.*, 1997], and additional heat flow from oceanic PSP [*Ma et al.*, 1996].

A cluster of shallow earthquakes appears in the Central range just across the

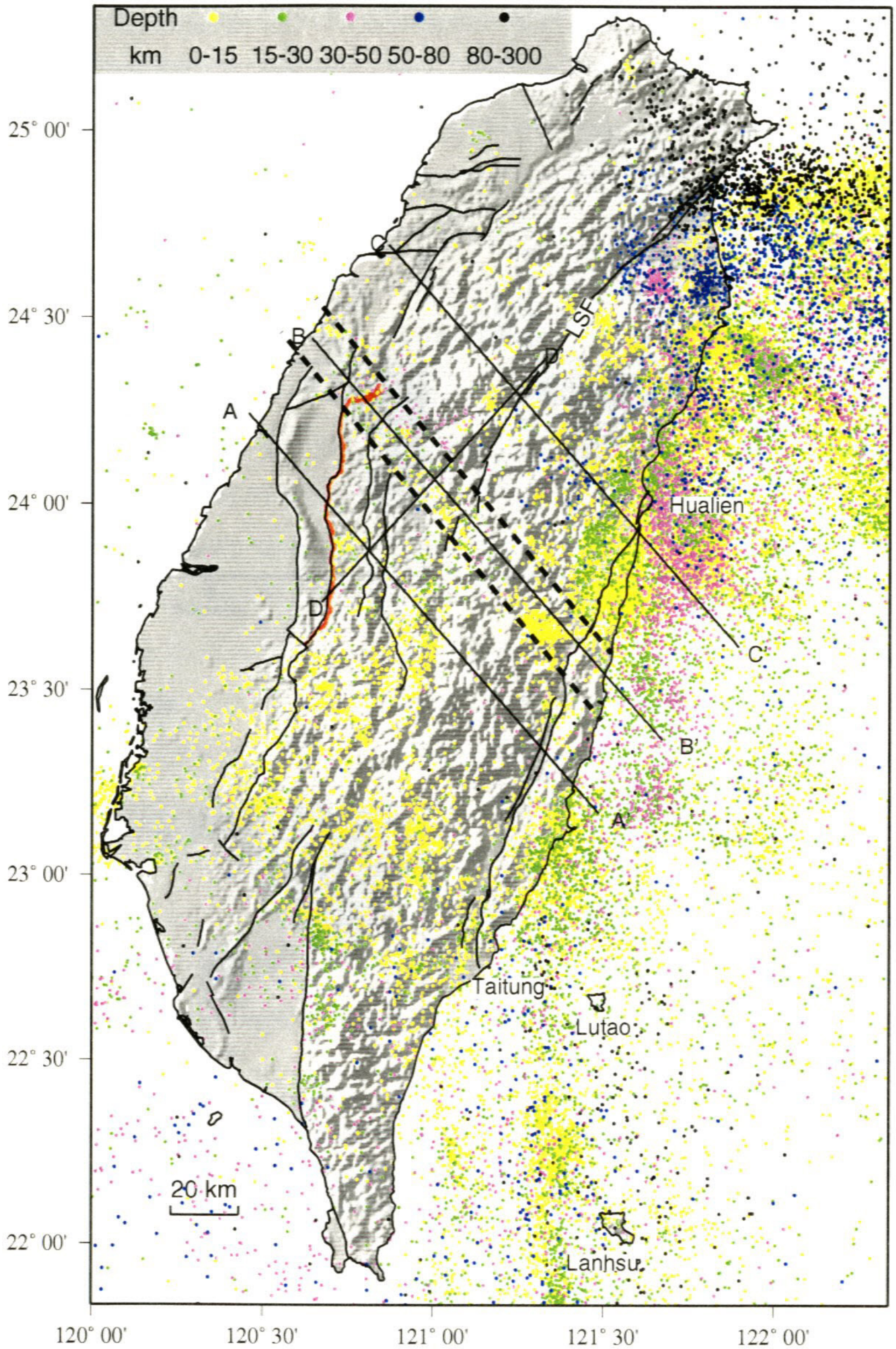

Figure 6.4: The seismicity of Taiwan and adjacent range during 1990-1998 (ML> 3, CWBSN). The depths of earthquakes are indicated in color. Lines AA', BB', CC' and DD' are the locations of seismicity crosssection shown in Figure 6.5.

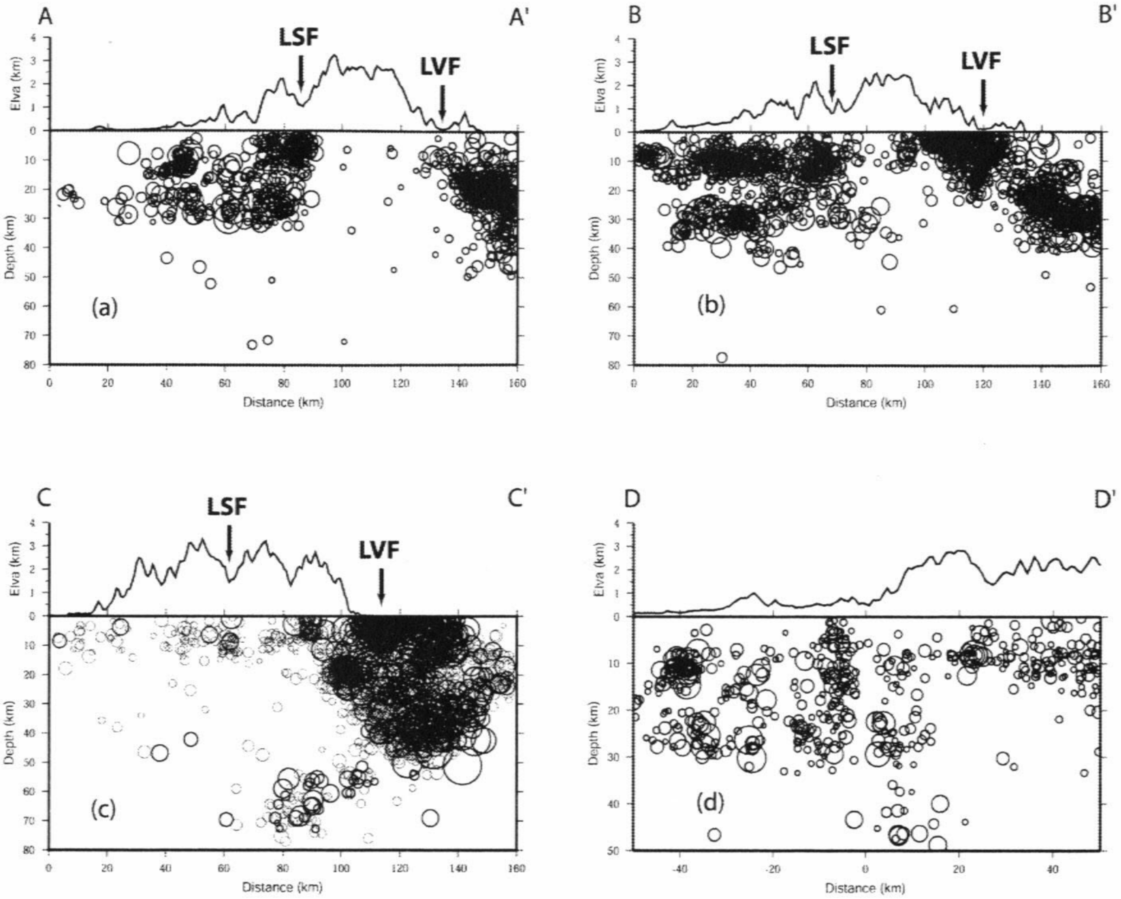

Figure 6.5: Seismicity crosssections along the lines shown in Figure 6.4. The locations of two major faults are indicated with LVF = Longitudinal Valley fault and LSF = Lishan fault. The earthquakes within 7.5 km of lines are projected on the lines. The elevations of topography are plotted for reference.

southern boundary of the CTTZ (< 15 km, yellow dots in Fig. 6.4). The focal mechanisms of two large Chi-Chi aftershocks indicated an extension stress field around this piece of the CTTZ [*Kao and Chen*, 2000]. Further across the northern boundary, the seismicity extends throughout the entire crust again (green and yellow dots in Fig. 6.4). Most of the deeper earthquakes present a compressional focal mechanisms [*Kao and Chen*, 2000]. It is noteworthy that the west boundary of the deep seismicity (>15 km, green dots in Fig. 6.4) is over 20 km inland, whereas the earthquakes with similar depths in the south of the CTTZ concentrates in the east of coastal line. Hence, the CTTZ is a sharp transition zone of the crustal seismicity. Actually, the seismicity in the north is not restricted to the crust; see that the crosssection CC' captures a linear seismic zone extending to about 70 km depth and over 40 km inland. It is suggested that the PSP probably under-thrusts beneath the west central range at about this location [*Wu et al.*, 1997].

Even though the plate convergence of the PSP and the EP is 8.1 cm/yr., oriented N306°E [*Yu et al.*, 1997], the GPS vectors along the east coastal line of central Taiwan are slightly different. They have smaller motion rates and more northward orientations in (N315°-322°E). Hence, first, some of the plate convection rate is sutured in the back of the Luzon arc. Second, the vector orientations are, in fact, parallel to the strikes of both the CTTZ and the STTZ. In other words, the Luzon arc attached to the Central Range intends to move along the CTTZ. However, a sharp transition occurred at latitude 23.6°N, the north boundary of the CTTZ. [*Yu et al.*, 1997] detected extraordinarily high shortening rates of 1.6-3.6 cm/yr. on baselines at 23.6°N; they suggested that a NE-SW trending oblique thrust cut through the Coastal Range. After this transition, the Longitudinal Valley fault (LVF), which have about 3 cm/yr shortening rates in the central Taiwan, loses the thrust component and becomes a left-lateral strike-slip fault further north [*Yu and Kuo*, 2001]. This transition apparently extends further inland. The GPS velocity vectors west of LVF are also clearly separated by the northern boundary of the CTTZ. The stations in the south side move in a more eastward direction in contrast with roughly northward motion observed in the north side stations. Such observation is consistent with the longitudinal

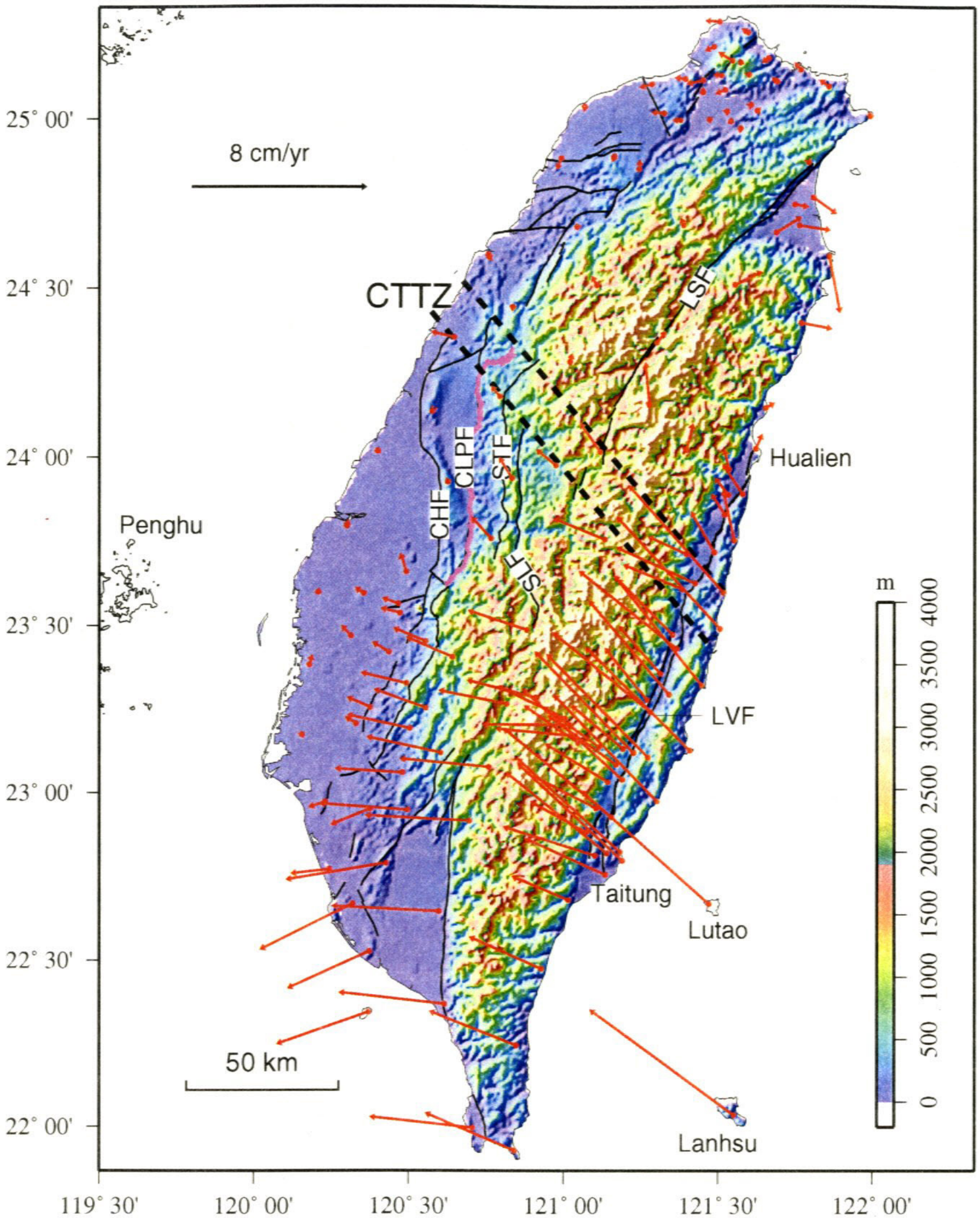

Figure 6.6: GPS velocities on the base of Taiwan topography. The reference station is at Paisai of the Penghu. The surface slip of the 1999 Chi-Chi earthquake is indicated in pink line.

extension inferred from the focal mechanisims addressed early. Finally, the crustal shortening in the eastwest direction ceases at just 10 km north of the CTTZ.

Hence, a transition along the LVF is inferred by the surface motion rate distribution. This transition is probably one of the causes of the narrow transfer zone. However, we do not know its vertical extension. A deeper extension, in fact, is very important to create a long and narrow transition zone similar to the CTTZ. Otherwise, the transfer zone would become broad gradually as we move further inland. Such information can not be directly observed but the behavior of the PSP in front of the Coast Range yields a plausible insight.

The PSP subducts beneath the EP along the Ryukyu trench. Even though a clear Wadati-Benioff zone beneath northeast Taiwan indicates that the subduction of PSP already migrated westward to 121.5°E [*Wang et al.*, 2000], the Ryukyu trench can not be easily identified west of 123°E after it meets the Gagua Ridge (Fig. 6.1). While most previous tectonic maps simply extended the Ryukyu trench to Hualien (Long dashed line inside ocean, Fig. 6.1 and 3), the subduction of the PSP probably starts south of Hualien [*Wu et al.*, 1997]. Both bathymetric and free air anomaly maps emphasize a more natural connection between the Ryukyu trench with the coastal line at 23.6°E (short dashed line, Fig. 6.1 and 6.3) rather than Hualien (24°N). After mapping the subduction zone with the earthquakes from 1990-1998, *Wang et al.* [2000] concluded that the western lithospheric boundary of the PSP is along the meridian line of 121.5°E; and the lithospheric boundary of the PSP is beneath the Taiwan north of 23.5°N. Hence, a transition from the collisional phase to the subduction phase of the PSP has probably occurred within the extension of the CTTZ. Such coincidence suggests that we should think about the interaction of the PSP and the EP.

6.4 Discussions and conclusion

One of the unique features of the Taiwan orogeny is that the collision is propagated southeastward. Then, we can consider the deformation pattern in the northern Taiwan is the future stage of the collisions occurred in the central and southern Taiwan.

The clear Benioff zone beneath the northeast Taiwan indicated that the interaction between the two plates still exists but occurs in the mantle depth. Then a question rises naturally, where is the subducted EP, or even South China Sea Plate (SCSP) in front of the EP?

Because of the absence of the subducted slab of the SCSP in the previous tomography models and less intermediate earthquakes (50-80 km) between 23°N to 23.6°N, the size of the original SCSP was widely debated until the recent study of [*Lallemand et al.*, 2001]. They found evidence of the SCSP slab beneath the PSP at the depth deeper than 100 km in a new irregular-cell tomography model [*Bijwaard et al.*, 1998]. Two important observations related to this study are repeated here. First, the SCSP had extended to at least 126°E before the subduction of the SCSP beneath the PSP starting at about 8 Ma ago. Second, the SCSP slab detached from the EP at some place northeast of the Taiwan as that hypothesized by *Teng et al.* [2000]. Unfortunately, the shape of the EP continental margin can not be well defined from the tomography model. Here, we assumed that the ocean-continent boundary of the EP and the SCSP (OCB) is along the extension of its current position (thick long-dashed dashed line, Fig. 6.1.), and a similar assumption also used in the work of *Lallemand et al.* [2001]. Then this boundary is oriented roughly N60°E. Such OCB location implies that the continental margin starts to subduct beneath the Luzon arc at some place of central Taiwan.

However, because of the positive buoyancy, the subduction of the continental plate can not go too deep. Sooner or later, the sinking oceanic plate will create enough negative buoyancy to break the slab. The rift is most likely along the preexisting weak zone, i.e., the ocean-continent boundary. However, the break of continental plate is also possible [*Davies and Blanckenburg*, 1995]. *Teng et al.* [2000] hypothesized that the slab breakoff already happens at some place south of the Hualien. *Lallemand et al.* [2001] suggested the rift started at 25°N about 3Ma ago and propagated westward during the Quaternary. They argued that the rift was already propagated to 23°N, thus explains the absence of intermediate earthquakes. However, if the ocean-continent boundary of EP and SCSP is along the line we draw, it will be the continental plate rather than the oceanic plate appeared at that depth region. Then earthquakes will be suppressed due to the geotherm effect (e.g., *Wu et al.*, 1997). So we think that the entire breakoff of slab propagates to some place around 23.5°N because of the existence of the CTTZ.

As soon as the SCSP slab detaches from the EP plate, a mantle window will form to allow the north-dipping PSP to move in laterally [*Teng et al.*, 2000]. Two effects occurred immediately. First, the crustal shorten in plate motion direction would significantly reduce. Then a deep extension of the transition inferred from the GPS observations will be suggested, which is a necessary condition to form a long and narrow transfer zone as mentioned early. Second, after the slab breaks off, the continental slab in the north will bend upward because of the positive buoyancy, whereas the south side is still pulled downward by the heavy SCSP slab [*Teng et al.*, 2000]. Then a tear shear will be accumulated at the boundary from mantle depth to the surface. In fact, several deep tear events within the CTTZ were included in the Chi-Chi aftershock sequence [*Kao and Chen*, 2000]. It is probably the cause of deeper extension of the CTTZ. However, the coincidence of the tear shear zone and the CTTZ should be illustrated by a future effect with three-dimensional numerical simulation.

The transfer zone is not a permanent feature by this mechanism. As the rift on the slab propagates southward, the transfer zone will also migrate southwest. Because the southward migration of the Ryukyu arc is 4-5 cm/yr. [*Lallemand et al.*, 2001], the CTTZ will reach the current position of the STTZ in about 1 My. Such migration behavior is not only consistent with the absence of surface offset across the transfer zone, but also in agreement with the observations of the 1999 Chi-Chi earthquake. Before the Chi-Chi earthquake occurred, the CLPF had already received attention. It was treated as an active fault and well mapped. However, the mapped fault trace does not turn at the current position; instead, it follows a valley at about 20 km north [*Bonilla*, 1975]. Then the occurrence of Chi-Chi earthquake implies that the rupture front of the CLPF migrated southward. In other words, the stable northern Taiwan impedes the northward propagation of co-seismic motion. Because the plate motion direction in the Central Taiwan is oblique to the striking of the major part of the CLPF, we would expect the uplift is not uniform along the CLPF fault plane; instead, the largest rise should be in the north part. This is consistent by the 6 meter waterfall created at the north tip [*Ma et al.*, 2000] and could be better illustrated by the co-seismic surface motions predicted by our slip model (Fig. 6.7). Note that 3-5 meters uplift occurred at the north end. This high uplift region coincides with a range oriented east-west (Fig 6.6). The red dashed line following the valley in the south of the range. *Dominguez et al.* [2002] suggested the seismic cycle of the Chelungpu fault is around 200 years, then we will expect about 1 km elevation increment within a short period of 0.1 Ma, even taking a 0.55 cm/yr. average erosion rate [*Davis et al.*, 1983] into account. Because the ranges with such shape and orientation are, in fact, very popular in the northern Taiwan but are absent in the southern Taiwan, we then hypothesize that most mountains of the west foothills in the northern Taiwan were built up this way.

In summary, the slip history of the 1999 Chi-Chi earthquake suggests the existence of two narrow transfer zones, which divide Taiwan into three regions with different tectonic behavior. The CTTZ has little relation with the surface geological evidence but is consistent with many geological observations. Its characteristics can be well explained by the slab breakoff model proposed recently (*Teng et al.*, 2000; *Lallemand et al.*, 2001). However, the research to the full understanding of the Taiwan orogeny is still undergoing. Particularly, the cause of the sharp transition along the STTZ is not elucidated.

This result, in fact, emphasizes the lessons that we obtained in the studies of the 1992 Landers, California, earthquake [*Nur et al.*, 1993] and the 1999 Hector Mine earthquake [*Ji et al.*, 2002b]. The large scale variations in the strike of active fault planes include very important information related to the evolution of the local stress field and should be further studied. In addition, divergence and convergence slip patterns presented in the Chi-Chi slip distribution are important features that should be considered in the study of other earthquakes.

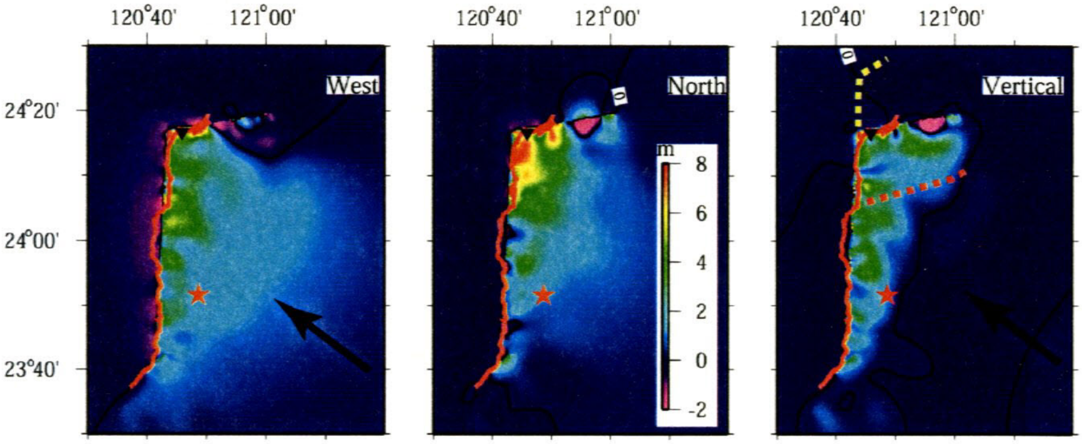

Figure 6.7: The surface slip predicted by the slip model inverted from static data [*Ji et al.*, 2001]. The red line shows the position of surface break, star indicates the epicenter and arrow shows the PSP motion direction relative to EP. Only the transition from position to negative is showed by the contour. Note that the Chelungpu fault was believed to extend further north as yellow dashed line [*Bonilla*, 1975]. An east-west oriented valley follows the red dashed line.

Bibliography

Aagaard, B., T. Heaton, and J. Hall, Dynamic earthquake ruptures in the presence of lithostatic normal stresses: Implications for friction models and heat production, *Bull. Seism. Soc. Am.*, *in press*, 2002.

Abercrombie, R., and J. Mori, Local observations of the onset of a large earthquake: 28 June 1992 Landers, California, *Bull. Seism. Soc. Am.*, *84*, 725–734, 1994.

Aki, K., and P. G. Richards, *Quantitative Seismology: Theory and methods*, W. H. Freeman and Co., New York, 1980.

Angelier, J., Geodynamics of the Eurasia-Philippine Sea Plate boundary: Preface, *Tectonophysics*, *125*, 1–3, 1986.

Angelier, J., F. Bergeat, and H.-T. Chu, Plate collision and paleostress trajectories in a fold-and-thrust belt: the foothills of Taiwan, *Tectonophysics*, *125*, 161–178, 1986.

Barr, T. D., and F. A. Dahlen, Brittle frictional mountain building, 2. thermal structure and heat-budget, *J. Geophys. Res.*, *94*, 3923–3947, 1989.

Beroza, G. C., Near-source modeling of the Loma Prieta earthquake: evidence for heterogeneous slip and implications for earthquake hazard, *Bull. Seism. Soc Am.*, *81*, 1603–1621, 1991.

Beroza, G. C., and P. Spudich, Linearized inversion for fault rupture behavior: Application to the 1984 Morgen Hill, California, Earthquake, *J. Geophys. Res.*, *93*, 1988.

Bijwaard, H., W. Sparkman, and E. R. Engdahl, Closing the gap between regional and global travel time tomography, *J. Geophys. Res.*, *103*, 30,055–30,078, 1998.

Bonilla, M. G., A review of recently active faults in Taiwan, *Open-File report 75-41, U. S. geological Survey*, 1975.

Brune, J., Particle motions in a physical model of shallow angle thrust faulting, *Proceedings of the Indian Academy of Sciences-Earth and Planetary Sciences*, *105*, L197–L206, 1996.

Chemenda, A. I., R.-K. Yang, C.-H. Hsieh, and A. L. Groholsky, Evolutionary model for the Taiwan collision based on physical modeling, *Tectonophysics*, *274*, 253–274, 1997.

Chen, C.-C., and C.-S. Chen, Preliminary report on the Sanyi-Puli seismic zone conductivity anomaly and its correlation with velocity structure and seismicity in the northwestern Taiwan, *Earth Planets and Space*, *52*, 377–381, 2000.

Chen, K.-C., B.-S. Huang, J.-H. Wang, W.-G. Huang, T.-M. Chang, R.-D. Hwang, H.-C. Chiu, and C.-C. P. Tsai, An observation of rupture pulses of 20 September 1999 Chi-Chi, Taiwan, earthquake from near-field seismograms, *Bull. Seism. Soc. Am.*, *91*, 1247–1254, 2001.

Chi, W.-C., D. Dreger, and A. Kaverina, Finite-Source modeling of the 1999 Taiwan (Chi-Chi) earthquake derived form a dense strong-motion network, *Bull. Seism. Soc. Am.*, *Submitted*, 2001.

Cohee, B. P., and G. C. Beroza, Slip distribution of the 1992 Landers earthquake and its implications for earthquake source mechanics, *Bull. Seism. Soc. Am.*, *84*, 692–712, 1994.

Cotton, F., and M. Campillo, Frequency domain inversion of strong motions: Application to the 1992 Landers earthquake, *J. Geophys. Res.*, *100*, 1995.

Davies, J. H., and F. V. Blanckenburg, Slab breakoff: A model of lithosphere detachment and its test in the magmatism and deformation of collisional orogens, *Earth and Planetary Science Letters*, *129*, 1995.

Davis, D., J. Suppe, and F. A. Dahlen, Mechanics of fold-and-thrust belts and accretionary wedges, *J. Geophys. Res.*, *88*, 1153–1172, 1983.

Deffontaines, B., J.-C. Lee, J. Carvalho, and J.-P. Rudant, New geomorphic data on the active Taiwan orogen: A multisource approach, *J. Geophys. Res.*, *99*, 20,243–20,266, 1994.

Deffontaines, B., et al., Qauaternary transfer faulting in Taiwan foothills: evidence from a multisource approach, *Tectonophysics*, *274*, 61–82, 1997.

Dominguez, S., J.-P. Avouac, and R. Michel, Horizontal co-seismic deformation of the 1999 Chi-Chi earthquake measured from SPOT satellite images: implications for the siesmic cycle along the western foothills of Central Taiwan, *J. Geophys. Res.*, *submitted*, 2002.

Dreger, D. S., Investigation of the rupture process of the 28 June 1992 Landers earthquake utilizing terrascope, *Bull. Seism. Soc. Am.*, *84*, 713–724, 1994.

Dreger, D. S., and D. V. Helmberger, Determination of source parameters regional distances with three-component sparse network data, *J. Geophys. Res.*, *98*, 8107–8125, 1993.

Dreger, D. S., and A. Kaverina, Seismic remote sensing for the earthquake source process and near-source strong shaking: A case study of the October 16, 1999 Hector Mine earthquake, *Geophys. Res. Lett.*, *27*, 1941–1944, 2000.

Ellsworth, W. L., and G. C. Beroza, Seismic evidence for an earthquake nucleation phase, *Science*, *268*, 851–855, 1995.

Fialko, Y., M. Simons, and D. Agnew, The complete (3-D) surface displacement field in the epicentral area of the 1999 M_w 7.1 Hector Mine earthquake, California, from space geodetic observations, *Geophys. Res. Lett.*, *28*, 3063–3066, 2001.

Graves, R. W., and D. J. Wald, Resolution analysis of finite fault source inversion using 1D and 3D Green's functions, Part I: Strong motion, *J. Geophys. Res.*, *106*, 8745–8766, 2001.

Guatteri, M., and P. Spudich, What can strong-motion data tell us about slip-weakening fault-friction law, *Bull. Seism. Soc. Am.*, *90*, 98–116, 2000.

Hartzell, S. H., and T. H. Heaton, Inversion of strong ground motion and teleseismic waveform data for the fault rupture history of the 1979 Imperial Valley, California, earthquake, *Bull. Seism. Soc Am.*, *73*, 1553–1583, 1983.

Hartzell, S. H., P. Liu, and C. Mendoza, The 1994 Northridge, California, earthquake: Investigation of rupture velocity, rise time, and high-frequency radiation, *J. Geophys. Res.*, *101*, 20,091–20,108, 1996.

Hauksson, E., Crustal structure and seismicity distribution adjacent to the Pacific and North America plate boundary in Southern California, *J. Geophys. Res.*, *105*, 13,875–13,903, 2000.

Hauksson, E., L. M. Jones, and K. Hutton, The 1999 M_w 7.1 california earthquake sequence: Complex conjugate strike slip faulting, *Bull. Seism. Soc. Am.*, *92*, in press, 2002.

Heaton, T. H., Evidence for and implications of self-healing pulses of slip in earthquake rupture, *Phys. Earth Planet. Inter.*, *64*, 1–20, 1990.

Hsu, C.-H., C. I. Lee, and J. F. Lee, NW-SE trending seismic zone in the Miaoli-Taichung-Nantou area, Central Taiwan, and its implication in tectonics, *Proceedings of the Sixth Symposium on Taiwan Quarternary*, pp. 224–228 (In Chinese), 1996.

Hu, J.-C., J. Angelier, J. Lee, H.-T. Chu, and D. Byrne, Kinematics of convergence, deformation and stress distribution in the Taiwan collision area: 2-D finite-element numerical modelling, *Tectonophysics*, *255*, 243–268, 1996.

Huang, B.-S., Two-dimensional reconstruction of the surface ground motions of an earthquake: The September 21, 1999, Chi-Chi, Taiwan earthquake, *Geophys. Res. Lett.*, *27*, 3025–3028, 2001.

Hudnut, K. W., et al., Co-seismic displacements of the 1994 Northridge, California, earthquake, *Geol. Soc. Am. Bull.*, *86*, S19–S36, 1996.

Ji, C., D. V. Helmberger, A. Song, K.-F. Ma, and D. J. Wald, Slip distribution and tectonic implication of the 1999 Chi-Chi, Taiwan, earthquake, *Geophys. Res. Lett.*, *28*, 4379–4382, 2001.

Ji, C., D. J. Wald, and D. V. Helmberger, Source description of the 1999 Hector Mine, California earthquake; Part I: Wavelet domain inversion theory and resolution analysis, *Bull. Seism. Soc. Am.*, *Submitted*, 2002a.

Ji, C., D. J. Wald, and D. V. Helmberger, Source description of the 1999 Hector Mine, California earthquake; Part II: Complexity of slip history, *Bull. Seism. Soc. Am.*, *Submitted*, 2002b.

Johnson, K. M., Y.-Y. Hsu, P. Segall, and S.-B. Yu, Fault geometry and slip distribution of the 1999 Chi-Chi, Taiwan earthquake imaged from inversion of GPS data, *Geophys. Res. Lett.*, *28*, 2285–2288, 2001.

Jones, L. E., and D. V. Helmberger, Earthquake source parameters and fault kinematics in the Eastern California shear zone, *Bull. Seism. Soc. Am.*, *88*, 1337–1352, 1998.

Kanamori, H., and T. H. Heaton, Microscopic and macroscopic physics of earthquake, *GeoComplexity and the Physics of Earthquake*, 2000.

Kanamori, H., H. K. Thio, D. Dreger, E. Hauksson, and T. Heaton, Initial investigation of the Landers, California, earthquake of 28 June 1992 using TERRAscope, *Geophys. Res. Lett.*, *19*, 2267–2270, 1992.

Kao, H., and W.-P. Chen, The Chi-Chi earthquake sequence: Active, out-of-sequence thrust faulting in Taiwan, *Science*, *288*, 2346–2349, 2000.

Kennett, B. L., and E. R. Engdahl, Traveltimes for global earthquake location and phase identification, *Geophys. J. Inter.I*, *105*, 429–465, 1991.

Lallemand, S., Y. Font, H. Bijwaard, and H. Kao, New insights on 3-D plates interaction near Taiwan from tomography and tectonic implications, *Tectonophysics*, *335*, 229–253, 2001.

Langston, C. A., and D. V. Helmberger, A procedure for modeling shallow dislocation sources, *Geophys. J.*, *42*, 117–130, 1975.

Lee, J.-C., H.-T. Chu, J. Angelier, C. Y.-C., H. J.-C., and C.-Y. Lu, Structural characteristic of northern surface ruptures of the 1999 M_w=7.6 Chi-Chi, Taiwan earthquake, *EOS*, p. F875, 2000a.

Lee, T.-Q., C. Kissel, E. Barrier, C. Laj, and W.-R. Chi, Paleomagnetic evidence for a diachronic clockwise rotation of the coastal range, eastern Taiwan, *Earth Planet. Sci. Lett.*, *98*, 23–32, 1991.

Lee, W., T. C. Kuo, and K. C. Chen, CWB free-field strong motion data from the 921 Chi-Chi earthquake: Volume 1. digital acceleration files on CD-ROM, *Seismology Center, Central Weather Bureau, Taipei, Taiwan*, *Prepublication version: December 6*, 1999.

Lee, Y., Y. Sugiyama, T. Azuma, and Y. Kariya, Displacement and segmentation of the surface fault, 1999 Chi-Chi, Taiwan, earthquake, *EOS*, p. F882, 2000b.

Ma, K.-F., J.-H. Wang, and D. Zhao, Three-dimensional seismic velocity structure of the crust and uppermost mantle beneath Taiwan, *Journal of Physical Earth*, *44*, 85–105, 1996.

Ma, K.-F., C.-T. Lee, Y.-B. Tsai, T.-C. Shin, and J. Mori, The Chi-Chi, Taiwan earthquake: Large surface displacements on an inland thrust fault, *EOS*, pp. 605–611, 1999.

Ma, K.-F., S.-J. L. Teh-Ru Alex Song, and H.-I. Wu, Spatial slip distribution of the September 20, 1999, Chi-Chi, Taiwan, earthquake (M_w 7.6)–Inverted from the teleseismic data, *Geophys. Res. Letters*, *27*, 3417–3420, 2000.

Ma, K.-F., J. Mori, S. Lee, and S.-B. Yu, Rupture process of the 1999 Chi-Chi, Taiwan, earthquake from strong motion, teleseismic and GPS data, *Bull. Seism. Soc. Am.*, *91*, 1069–1087, 2001.

Madariaga, R., High-frequency radiation from dynamic earthquake fault models, *Ann. Geophys.*, *1*, 1983.

Mallat, S., *A wavelet tour of signal processing*, Academic Press, San Diego, USA, 1998.

Mendoza, C., and S. Hartzell, Inversion for slip distribution using teleseismic P waveforms: North Palm Springs, Borah Peak, and Michoacan earthquakes, *Bull. Seism. Soc. Am.*, *78*, 1092–1111, 1988.

Mori, J., H. Kanamori, J. Davis, E. Hauksson, R. Clayton, T. Heaton, L. Jones, and A. Shakal, Major improvements in progress for southern California earthquake monitoring, *Trans. Am. Geophys. U.*, *79*, 217–221, 1999.

Ni, S., J. N. Brune, G. Choy, J. G. Anderson, and Y. Zeng, Local and teleseismic estimates of radiated energy and apparent stress from the Ch-Chi, Taiwan earthquake: evidence for inertial detachment of the hanging wall from the footwall in thrust faulting, *AGU 1999 Fall Meeting program*, 1999.

Nur, A., H. Ron, and G. C. Beroza, The nature of the Landers-Mojave earthquake line, *Science*, *261*, 1993.

Oglesby, D., and S. Day, The effect of fault geometry on the 1999 Chi-Chi (Taiwan) earthquake, *Geophys. Res. Lett.*, *28*, 1831–1834, 2001.

Oglesby, D., R. Archuleta, and S. Nielsen, Earthquakes on dipping faults: The effects of broken symmetry, *Science*, *280*, 1055–1059, 1998.

Olsen, K. B., R. Madariaga, and R. J. Archuleta, Three-dimensional dynamic simulation of the 1992 landers earthquake, *Science*, *278*, 834–838, 1997.

Olson, A. H., and J. H. Anderson, Implications if frequency-domain inversion of earthquake ground motions for resolving the space-time dependence of slip on an extended fault, *Geophysical Journal*, *94*, 443–455, 1988.

Olson, A. H., and R. Apsel, Finite fault and inversion theory with applications to the 1979 Imperial Valley earthquake, *Bull. Seism. Soc Am.*, *72*, 1982.

Rau, R. J., and F. Wu, Tomographic imaging of lithospheric structure under Taiwan, *Earth Planet. Sci. Lett.*, *133*, 517–532, 1995.

Rosen, P. A., S. Hensley, I. R. Joughin, F. K. Li, S. N. Madsen, E. Rodriguez, and R. M. Goldstein, Synthetic aperture radar interferometry - Invited paper, *PROCEEDINGS OF THE IEEE*, *88*, 2000.

Rothman, D. H., Automatic estimation of large residual statics corrections, *Geophysics*, *51*, 337–346, 1986.

Sandwell, D. T., and W. H. F. Smith, new global marine gravity map/grid based on stacked ERS1 Geosat and Topexaltimetry, *EOS*, *75*, 321, 1994.

Scholz, C. H., *The mechanics of earthquakes and faulting*, Cambridge University Press, 1990.

Scientists from the U.S. Geological Survey, S. C. E. C., C. D. of Mines, and Geology, Preliminary report on the 10/16/1999 M7.1 Hector Mine, California earthquake, *Seismo. Res. Lett.*, 2000.

Segall, P., and D. D. Pollard, Mechanics of discontinuous faults, *J. Geophys. Res.*, *88*, 555–568, 1983.

Sen, M. K., and P. L. Stoffa, Nonlinear one-dimensional seismic waveform inversion using Simulated Annealing, *Geophysics*, *56*, 1624–1638, 1991.

Sen, M. K., and P. L. Stoffa, *Global optimization methods in geophysical inversion*, Elsevier Science B. V., Amsterdam, The Netherlands, 1995.

Seno, T., S. Stein, and A. E. Gripp, A model for the motion of the Philippine Sea plate consistent with NUVEL-1 and geological data, *J. Geophys. Res.*, *109*, 17,941–17,948, 1993.

Sieh, K. L., et al., Near-field investigations of the Landers earthquake sequence, April to July, *Science*, *260*, 171–176, 1993.

Suppe, J., Mechanics of Mountain building and metamorphism in Taiwan, *Mem. Geol. Soc. China*, *4*, 67–89, 1981.

Teng, L. S., Geotectonic evolution of late Cenozoic arc-continent collision in Taiwan, *Tectonophysics*, *183*, 67–76, 1990.

Teng, L.-S., C.-T. Lee, Y.-B. Tsai, and L.-Y. Hsiao, Slab breakoff as a mechanism for flipping of subduction polarity in Taiwan, *Geology*, *28*, 155–158, 2000.

Wald, D. J., D. V. Helmberger, and S. H. Hartzell, Rupture process of the 1987 Superstition Hills earthquake from the inversion of strong-motion data, *Bull. Seism. Soc. Am.*, *80*, 1079–1098, 1990.

Wald, D. J., D. V. Helmberger, and T. H. Heaton, Rupture model of the 1989 Loma Prieta earthquake from the inversion of strong-motion and broadband teleseismic data, *Bull. Seism. Soc. Am.*, *81*, 1540–1572, 1991.

Wald, D. J., and T. H. Heaton, Spatial and temporal distribution of slip for the 1992 Landers, California, earthquake, *Bull. Seism. Soc. Am.*, *84*, 668–691, 1994.

Wald, D. J., T. H. Heaton, and K. W. Hudnut, A dislocation model of the 1994 Northridge, California earthquake determined from strong-motion, GPS, and leveling-line data, *Bull. Seism. Soc. Am.*, *86*, S49–S70, 1996.

Wald, D. J., and R. W. Graves, Resolution analysis of finite fault source inversion using 1D and 3D Green's functions, Part II: Combining seismic and geodetic data, *J. Geophys. Res.*, *106*, 8767–8788, 2001.

Wang, C.-S., T.-H. Huang, I.-C. Yen, S.-L. Wang, and W.-B. Cheng, Tectonic environment of the 1999 Chi-Chi earthquake in Central Taiwan and its aftershock sequence, *TAO*, *11*, 661–678, 2000.

Wu, C.-J., M. Takeo, and S. Ide, Source process of the Chi-Chi earthquake: A joint inversion of strong motion data and Global positioning system data with a multifault model, *Bull. Seism. Soc. Am.*, *91*, 1128–1143, 2001.

Wu, F., R.-J. Rau, and D. Lalzberg, Taiwan orogeny: thin-skinned or lithospheric collision?, *Tectonophysics*, *274*, 191–200, 1997.

Xie, X.-B., and Z.-X. Yao, A generalized reflection-transmission coefficient matrix method to calculate static displacement field of a dislocation source in a stratified half-space, *Chinese J. Geophysics*, *32*, 191–205, 1989.

Yamada, M., and K. Ohkitani, Orthonormal wavelet analysis of turbulence, *Fluid Dyn. Res.*, *8*, 101–115, 1991.

Yao, Z., and C. Ji, Finite fault inversion in the time domain, *Chinese J. Geophysics*, 1998.

Yeh, Y. H., E. Barrier, C. H. Lin, and J. Angelier, Stress tensor analysis in the Taiwan area from focal mechanisms of earthquakes, *Tectonophysics*, *200*, 267–280, 1991.

Yen, H.-Y., Y.-H. Yeh, and F. T. Wu, Two-dimensional crustal structures of Taiwan from gravity data, *Tectonics*, *17*, 104–111, 1998.

Yomogida, K., Detection of anomalous seismic phases by the wavelet transform, *Geophys. J. Int.*, *116*, 119–130, 1994.

Yu, S.-B., and L.-C. Kuo, Present day crustal motion along the longitudinal valley fault, east Taiwan, *Tectonophysics*, *333*, 199–217, 2001.

Yu, S.-B., H.-Y. Chen, and L.-C. Kuo, Velocity field of GPS stations in the Taiwan area, *Tectonophysics*, *274*, 41–59, 1997.

Yu, S.-B., et al., Preseismic deformation and coseismic displacements associated with the 1999 Chi-Chi, Taiwan earthquake, *Bull. Seism. Soc. Am.*, *submitted*, 2001.

Zeng, Y., and C.-H. Chen, Fault rupture process of the September 20, 1999 Chi-Chi, Taiwan earthquake, *Bull. Seism. Soc. Am.*, *Submitted*, 2001.

Zhao, L.-S., and D. V. Helmberger, Source estimation from broadband regional seismograms, *Bull. Seism. Soc. Am.*, *84*, 91–104, 1994.

Zhu, L., and D. V. Helmberger, Advancement in source estimation techniques using broadband regional seismograms, *Bull. Seism. Soc. Am.*, *86*, 1634–1641, 1996.

Zhu, L., and L. A. Rivera, Computation of dynamic and static displacement from a point source in multi-layered media, *Geophys. J. Int.*, *submitted*, 2000.